Single Trapped Atom System and Its Applications in Quantum Thermal Machines

by

Mohsen Izadyari

A Dissertation Submitted to the
Graduate School of Sciences and Engineering
in Partial Fulfillment of the Requirements for
the Degree of

Doctor of Philosophy

in

Physics

KOÇ ÜNİVERSİTESİ

November, 2022

Single Trapped Atom System and Its Applications in Quantum Thermal Machines

Koç University

Graduate School of Sciences and Engineering

This is to certify that I have examined this copy of a doctoral dissertation by

Mohsen Izadyari

and have found that it is complete and satisfactory in all respects,
and that any and all revisions required by the final
examining committee have been made.

Committee Members:

_____

Prof. Özgür E. Müstecaplıoğlu (Advisor)

_____

Assoc. Prof. Kadır Durak

_____

Assoc. Prof. Menderes Işkın

_____

Assoc. Prof. Alkan Kabakçıoğlu

_____

Assoc. Prof. Barış Çakmak

Date: _____

Dedication here (Optional)

ABSTRACT

Single Trapped Atom System and Its Applications in Quantum Thermal Machines

Mohsen Izadyari

Doctor of Philosophy in Physics

November, 2022

A quantum heat engine is a machine that converts thermal energy to work by following the quantum mechanics laws. In this thesis, I investigate single atom-field interaction and its applications in quantum thermal machines. I show the possibility of exploiting thermodynamic processes for enantiomer detection, which are chiral molecules that exist in right-handed and left-handed conformations. A quantum Otto cycle is employed, in which a chiral molecule described by a three-level system with cyclic optical transitions is considered a working medium. I demonstrate that left and right-handed molecules can be distinguished by evaluating the work distribution in the Otto cycle. Also, I show how quantum signatures can appear in a single-atom heat engine consisting of an atom confined in a tapered trap and subject to hot and cold thermal reservoirs. It is found that lowering the temperature is insufficient to make the single-atom engine of Ref. [Roßnagel et al., 2016] a genuine quantum-enhanced heat engine. I show that it is necessary to make the trap more asymmetric and confined to ensure that quantum correlations cause an enhancement in the power output. A method is presented to generate a dipole trap with a radius of the sub-diffraction limit, which makes the atom more confined. Moreover, I indicate that the single atom-field coupling strength is improved by reducing the trap's radius.

ÖZETÇE

Doktora Tez Başlığı
Mohsen Izadyari
Fizik, Doktora
30 Kasım 2022

Bu tezde, atom-ışık etkileşimini araştırıyor ve kuantum termal makinelerdeki uygulamalarını gösteriyoruz. Sağ elli ve sol elli konformasyonlarda bulunan kiral moleküller olan enantiyomer tespiti için termodinamik süreçlerden yararlanma olasılığını gösteriyoruz. Otto döngüsündeki iş dağılımını değerlendirerek sol ve sağ elli moleküllerin ayırt edilebileceğini gösterdik. Ayrıca, konik bir tuzakta hapsedilmiş ve sıcak ve soğuk termal rezervuarlara maruz kalan bir atomdan oluşan tek atomlu bir ısı motorunda kuantum imzalarının nasıl ortaya çıkabileceğini gösteriyoruz. Sıcaklığın düşürülmesinin, Ref. [Roßnagel et al., 2016]'daki tek atom motorunu gerçek bir kuantumla güçlendirilmiş ısı makinesi yapmak için yetersiz olduğunu bulduk. Kuantum korelasyonlarının güç çıkışında bir artışa neden olmasını sağlamak için tuzağı daha asimetrik ve sınırlı hale getirmenin gerekli olduğunu gösteriyoruz. Atomu daha sınırlı hale getirmek için, kırınım altı sınırının yarıçapına sahip bir dipol tuzağı oluşturmak için bir yöntem sunuyoruz. Ayrıca, tuzağın yarıçapı azaltılarak tek atom alanı bağlantı kuvvetinin geliştirildiğini belirtiyoruz.

ACKNOWLEDGMENTS

I would like to express my gratitude and appreciation for Prof. Özgür E. Müstecaplıoğlu whose guidance, support, and encouragement have been invaluable throughout this study. I want to thank my wife, Sama, for her patience, asset, and encouragement and my family for supporting me during the compilation of this dissertation. Furthermore, I would like to thank Prof. Kadir Durak for his collaborative support during my research. Finally, I wish to thank the Quest team members and my friends, who have supported me immensely.

TABLE OF CONTENTS

List of Tables **x**

List of Figures **xi**

Abbreviations **xviii**

Chapter 1: Introduction **1**

Chapter 2: The Principles I (Atom-Field Interaction) **5**

2.1 Two-Level Atom-field Interaction 5

2.1.1 Atom interaction with a Classical Field 5

2.1.2 The Jaynes-Cummings model 8

2.1.3 Spontaneous Emission 10

2.2 Three-level System 12

2.3 Atom Trap 14

2.3.1 Paul Trap 15

2.3.2 Magneto-Optical Trap (MOT) 15

2.4 Dipole Trap 16

2.4.1 Model system 16

2.4.2 Atomic polarizability 17

2.4.3 The Gaussian Beam 19

2.4.4 Dipole Trap's Dynamics (Red Detuned) 20

2.4.5 Designing a Blue-Detuned Trap 22

2.4.6 Blue-detuned Trap Equation of the Motion 25

2.5 Strongly Focused Light Beam 25

2.5.1 Focusing with an ideal lens 27

2.5.2 A Tight Blue-Detuned Trap 29
2.5.3 Generation of a sub-diffraction blue-detuned Trap 30

Chapter 3: The Principles II (Quantum Thermodynamics) 34
3.0.1 Thermodynamics laws 34
3.1 Thermodynamic Cycles 37
3.1.1 Quantum isothermal process 38
3.1.2 Quantum isochoric process 38
3.1.3 Quantum adiabatic process 38
3.2 Otto Engine 39
3.2.1 Otto Engine's Work and efficiency 39
3.2.2 Two-Level system QOE 40

Chapter 4: Enantiomer detection via Quantum Otto cycle 44
4.1 Introduction 44
4.2 Model System 46
4.3 Chiral Molecule Otto cycle 50
4.4 Results 55
4.4.1 Control parameter Φ 55
4.4.2 Control parameter δ 57
4.5 Conclusion 58

Chapter 5: Single Atom Heat Engine in a Tapered Trap 61
5.1 Introduction 61
5.2 Model System 63
5.2.1 Results 66
5.2.2 Parameters 66
5.2.3 The dynamics of the system 67
5.3 Effective Otto Cycle For the Radial Mode 71
5.3.1 Performance of the engine 72

5.4 Classical vs Quantum Heat Engine Regimes 74
5.5 Conclusion 77

Chapter 6: Atom-field interaction in a sub-diffraction hollow shape trap 79

6.1 Introduction 79
6.2 Generating a Sub-diffraction Blue-detuned Trap 80
6.2.1 Dipole Trap 82
6.3 Atom-Field Interaction 84
6.3.1 Scattering Ratio 84
6.3.2 Effects of the Thermal fluctuations on Scattering Ratio 85

Chapter 7: Conclusion 88

Bibliography 89

Appendix A: 107

.1 Effective entropy and temperature of the working mode a 107

LIST OF TABLES

LIST OF FIGURES

2.1 Schematic of two-level atom interacting with a field E. 6

2.2 The population of the ground and excited states, respectively shown by solid black and dashed blue lines for $\Delta = 0$ (a), $\Delta = 2\Omega$ (b). . . . 9

2.3 The inversion of the two-level system for $\Delta = 0$, $\Delta = 2\Omega$ cases is plotted by solid black and dashed blue lines. 9

2.4 Three possible configurations of the energy levels of a three-level atom. 12

2.5 Portrait of dipole traps with red and blue detuning, respectively, shown by a simple Gaussian laser beam and a Laguerre-Gaussian LG01 "doughnut" mode beam, providing the same potential depth and curvature in the trap center [R.Grimm et al., 2000] 19

2.6 Free Gaussian beam propagation along the z-axis with ω_0 as beam waist, and Z_R as Rayleigh range [Jährling and Saghafi, 2011]. 20

2.7 The original (blue dotted curve) and approximated (red solid curve) potential energies in an optical dipole trap are illustrated along the radial direction. They scale in terms of the maximal trap depth U_0 and the position in the beam waist w_0, showing that the second-order Taylor expansion is a good approximation for atoms occupying the bottom of the potential. 21

2.8 The image inversion interferometer is implemented as a Mach-Zehnder interferometer. It works with an appropriate delay in one arm and an image inverter in the other. The red and blue beams are perpendicular to each other and can not interfere [Tang et al., 2016]. 22

2.9 Dimensionless output electric field where x scaled by $\omega_0 = 1$ and $d = \omega_0/2$. 23

2.10 Dimensionless output intensity where x scaled by $\omega_0 = 1$ and $d = \omega_0/2$. Blue-dashed curves show the intensity of each beam separately, and the solid red curve indicates the interference output beam's intensity. The distance between two vertical black lines displays the FWHM. 24
2.11 The scaled pp vs d/ω_0. 24
2.12 The original (blue dotted curve) and approximated (red solid curve) potential energies in an optical dipole trap are illustrated along x direction. They scale in terms of the maximal trap depth U_0 and the position in the beam waist w_0 where $E_0 = 1$, showing that Taylor expansion is a good approximation for small values of x. 26
2.13 The electrical field $\boldsymbol{E}_{in}$ of a collimated beam with a Gaussian profile is converted into a focusing field $\boldsymbol{E}_f$ with a spherical wavefront by an ideal thin lens with a focal length f. 28
2.14 (a) Input $|F_0|^2$ and (b) focal $|F_+|^2$ dimensionless intensity. 29
2.15 (a) Input $|F_0|^2$ and (b) focal $|F_+|^2$ dimensionless intensity. 29
2.16 The schematic of an experimental setup to trap a single atom in a tight blue-detuned trap potential. The setup includes a balanced Mach-Zehnder interferometer and a lens system to focus the output beam in the focal point where a single atom is located. The interferometer contains an appropriate delay, Φ, in one arm and an image inverter in the other. We implement a self-interference technique to make a hollow shape beam before the first lens. After the first lens, the output beam propagates to the focal point. The inset figure shows the zoom-in of the trap potential in the focal point. 31
2.17 The dimensionless intensity distribution in focal point where $w_0 = d = 1.1$ mm, and $f = 4.5$ mm. The pick to pick in the focal point is calculated as $pp \approx 630$ nm. 32

3.1 Schematic of an Otto Cycle. 39
3.2 Evolution of the Two-level atom Eigen values vs detuning Δ. 41
3.3 Evolution of δE vs detuning Δ. 41
3.4 Evolution of efficiency $\eta(\%)$ vs detuning Δ. 43

4.1 (Color online) A schematic illustration of a left-handed (a) and right-handed (b) chiral molecule which is described by a three-level system with cyclic optical transitions. The three-level system is coupled with three classical optical drives of Rabi frequencies Ω_{12}, Ω_{13}, and $\pm\Omega_{23}$, where $+\Omega_{23}$ $(-\Omega_{23})$ describes the left-handed (right-handed) molecule. The detunings of the external optical drives from energy transitions are indicated by δ_{ij}. 47
4.2 (Color online) Energy eigenvalues of the Hamiltonian $H_{\rm int}^{\pm}$ for constant overall phase $\Phi = 0$ (a, b), and constant detuning $\delta = 0.1/\tau_0$ (c, d). The panels (a, c) and (b, d) represent left- and right-handed enantiomers, respectively. The eigenenergies are scaled with the rotational energy $E_0 = \hbar^2 B$ with the rotational constant B, that is why eigenenergies are $\pm 1E_0$ and $\pm 2E_0$ for $\Phi = \delta = 0$. The eigenvalues are obtained for time-independent Hamiltonian ($\Delta = 0$) and considering the unit magnitude of the Rabi frequencies Ω_{ij}. 48
4.3 (Color online) A schematic description of a quantum Otto cycle consisting of two isochore strokes ($A \to B$ and $C \to D$), and two adiabatic strokes ($B \to C$ and $D \to A$). During the hot isochore $A \to B$, Q_h heat is injected into the working medium from the hot bath of temperature T_h, and in the cold isochore $C \to D$, the working medium rejects Q_c into the cold bath of temperature T_c. During the adiabatic expansion $B \to C$ and compression $D \to A$, work is extracted and invested on the working medium, respectively. 52

4.4 (Color online) The error ε (Eq. (4.6)) in the assumption of thermalization calculated during the isochoric stages of the cycle as a function of the time (scaled by τ_0). Solid and dashed lines represent the thermalization of the system during the cold and hot isochore stages of the cycle. In the long time limit, the state of the three-level system $\rho(t)$ reaches the target thermal state $\rho_{\rm th}$ during the isochoric stages. . 54

4.5 (Color online) (a) Heat exchange Q_h with the hot bath and Q_c (scaled by E_0) with the cold bath as a function of the overall phase Φ of the optical drives with contant $\delta = 0.1/\tau_0$. The solid and dashed lines are for the right- and left-handed enantiomers. In addition, upper and lower horizontal lines represent heat Q_h injected into the system, and heat rejected Q_c into the cold bath is denoted by curved lines. (b) Work output W as a function of the phase Φ of the optical drives in the quantum Otto cycle operating between the hot and cold baths of inverse temperatures $\beta_h = 0.01$, and $\beta_c = 1$, respectively. The solid and dashed lines are for the left- and right-handed enantiomers, respectively. 56

4.6 (Color online) Work output W as a function of the detuning δ_2 (scaled by τ_0) supposing the optical drive fixed initially at resonance, $\delta_1 = 0$ and overall phase kept constant at $\Phi = 0$. The quantum Otto cycle operates between the hot and cold baths of inverse temperatures $\beta_h = 0.01$, and $\beta_c = 1$, respectively. The solid and dashed lines are for the left- and right-handed enantiomers. 57

4.7 (Color online) The engine's efficiency $\eta(\%)$ as a function of Φ, while detuning as a control parameter modifies from $\delta = 0$ to $\delta = 1/\tau_0$, in the quantum Otto cycle operating between the hot and cold baths of inverse temperatures $\beta_h = 0.01/\tau_0$, and $\beta_c = 1/\tau_0$, respectively. The solid and dashed lines are for the left- and right-handed Otto engines. 59

5.1 Cross sections of the approximate (Left panels) and exact (Right panels) funnel-shaped potential (in units of eV) of the tapered trap geometry. The approximation requires $z \tan\theta \ll r_0$ where $\theta = 30^o$ is the tapered trap angle and $r_0 = 1.1$ mm is the trap radius at $z = 0$. The calculations are done for the Calcium ion of mass $m = 40$u in atomic unit $u = 1.66 \times 10^{-27}$ kg. 63

5.2 Diagram of the heat engine system based on the radial (a) and axial (b) vibrational modes whose coupling is characterized by the parameter β. Radial mode is coupled to two thermal baths at temperatures T_h and T_a, where the coupling to the bath at temperature T_h is periodically turned on and off, and the axial mode is coupled to a bath at temperature T_b. The background environment common to both modes is not shown. 65

5.3 Dynamics of the mean number of vibrational phonons $\langle n_z \rangle$ in modes b where time is scaled with ω_z. The parameters used in the plots are taken to be $\omega_r/2\pi = 1$ MHz, $\omega_z/2\pi = 50$ kHz, $\bar{n}_h = 3$, and $\beta/2\pi = 100$ kHz. The solid black, dotted blue, dash-dotted green, and dashed red lines show the evolution of $\langle n_z \rangle$ under the models A_0, A_1, A_2, and A_3, respectively. 69

5.4 The time evolutions of the variances of the quadratures $(\langle \Delta \hat{q}_r \rangle)^2$ (red dotted line) and$(\langle \Delta \hat{p}_r \rangle)^2$ (blue solid line) of the radial mode. The inset magnifies the squeezing region where Variance $< 1/4$. 70

5.5 Colour online)(a)-(c) The Wigner functions in the p_r, q_r field quadrature phase space of the radial mode plotted for (a) $\beta/2\pi = 10$ kHz, (b) $\beta/2\pi = 100$ kHz, (c) $\beta/2\pi = 200$ kHz. The other system parameters are $\omega_r/2\pi = 1$ MHz, $\omega_z/2\pi = 50$ kHz. 71

5.6 Effective energy-frequency diagram of the radial mode a by considering the dependence of the mean effective energy U to the effective frequency ω_{eff} (in units of $\hbar\omega_z$). 73

5.7 T-S diagram of the mode a which closely resembles that of an Otto engine (in units of $\hbar\omega_z$) 74
5.8 Extracted work W (in unit of $\hbar\omega_z$) versus trap's radius r_0 (μm) where radial and axial frequencies are constant ($\omega_r/2\pi = 1$ MHz, and $\omega_z/2\pi = 50$ kHz) and $\theta = \pi/4$. 75
5.9 The maximum dissipated power (in units of $\hbar\omega_z$) concerning coupling constant β (in units of kHz). The black dashed and solid blue curves show the results of classical and quantum simulations, respectively. . 77

6.1 The schematic of an experimental setup to trap a single atom in a tight blue-detuned trap potential. The setup includes a balanced Mach-Zehnder interferometer and a lens system to focus the output beam in the focal point where a single atom is located. The interferometer contains an appropriate delay, Φ, in one arm and an image inverter in the other. We implement a self-interference technique to make a hollow shape beam before the first lens. After the first lens, the output beam propagates to the focal point. The inset figure shows the zoom-in of the trap potential in the focal point. 81
6.2 The normalized intensity distribution of the incident light where $w_0 = 331$ μm, $z = z_0 = 276$ mm, and $\lambda = 632.8$ nm. The plot is scaled by $\lambda = 1$, and we consider $d = w_0$ where the peak-to-peak diameter of the beam is obtained as $pp = 1118$ λ. 82
6.3 The designed intensity on the focal plane at $z = z_0 + f$, where the plot is scaled by $\lambda = 1$ and focal length is $f = 600$ λ, and the focal beam's peak-to-peak diameter is $pp_f \approx 0.59$ λ. 83

6.4 The scattering ratio R_{sc} vs. focusing strength u for different trap frequencies in constant temperature $T = 10$ μK. The dashed black curve displays the scattering ratio in focus, while the solid curves demonstrate R_{sc} for frequencies 0.5, 0.75, and 1 MHz down to up, respectively. 87

ABBREVIATIONS

QHE	Quantum Heat Engine
QOC	Quantum Otto Cycle
MOT	Magneto-Optical Trap

Chapter 1

INTRODUCTION

"Consider any machine—for example, an automobile— and ask about the problems of making an infinitesimal machine like it [Feynman, 1960]."

Proficiency in manipulating small quantum systems is necessary for quantum machines. Atoms on a small scale behave like nothing on a large scale, for they satisfy the laws of quantum mechanics [Feynman, 1960]. On the other hand, exchange energy performs by photons representing a quantum of light interacting with atoms. Therefore, investigating the light, matter, and their interaction forms our knowledge of the quantum world. Our visions of light and matter have followed an impulsive evolution, culminating with the discovery of the atom and formulation of the theories of electrodynamics and quantum mechanics. Integrating those two theories provide us with a reasonable point of view.

Quantum machines implementing atom-field interaction are employed in a wide area of modern technology. In the past decades, there has been a continuous technical devices' size reduction from the macroscale to the nanoscale, approaching the leading restriction of single atoms. The miniaturization process puts the thermodynamics of single particles and nanosystems into the research focus. In a broad context, quantum heat engine (QHE) is a thermal machine whose operation cycle requires a quantum mechanical description [Geusic et al., 1967, Kosloff and Levy, 2014a]. The first quantum heat engine was introduced by Scovil et al. as a three-level master quantum device that amplifies microwave radiation [Geusic et al., 1967]. More methodical studies of QHE have attracted much attention quite recently [Dawkins et al., 2019, Kieu, 2004, Quan et al., 2005, Quan et al., 2007c, Scully et al., 2011, Altintas et al., 2014, Abah et al., 2012, Bergenfeldt et al., 2014, Roßnagel

et al., 2014, Altintas et al., 2015, Zhang and Zhang, 2017, Naseem and Mustecaplıoglu, 2019, Barontini and Paternostro, 2019, Wang et al., 2012, Steeneken et al., 2011, Kaur et al., 2021, Ghosh et al., 2019, Brantut et al., 2013, Blickle and Bechinger, 2012, Hugel et al., 2002, Martinez et al., 2016, Zhang, 2020, Naseri-Karimvand et al., 2022, Metcalf and van der Straten, 1999, Levy et al., 2020, Levy et al., 2016, Lindenfels et al., 2019, Sheng et al., 2021, Xu et al., 2021, Gelbwaser-Klimovsky and Kurizki, 2015, Huang et al., 2018, He et al., 2012]. A specific example is the quantum Otto cycle, where the slow quantum adiabatic parametric processes replace its classical counterpart's fast isentropic compression and expansion strokes [Kosloff and Levy, 2014b, Kosloff and Rezek, 2017, Izadyari et al., 2022b, Altintas and Mustecaplıoglu, 2015, Singh et al., 2021]. Different quantum working substances have been proposed to execute the quantum Otto cycle [Scovil and Schulz-DuBois, 1959a, ScullyM et al., 2012, N. Brunner and Skrzypczyk, 2012, Hewgill et al., 2020, Naseem et al., 2020, Insinga et al., 2016]. We question if a quantum Otto cycle can be employed as an examination to discriminate systems with identical energy spectrums but with distinct spectral changes under the same parametric processes. A chiral molecule is a characteristic system with such a spectral character, and for which this question is incredibly consequential. Chiral molecules can have either left- or right-handed geometries called enantiomers that are not superimposable on their mirror images [Fox and Whitesell, 1974, Woolley, 1976]. Chiral molecules may exist as a mixture of enantiomers in varying proportions. Therefore, enantioseparation is a critical and challenging task in chemistry and medicine [Chen et al., 2022, Ye et al., 2021, Kondru et al., 1998, Bielski and Tencer, 2005, Ye et al., 2019, McKendry et al., 1998, Bielski and Tencer, 2007]. We investigate the possibility of manipulating thermodynamic processes for enantiomer detection. In particular, we operate a quantum Otto cycle, in which a chiral molecule described by a three-level system with cyclic optical transitions is considered a working medium. Applying an Otto cycle, we show a method to distinguish left- and right-handed enantiomers according to extracted work measurement.

Moreover, the Otto engine can be performed with a single-atom configuration

in a trap. In 2016, Roßnagel et al. presented a pioneering experiment demonstrating a piston-type (Otto) engine employing a single trapped ion [Roßnagel et al., 2016]. However, they did not report any genuine, profound quantum effects in the single-atom piston due to the relatively small energy gaps of the trapped ion at the involved temperatures. In Sec. 5, we ask if it is sufficient to lower the temperature to bring the experimental setup to the quantum regime, or it is necessary to make more modifications. To answer this question, we use a higher-order, so-called quadratic, optomechanical model of the interaction between the motional degrees of freedom of the atom arising due to the tapered trap geometry of the experiment. We demonstrate that more than reducing the temperature of the experiment [Roßnagel et al., 2016], making the trap geometry more asymmetric and the atom more confined are required to make quantum squeezing-type correlations, and it significantly increases the engine's performance rather than the classical stochastic engine.

To make the atom more confined, we persist in examining diploe trap geometry. A single atom can be confined in a dipole trap after cooling inside a magneto-optical trap (MOT) [Foot, 2005]. We indicate how a tight dipole trap can be designed by employing a Gaussian beam using a lens system to focus the beam and the self-interference technique presented in Ref. [Tang et al., 2016]. We introduce a method to make a tight blue-detuned trap with a radius of under-diffraction limit. Also, we show that a more confined trap enhances the atom-field coupling strength by developing the original theoretical model of atom-light interaction in realistic focusing geometries by considering the thermal fluctuations of the atom [Teo and Scarani, 2011].

The rest of the thesis is organized as follows. In Secs. 2 and 3, we describe and shortly review atom-field interaction and quantum thermodynamics. In Sec. 4, we introduce a chiral cyclic three-level Otto cycle for different enantiomers and discuss how they can be distinguished. We study the performance of a single-atom Otto engine in a tapered trap in Sec. 5. A sub-diffraction dipole trap configuration is presented in Sec. 6, where the atom-field interaction is examined in free space using a lens system.

Finally, we conclude in Sec. 7.

Chapter 2

THE PRINCIPLES I (ATOM-FIELD INTERACTION)

2.1 Two-Level Atom-field Interaction

A two-level system is a simple but fundamental means in quantum optics. Physically, the two-level system can be any quantum system with two energy levels which are nothing more than combinations of transformations in the appropriate vector space representing the quantum states under consideration. These transformations correspond to physical processes implemented through the interaction of the two-level system with another quantum or even a classical system. In quantum optics, such interactions explore and elucidate the quantum and statistical properties of the electromagnetic field. An atom interacting with an electromagnetic field with a frequency close to the transition frequency between a particular pair of atomic eigenstates represents a two-level system to a perfect approximation.

2.1.1 Atom interaction with a Classical Field

In a two-level atom, $|g\rangle$ and $|e\rangle$ denote the ground and excited states of an atom, with respective energies $E_g = \hbar\omega_g$ and $E_e = \hbar\omega_e$, respectively, shown schematically in Fig. 3.1. The corresponding frequency of the atomic transition $|g\rangle \rightarrow |e\rangle$ is $\omega_{eg} = \omega_e - \omega_g$. The Hamiltonian for the atom put in an electromagnetic field is

$$H = H_A + H_{AF}(t), \tag{2.1}$$

where $H_A = \hbar\,|g\rangle\,\langle g|\,\omega_g + \hbar\,|e\rangle\,\langle e|\,\omega_e$, and $H_{AF} = -\boldsymbol{\mu}.\boldsymbol{E}(t) = -\mu E(t)$.
$\mu = \boldsymbol{\mu}.\hat{\epsilon}$ is the projection of the electric dipole operator on the polarization direction $\hat{\epsilon}$ of the electric field of amplitude

$$E(t) = 2|E_0|\cos(\omega t + \phi) \tag{2.2}$$

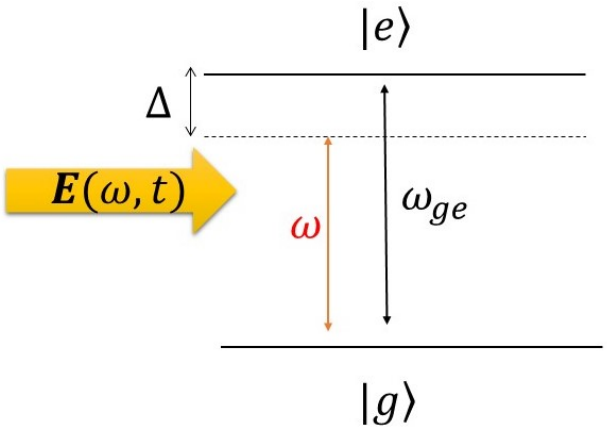

Figure 2.1: Schematic of two-level atom interacting with a field E.

Here, ω and ϕ are the frequency and the phase of the classical monochromatic field electric field (considering $E_0 = |E_0| \exp(-i\phi)$). The state of the atom at any time can be represented as

$$|\Psi(t)\rangle = c_g(t)\,|g\rangle + c_e(t)\,|e\rangle\,, \tag{2.3}$$

where c_g and c_e are the time-dependent complex amplitudes of the atomic eigenstates $|g\rangle$ and $|e\rangle$. According to the Schrodinger equation, the time-evolution of $\psi(t)$ is

$$\frac{\partial\,|\psi(t)\rangle}{\partial t} = -\frac{i}{\hbar} H\,|\psi(t)\rangle\,, \tag{2.4}$$

where we consider $c_g(0) = 1$ and $c_e(0) = 0$, as the initial condition i.e., the system is assumed to be initially in its ground state $|g\rangle$.
To simplify, the Schrodinger equation (2.4) for two states can be written in a matrix form. Substituting Eq. (2.3)

$$\frac{\partial}{\partial t}\begin{pmatrix} c_g \\ c_e \end{pmatrix} = -\frac{i}{\hbar}\begin{pmatrix} \omega_g & \mu_{ge}(E_0 e^{-i\omega t} + E_0^* e^{i\omega t}) \\ \mu_{eg}(E_0 e^{-i\omega t} + E_0^* e^{i\omega t}) & \omega_e \end{pmatrix}\begin{pmatrix} c_g \\ c_e \end{pmatrix}, \tag{2.5}$$

where $\mu_{ij} = \langle i|\,\mu\,|j\rangle$, while We have supposed that the diagonal matrix elements of μ are zero. we acquire the differential equations for the slowly varying amplitudes

$\tilde{c}_k(t)$ by making the transformations $c_k(t) = \tilde{c}_k(t)\exp(-i\omega_k t)$ for $(k = g, e)$, which is analogous to adopting the interaction picture.

$$\frac{\partial}{\partial t}\begin{pmatrix}\tilde{c}_g\\ \tilde{c}_e\end{pmatrix} = \frac{i}{\hbar}\begin{pmatrix}\tilde{c}_e\mu_{ge}E_0^* e^{i\Delta t}\\ \tilde{c}_g\mu_{eg}E_0 e^{-i\Delta t}\end{pmatrix}, \tag{2.6}$$

where $\Delta = \omega - \omega_{eg}$ is the detuning from the resonance frequency ω_{eg}. In the near-resonant transitions, $\Delta \ll \omega_{eg} \approx \omega$, so the rotating wave approximation (RWA) can be applied. In RWA, the terms involving the exponentials $\exp[\pm(\omega + \omega_{eg})]$ are neglected, i.e., oscillating with the sum frequencies $\pm(\omega + \omega_{eg})$, as opposed to those oscillating with the small difference frequencies $\pm\Delta$.

In the following, the obtained differential equation is solved by introducing $\Omega = \mu_{ge}E_0/\hbar$ called Rabi frequency. The Hamiltonian of the system can be written as

$$H = \begin{pmatrix}0 & \Omega^* e^{i\Delta t}\\ \Omega e^{-i\Delta t} & 0\end{pmatrix}. \tag{2.7}$$

The system's state $|\Phi(t)\rangle = [\tilde{c}_g \quad \tilde{c}_e]^T$ can be written in a new basis $|\Psi(t)\rangle = R\,|\Phi(t)\rangle$ where R is a unitary matrix

$$R = \begin{pmatrix}1 & 0\\ 0 & e^{i\Delta t}.\end{pmatrix} \tag{2.8}$$

Considering $\hbar = 1$, the Schrodinger equation will be

$$\begin{aligned} i\frac{\partial}{\partial t}(R(t)\,|\Phi(t)\rangle) &= H(R(t)\,|\Phi(t)\rangle)\\ i\frac{\partial}{\partial t}\,|\Phi(t)\rangle &= (R^\dagger(t)HR(t) - iR^\dagger(t)\frac{\partial R(t)}{\partial t})\,|\Phi(t)\rangle\,, \end{aligned} \tag{2.9}$$

where we can introduce the effective Hamiltonian in a new basis

$$H_{eff} = \begin{pmatrix}0 & \Omega^*\\ \Omega & \Delta\end{pmatrix}. \tag{2.10}$$

We will employ these unitary transformations in the following problems to simplify the Hamiltonian of the system. Now, we return to Eq. (2.6) to solve the differential equations by the Laplace method. This method enables us to solve more complicated

systems like three-level atoms' interacting with the external field. The Laplace transformation can be introduced by [Lambropoulos and Petrosyan, 2007]

$$L(u) = \int_0^\infty dt e^{-ut} a(t), \tag{2.11}$$

Using properties of the Laplace transform $\int_0^\infty e^{-}ut\dot{a}(t) = uL(u) - a(0)$ and considering that the atom initially is in its ground state, the Laplace function can be obtained from 2.6

$$L_g(u) = \frac{u - i\Delta}{u^2 - i\Delta u + \Omega^2} \tag{2.12}$$

The roots of the denominator are $u_\pm = i(\Delta/2 \pm \sqrt{\Omega^2 + (\Delta^2/2)^2})$, andby employing the inverse Laplace transform of $L_g(u)$

$$\tilde{c}_g(t) = \frac{u_+ - i\Delta}{u_+ - u_-} e^{u_+ t} - \frac{u_- - i\Delta}{u_+ - u_-} e^{u_- t} \tag{2.13}$$

Simplifying Eq. 2.13 and applying the same method for $c_e(t)$,

$$\begin{aligned} \tilde{c}_g(t) &= e^{i\Delta t/2} \left[\cos\big(\bar{\Omega} t\big) - i \frac{\Delta}{2\bar{\Omega}} \sin\big(\bar{\Omega} t\big) \right] \\ \tilde{c}_e(t) &= i e^{-i(\frac{\Delta t}{2} + \phi)} \frac{\Omega}{\bar{\Omega}} \sin\big(\bar{\Omega} t\big), \end{aligned} \tag{2.14}$$

where $\bar{\Omega} = \sqrt{\Omega^2 + (\Delta/2)^2}$ defined as effective Rabi frequency.where $\bar{\Omega} = \sqrt{\Omega^2 + (\Delta/2)^2}$ defined as effective Rabi frequency. In Fig. 2.2, we plotted the population of the system $P_i(t) = |\tilde{c}_i|^2$ as a function of the time where $(i = e, g)$ show the population of the ground and excited states. The solid black and dashed blue lines indicate two cases $\Delta = 0$ and $\Delta = 2\Omega$, respectively.

Furthermore, population inversion is defined as $D_{inv}(t) = P_e - P_g$, showen in Fig. 2.3 where the solid black and dashed blue lines indicate plotted in conditions of $\Delta = 0$ and $\Delta = 2\Omega$, respectively.

2.1.2 The Jaynes-Cummings model

Consider the interaction of a single atom with the quantized field of a cavity. We suppose that the cavity's frequency ω is near-resonant with the frequency ω_{eg} of the atomic transition. The total Hamiltonian for the system is given by,

$$H = H_A + H_F + V_{AF}, \tag{2.15}$$

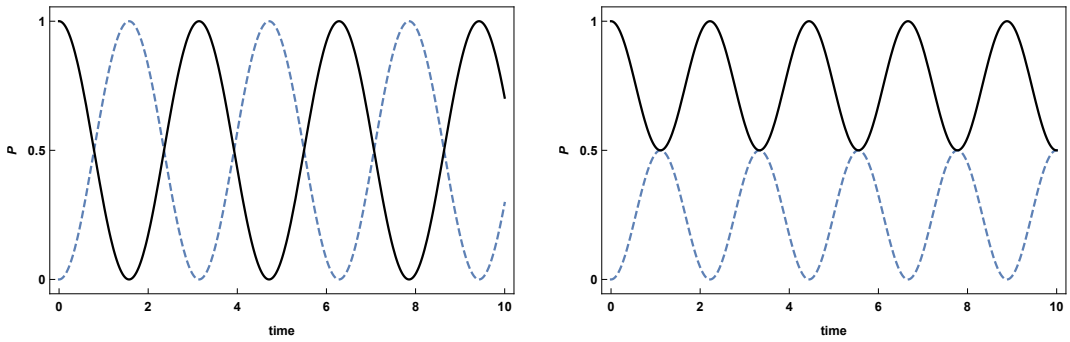

(a) (b)

Figure 2.2: The population of the ground and excited states, respectively shown by solid black and dashed blue lines for $\Delta = 0$ (a), $\Delta = 2\Omega$ (b).

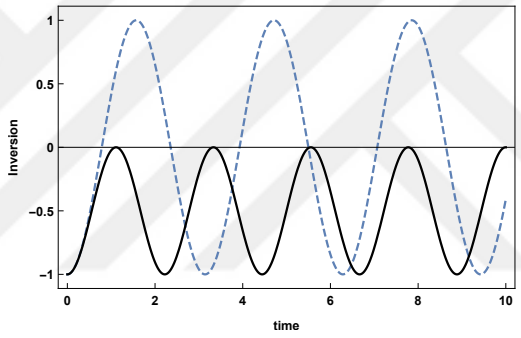

Figure 2.3: The inversion of the two-level system for $\Delta = 0$, $\Delta = 2\Omega$ cases is plotted by solid black and dashed blue lines.

The first and second terms describe the atom and the cavity field Hamiltonians. V_{AF} is the atom–field interaction. Considering a two-level atom, we can introduce the atomic transition (Pauli) operators as, $\sigma_z = (|g\rangle\langle g| - |e\rangle\langle e|)$, $\sigma_+ = |e\rangle\langle g|$ and $\sigma_- = |g\rangle\langle e|$. Accordingly, the Hamiltonian of a two-level atom is

$$H_A = \frac{1}{2}\hbar\omega_{eg}\sigma_z. \tag{2.16}$$

We choose the zero point of energy halfway between levels as $E_e = \hbar\omega_{eg}/2$ and $E_g = -\hbar\omega_{eg}/2$.

The Hamiltonian for the cavity field is $H_F = \hbar\omega a^\dagger a$, where $a^\dagger$ and a are the creation and annihilation operators for the field mode. Finally, in the dipole approximation, the atom–field interaction has the standard form $V_{AF} = -\vartheta E(z_0)$, where the electric

field at the atomic position z_0 is given by $E(z_0) = \epsilon_\omega(a + a^\dagger)\sin(kz_0)$ with $\epsilon_\omega = \sqrt{\hbar\omega/\varepsilon_0 V}$ being the field per photon within the cavity volume V . Representing the dipole moment operator as

$$\vartheta = \vartheta_{ge}\sigma_- + \vartheta_{eg}\sigma_+, \tag{2.17}$$

and introducing the atom–cavity field coupling constant $g \equiv -(\vartheta_{ge}\varepsilon_\omega/\hbar)\sin(kz_0)$, we can write [Lambropoulos and Petrosyan, 2007]

$$V_{AF} = \hbar g(\sigma_+ + \sigma_-)(a + a^\dagger), \tag{2.18}$$

where g is assumed real.

In the rotating wave approximation, the total Hamiltonian describing a two-level system coupled to a single-mode electromagnetic field is known as the Jaynes–Cummings model, will be

$$H = \frac{1}{2}\hbar\omega_{eg}\sigma_z + \hbar\omega a^\dagger a + \hbar g(\sigma_+ a + \sigma_- a^\dagger). \tag{2.19}$$

2.1.3 Spontaneous Emission

In the previous section, the wave function of the total Hamiltonian included only the purely oscillatory behavior associated with the eigenvalues and the $C_k(t)$'s radiation-induced time dependence. That discussion omitted the spontaneous decay of the excited states resulting from their interaction with the zero-point energy of the electromagnetic field. Spontaneous emission has played an essential role in atomic physics since Bohr conceived discrete atomic states. The spontaneous emission causes a pure state to evolve into a mixed state because only the atom and the laser field are considered, not the spontaneously emitted light. This greatly simplifies the description because the spontaneously emitted light can travel in many different directions and have different polarizations. The number of modes is infinite, and this complicates the situation enormously. Also, spontaneous emission cannot be addressed appropriately within the framework of a semiclassical definition of the electromagnetic field because vacuum fluctuations of the field induce it[Metcalf and van der Straten, 1999]. Consider an atom in the excited state at t_0 and no photons in the

radiation field. The system is in a pure state $|e0\rangle$, where the first parameter in the ket represents the atom's state, and the zero indicates the absence of photons in the field. The system transitions from the excited to the ground state presented by spontaneous emission, emitting one photon into the radiation field. Then the state is denoted by $|g1_s\rangle$ with $s = (\mathbf{k}, \epsilon)$, the mode of spontaneous emission, where the direction of the emitted photon is explicitly indicated by its wavevector $\mathbf{k}$ and its polarization by ϵ. The state of the system can now be described by

$$\Psi(t) = c_{e_0} e^{-i\omega_e t} |e_0\rangle + \sum_s c_{g_1} e^{-i(\omega_g+\omega)t} |g_{1_s}\rangle , \tag{2.20}$$

where s denotes all possible modes and ω must be replaced by kc. The Hamiltonian of the system has to be defined by the quantization of the electromagnetic field, which will not be mentioned here. However, the atom-field interaction is the only part of the Hamiltonian that couples the two states. This coupling is equivalent to its semiclassical counterpart, and the result for the time evolution of the two states is [Metcalf and van der Straten, 1999]

$$\begin{aligned} i\frac{dc_{e_0}(t)}{dt} &= \sum_s c_{g_1 s}(t)\Omega_s e^{-i(\omega-\omega_{eg})t}, \\ i\frac{dc_{g_1 s}(t)}{dt} &= c_{e_0}(t)\Omega_s^* e^{i(\omega-\omega_{eg})t}. \end{aligned} \tag{2.21}$$

By simplifying the differential equation for the excited state, we will have

$$\frac{dc_{e_0}(t)}{dt} = -\frac{\gamma}{2} c_{e_0}(t), \tag{2.22}$$

where

$$\gamma = \frac{\omega^3 \mu^2}{3\pi\epsilon_0 \hbar c^3}. \tag{2.23}$$

Since the amplitude of the excited state decays at a rate of $\gamma/2$, the population of the state decays with γ and the lifetime of the excited state becomes $T = 1/\gamma$. The decay of the excited state is irreversible. In principle, the modes of the spontaneously emitted light are also coupled to the ground state but there is an infinite number of modes in free space. The amplitude for the reverse process has to be summed over these modes. Since the different modes add destructively, the probability for the reverse process becomes zero.

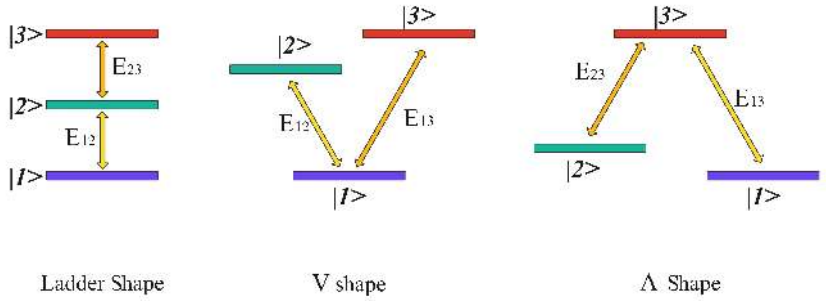

Figure 2.4: Three possible configurations of the energy levels of a three-level atom.

2.2 Three-level System

An atom consists of an infinite number of discrete levels corresponding to the bound states of the electron. As an extension of the two-level model, we consider a three-level atom whose energy levels are introduced by $|1\rangle$, $|2\rangle$, and $|3\rangle$. The three possible configurations of atomic levels are the ladder ($\equiv$), $\vee$, and $\wedge$ shapes. Also, we will discuss a cyclic configuration that can be seen in molecules and artificial atoms in Sec. 4. To introduce some applications, we continue to study the $\wedge$ configuration of atomic levels in more detail. By definition, the ground state $|1\rangle$ is stable while $|2\rangle$ is metastable (long-lived), which is called the Raman configuration [Lambropoulos and Petrosyan, 2007]. The Hamiltonian for the three-level system takes the form

$$H = H_A + H_{int}(t). \tag{2.24}$$

Here $H_A = \hbar \sum_{i=1}^{3} \omega_{ii}\sigma_{ii}$, and atom-field interaction Hamiltonian is

$$H_{int}(t) = -\sum_{j=1,2} \vartheta_{j3}\varepsilon_{j3}e^{-i\omega_{j3}t} + c.c., \tag{2.25}$$

where $\vartheta_{ab} = \langle a|\boldsymbol{\vartheta}.\boldsymbol{\epsilon}_{ab}|b\rangle$ is the dipole matrix element for the corresponding atomic transition $|a\rangle \leftrightarrow |b\rangle$. The intracting electric field is $E_{ab} = \boldsymbol{\epsilon}_{ab}(\varepsilon_{ab}\exp(-i\omega_{ab}t) + c.c.)$, where $\boldsymbol{\epsilon}$ shows the polarization of the field.

Considering the state vector of the system as

$$\psi(t) = c_1(t)|1\rangle + c_2(t)|2\rangle + c_3(t)|3\rangle \tag{2.26}$$

Using Schrodinger equation in RWA regime,

$$\begin{aligned}
\frac{\partial c_1}{\partial t} &= -i\omega_1 c_1 + ic_3\Omega_{13}\exp(i\omega_{13}t),\\
\frac{\partial c_2}{\partial t} &= -i\omega_2 c_2 + ic_3\Omega_{23}\exp(i\omega_{23}t),\\
\frac{\partial c_3}{\partial t} &= -i\omega_3 c_3 + ic_1\Omega_{13}\exp(-i\omega_{13}t) + ic_2\Omega_{23}\exp(-i\omega_{23}t),
\end{aligned} \tag{2.27}$$

where $\Omega_{ij} = \vartheta_{ij}\varepsilon_{ij}/\hbar$ is the Rabi frequency of the fields on the corresponding transitions.

By transforming $c_i(t) = c_i^{'}(t)\exp(-i\omega_i)$, where $(i = 1, 2, 3)$, we transform the set of amplitude equations to the rotating frame,

$$\begin{aligned}
\frac{\partial c_1^{'}}{\partial t} &= i\Omega_{13}c_3^{'},\\
\frac{\partial c_2^{'}}{\partial t} &= i(\Delta_1 - \Delta_2)c_2^{'} + i\Omega_{23}c_3^{'},\\
\frac{\partial c_3^{'}}{\partial t} &= i\Delta_1 c_3^{'} + i\Omega_{13}c_1^{'} + i\Omega_{23}c_2^{'},
\end{aligned} \tag{2.28}$$

where, $\Delta_1 = \omega_1 - \omega_{13}$ and $\Delta_2 = \omega_2 - \omega_{23}$ are the detunings of the fields from the corresponding atomic transitions. So, the Hamiltonian of the system in the basis of bare atomic eigenstates ($|1\rangle$, $|2\rangle$, $|3\rangle$) can be written as

$$H_\wedge = -\hbar\begin{bmatrix} 0 & 0 & \Omega_{13}^* \\ 0 & (\Delta_1 - \Delta_2) & \Omega_{23}^* \\ \Omega_{13} & \Omega_{23} & \Delta_1 \end{bmatrix}. \tag{2.29}$$

Considering the case of small and equal detuning $\Delta_1 = \Delta_2 \equiv \Delta \ll \Omega_{ij}$, the eigenvalues of the Hamiltonian are

$$\begin{aligned}
E_0 &= 0,\\
E_\pm &= \frac{1}{2}\left(-\Delta \pm \bar{\Omega}\right),
\end{aligned} \tag{2.30}$$

where, $\bar{\Omega} \equiv \sqrt{4\Omega_{13}^2 + 4\Omega_{23}^2 + \Delta^2}$, and the corresponding normalized eigenvectors are

$$\begin{aligned}
|D\rangle &= \frac{1}{\sqrt{N_0}}(\Omega_{23}|1\rangle - \Omega_{13}|2\rangle),\\
|B_\pm\rangle &= \frac{1}{\sqrt{N_\pm}}(\Omega_{13}|1\rangle + \Omega_{23}|2\rangle - E_\pm|3\rangle),
\end{aligned} \tag{2.31}$$

where, $N_0 = \Omega_{13}^2 + \Omega_{23}^2$ and $N_\pm = N_0 + E_\pm^2$ are the normalization coefficients. The eigenstate with zero energy $|D\rangle$ is called the Dark state since it does not contain the excited state $|3\rangle$, which decays by spontaneous emission. On the other hand, the eigenstates $|B_\pm\rangle$ are called the Bright states. According to Eq. (2.31), the Dark state represents an atom subject to two fields with Rabi frequencies, which can be prepared in a coherent superposition state. For this reason, this state is also called the coherent population trapping (CPT) state. The CPT is implemented in various areas of the quantum optics, such as electromagnetically induced transparency on field propagation in atomic media [Fleischhauer et al., 2005] and coherent population transfer [Vitanov et al., 2017].

2.3 Atom Trap

Experiments storing and trapping charged and neutral particles have often been the key to promising scientific approaches. Over the last two decades, the ultra-low-energy region developed experimentally accessible due to the dramatic outcomes in laser cooling and trapping, which have taken place [Metcalf and van der Straten, 1999, Letokhov et al., 1995, Cohen-Tannoudji et al., 1998]. It has improved an experimental routine to have ensembles of neutral atoms in the micro-kelvin region, and many experiments are being designed with laser-cooled ultra-cold gases. It is thus possible to trap the neutral atoms by much weaker mechanisms than the Coulomb interaction. Traps for neutral atoms can be learned based on three different interactions [R.Grimm et al., 2000].

Optical dipole traps depend on the far-detuned electric dipole interaction, which is much weaker than all trapping mechanisms. The trap depths are in the range below one millikelvin. The light-induced mechanisms do not restrict the optical trap in radiation pressure traps since the excitation can be kept extremely low. The trapping mechanism is independent of the particular sub-level of the electronic ground state under suitable conditions. The internal ground-state dynamics can thus be fully exploited for experiments, and a great variety of different trapping geometries can be realized.

The powerful Coulomb interaction is used to trap charged particles' by trapping them in electric or electromagnetic fields [Herfurth and Blaum, 2008]. Single ions exhibit various impressive quantum effects at the very low temperatures reached by laser cooling [Wineland et al., 2003, Cirac et al., 1996], and ensembles form a crystalline ordered state [Walther, 1993]. Laser cooling in ion traps has opened up new prospects for ultrahigh precision spectroscopy and related fundamental applications. More remarkably, the confining mechanism does not rely on the internal structure of the ion, which is therefore accessible for all kinds of experiments.

2.3.1 Paul Trap

The quadrupole ion trap, or the Paul trap, is a device that can confine charged particles employing interactions between electric fields [Paul, 1990]. Due to Earnshaw's theorem, we know that charged particles cannot be trapped stably by static electric fields alone. The quadrupole is the most straightforward electric field geometry utilized in such traps. The Paul trap operates AC voltage to generate alternating electric fields on a pair of hyperbolic electrodes suspended on either side of a ring electrode. Ion traps are practical because they let us isolate individual charged particles over long periods, which we can observe and use in experiments. Microfabricated ion traps exist where the electrodes lie in a plane with the trapping region above the plane.

2.3.2 Magneto-Optical Trap (MOT)

Employing optical and magnetic fields present the most famous trap for neutral atoms called magneto-optical trap (MOT), demonstrated in 1987 [Raab et al., 1987]. The operation of a MOT depends on both inhomogeneous magnetic fields and radiative selection rules to exploit optical pumping and the strong radiative force [Raab et al., 1987, Metcalf, 1989]. The radiative interaction provides cooling that helps in loading the trap and enables a straightforward process. The trap is easy to construct because it can be operated with a room-temperature cell where alkali atoms are captured from the vapor [Metcalf and van der Straten, 1999].

2.4 Dipole Trap

In this section, we concentrate on dipole traps obtained with far-detuned light. In these traps, an ultracold ensemble of atoms captured from the magneto-optical trap is conned in a nearly conservative potential well with feeble influence from spontaneous photon scattering.

2.4.1 Model system

In interacting atoms with far-detuned light, the optical excitation is very low, and the radiation force due to photon scattering is negligible compared to the dipole force. The optical dipole force arises from the dispersive interaction of the induced atomic dipole moment with the intensity gradient of the light field [Cook, 1979, Gordon and Ashkin, 1980]. Because of its conservative character, the force can be derived from potential, the minima of which can be used for atom trapping. The basic equations for the dipole potential and the scattering rate is driven by considering the atom as a simple oscillator subject to classical radiation. When an atom is placed into laser light, the electric field E induces an atomic dipole moment p that oscillates at the driving frequency ω.

According to the classical Lorentz model, an atom is taken with complex polarizability $\alpha(\omega)$ exposed to the electric field [Foot, 2005]:

$$\boldsymbol{E}(\boldsymbol{r},t) = \hat{\epsilon}\tilde{E}(\boldsymbol{r})e^{-i\omega t} + c.c. \tag{2.32}$$

where $\hat{\epsilon}$ is the polarization, ω and $\tilde{E}$ are the frequency and amplitude of the electric field, respectively. The electric field induces a dipole moment

$$\boldsymbol{P}(\boldsymbol{r},t) = \alpha\boldsymbol{E}(\boldsymbol{r},t) \tag{2.33}$$

Here oscillates with $\boldsymbol{E}$ and has an amplitude

$$\tilde{p} = \alpha\tilde{E}. \tag{2.34}$$

The interaction potential of the induced dipole moment in the driving field is given

by

$$U_{dip} = -\frac{1}{2}\langle \boldsymbol{P}.\boldsymbol{E}\rangle_t = -\frac{1}{2\epsilon_0 c} Re(\alpha) I, \tag{2.35}$$

where $I = 2\epsilon_0 c|\tilde{E}|^2$ is the light intensity, and the angular brackets denote the time average over the rapidly oscillating terms. So, the atom's potential energy in the field is proportional to the intensity I and the real part of the polarizability. It describes the in-phase component of the dipole oscillation responsible for the interaction's dispersive properties. From the gradient of the interaction potential, the dipole force can be obtained

$$\boldsymbol{F}_{dip}(\boldsymbol{r}) = -\boldsymbol{\nabla} U_{dip}(\boldsymbol{r}) = -\frac{1}{2\epsilon_0 c} Re(\alpha) \boldsymbol{\nabla} I(\boldsymbol{r}), \tag{2.36}$$

The imaginary part of the polarizability accounts for energy absorption from the driving field. It contributes to the out-of-phase component of the electronic oscillation. The absorbed power is

$$P = \langle \dot{p}.\boldsymbol{E}\rangle_t = \frac{\omega}{\epsilon_0 c} Im(\alpha) I \tag{2.37}$$

The absorption can be interpreted as photon scattering in absorption cycles and subsequent spontaneous re-emission processes by considering the light as a stream of photons $\hbar\omega$. The corresponding scattering rate is

$$\Gamma_{sc}(\boldsymbol{r}) = \frac{P}{\hbar\omega} = \frac{1}{\hbar\epsilon_0 c} Im(\alpha) I(\boldsymbol{r}) \tag{2.38}$$

The interaction potential and the scattered radiation power have been expressed in the two primary quantities of interest for dipole traps in terms of the position-dependent field intensity $I(\boldsymbol{r})$ and the polarizability $\alpha(\omega)$.

2.4.2 Atomic polarizability

To calculate its polarizability α, the atom is considered in Lorentz's model of a classical oscillator where an electron with mass m_e, elementary charge e is oscillating with frequency ω_0 corresponding to the optical transition frequency. Damping results from the dipole radiation of the oscillating electron according to Larmor's well-known

formula for the power radiated by an accelerated charge[R.Grimm et al., 2000]. The equation of the motion in one dimension can be written as

$$\ddot{x} + \Gamma_\omega \dot{x} + \omega_0^2 x = -e\frac{E(t)}{m_e} \tag{2.39}$$

For the driven oscillation of the electron, it is forthright to calculate the polarizability by integration of the equation of motion

$$\alpha = \frac{e^2}{m_e}\frac{1}{\omega_0^2 - \omega^2 - i\omega\Gamma_\omega} \tag{2.40}$$

Here, $\Gamma_\omega = e^2\omega^2/(6\pi\epsilon_0 m_e c^3)$ is the classical damping rate due to the radiative energy loss.

Introducing $\Gamma \equiv \Gamma_{\omega_0} = (\omega_0/\omega)^2\Gamma_\omega$, the polarizability will be

$$\alpha = 6\pi\epsilon_0 c^3 \frac{\Gamma/\omega_0^2}{\omega_0^2 - \omega^2 - i(\omega^3/\omega_0^2)\Gamma} \tag{2.41}$$

The atomic polarizability can be calculated by assuming the atom as a two-level quantum system interacting with the classical radiation field (semi-classical approach), and the saturation effects can be neglected.

$$\Gamma = \frac{\omega_0^3}{3\pi\epsilon_0\hbar c^3}|\langle e|\mu|g\rangle|^2, \tag{2.42}$$

where $|g\rangle$ and $|e\rangle$ show ground and excited states of the atom.

Finally, Eq. (2.35) can be written as

$$U_{dip}(\boldsymbol{r}) = -\frac{3\pi c^2}{2\omega_0^3}\left(\frac{\Gamma}{\omega_0 - \omega} + \frac{\Gamma}{\omega_0 + \omega}\right)^2 I(r), \tag{2.43}$$

and the scattering rate in the relevant case of large detunings and negligible saturation:

$$\Gamma_{sc}(\boldsymbol{r}) = \frac{3\pi c^2}{2\hbar\omega_0^3}\left(\frac{\omega}{\omega_0}\right)^3\left(\frac{\Gamma}{\omega_0 - \omega} + \frac{\Gamma}{\omega_0 + \omega}\right)^2 I(r). \tag{2.44}$$

In most experiments, the laser is tuned relatively close to the resonance at ω_0 such that the detuning $\Delta = \omega - \omega_0$ satisfies $|\Delta| \ll \omega_0$. In this case, the counter-rotating term can be neglected in the well-known rotating wave approximation. According

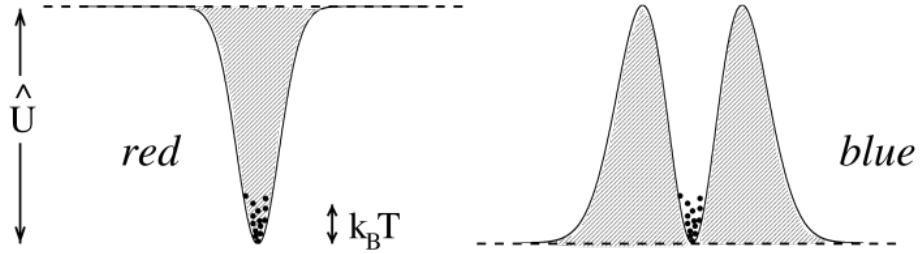

Figure 2.5: Portrait of dipole traps with red and blue detuning, respectively, shown by a simple Gaussian laser beam and a Laguerre-Gaussian LG01 "doughnut" mode beam, providing the same potential depth and curvature in the trap center [R.Grimm et al., 2000]

to rotating wave approximation, the known expressions for the dipole potential and the scattering rate simplify to

$$U_{dip}(\boldsymbol{r}) = \frac{3\pi c^2}{2\omega_0^3}\frac{\Gamma}{\Delta}I(\boldsymbol{r}), \tag{2.45}$$

and,

$$\Gamma_{sc}(\boldsymbol{r}) = \frac{3\pi c^2}{2\hbar\omega_0^3}\left(\frac{\Gamma}{\Delta}\right)^2 I(\boldsymbol{r}). \tag{2.46}$$

According to the sign of detuning, dipole traps can be divided into two main categories: red-detuned and blue-detuned.

On the one hand, below an atomic resonance, calling red detuning ($\Delta < 0$), where the dipole potential is negative, and the interaction thus attracts atoms into the light field. So, potential minima are found at positions with maximum intensity. On the other hand, the above resonance calling blue detuning, ($\Delta > 0$), where the dipole interaction repels atoms out of the field, and potential minima correspond to the intensity minima (Fig. 2.5).

2.4.3 The Gaussian Beam

The intensity of a Gaussian beam at the cylindrical coordinates (r, ϕ, z) is given by (2.6)

$$I(r,z) = \frac{I_0}{1+z/z_R} exp\left[\frac{-2r^2}{\omega_0^2(1+(z/z_R)^2)}\right] \tag{2.47}$$

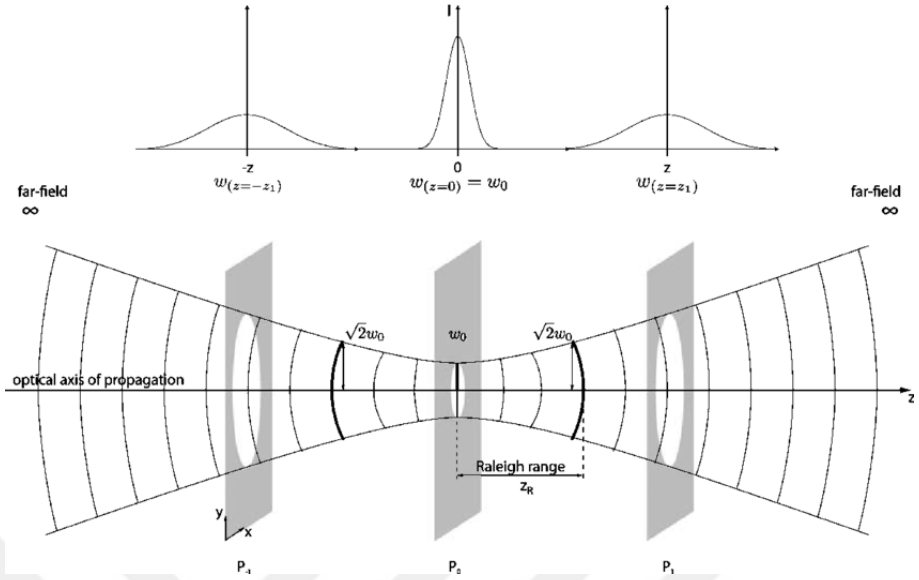

Figure 2.6: Free Gaussian beam propagation along the z-axis with ω_0 as beam waist, and Z_R as Rayleigh range [Jährling and Saghafi, 2011].

Here ω_0 indicates the beam waist at $z = 0$ where the intensity drops to $I(\omega_0, 0) = I_0 e^{-2}$. The Rayleigh range z_R can be define as $z_R = \pi\omega_0^2/\lambda$.

The beam waist at an arbitrary z is

$$\omega = \omega_0 \sqrt{1 + \left(\frac{\lambda(z - z_f)}{\pi\omega_0^2}\right)^2} \tag{2.48}$$

where z_f is the position of the focal point. Based on Equation (2.44), the intensity of a Gaussian beam consequently forms a potential as

$$U(r, z) = \frac{-U_0}{1 + (z/z_R)} exp\left[\frac{-2(r/\omega_0)^2}{1 + (z/z_R)^2}\right], \tag{2.49}$$

where based on RWA, U_0 is defined as

$$U_0 = \frac{3\pi c^2}{2\omega_0^3}\frac{\Gamma}{\Delta} I_0 \equiv \xi I_0. \tag{2.50}$$

2.4.4 Dipole Trap's Dynamics (Red Detuned)

We figure the atoms' dynamics in an optical dipole trap according to the Potential $U(r, z)$. Generally, we suppose the red detuned case using a single Gaussian beam. The small distances from the radial center can be approximated harmonically. Since

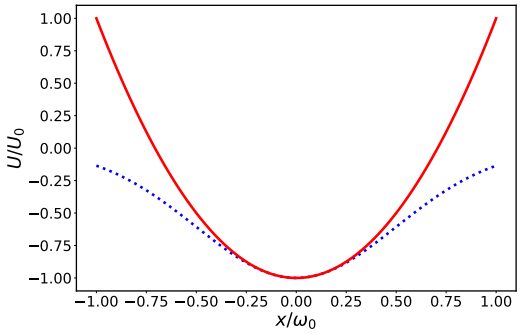

Figure 2.7: The original (blue dotted curve) and approximated (red solid curve) potential energies in an optical dipole trap are illustrated along the radial direction. They scale in terms of the maximal trap depth U_0 and the position in the beam waist w_0, showing that the second-order Taylor expansion is a good approximation for atoms occupying the bottom of the potential.

we are interested in the radial direction of the potential landscape, for the sake of simplicity, we can absorb the axial part in $U0$ and ω_0:

$$U_0 \equiv U_0(z) = \frac{U_0}{1 + z/z_R} \tag{2.51}$$
$$\omega_0 \equiv \omega(z) = \omega_0(1 + (z/z_R))$$

Therefore,

$$U(r, z) = -U_0 exp\left(-2(r/\omega_0)^2\right) \tag{2.52}$$

Expanding the Eq. (2.52) by Taylor polynomial at $r = 0$

$$U(r, z) = -U_0 \left[1 - 2(r/\omega_0)^2 + 4\frac{(r/\omega_0)^2}{2!} - ...\right] \tag{2.53}$$

where for $r \ll 1$

$$U(r, z) \approx -U_0 + 2U_0(r/\omega_0)^2 \tag{2.54}$$

This approximation (harmonic approximation) is valid for $r^4 \ll \omega_0$. The original (Eq. (2.52)) and approximated (Eq. (2.54)) potentials are shown in Fig. 2.7, indicating that the approximation works where $r/\omega_0 < 1$.

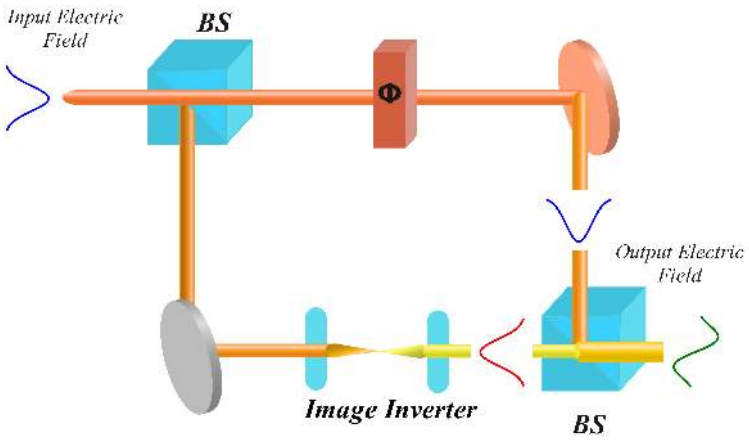

Figure 2.8: The image inversion interferometer is implemented as a Mach-Zehnder interferometer. It works with an appropriate delay in one arm and an image inverter in the other. The red and blue beams are perpendicular to each other and can not interfere [Tang et al., 2016].

The equations of motion of an atom trapped in a dipole trap with approximated potential represented in Eq. (2.54) is

$$m\ddot{r}(t) = -\frac{d}{dr}U(r(t)) = -\frac{4U_0}{\omega_0^2}r(t), \tag{2.55}$$

which gives the trap frequency as

$$\omega_r = \sqrt{\frac{4U_0}{m\omega_0^2}} \tag{2.56}$$

2.4.5 Designing a Blue-Detuned Trap

This section introduces a way to make a hollow (donut) shape beam based on interferometry introduced in Ref. [Tang et al., 2016] and then implement the obtained beam to create a blue-detuned trap. In 2016 an experiment introduced by Tang et al. using a method based on the self-interference technique, relying on image inversion interferometry, to determine the separation between two incoherent point sources [Tang et al., 2016]. The experiment is designed by the underlying tool of image inversion interferometry, that is, the interference of a beam with its inverted

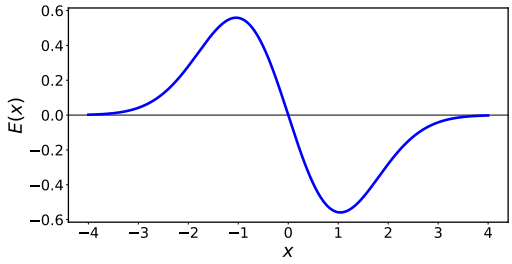

Figure 2.9: Dimensionless output electric field where x scaled by $\omega_0 = 1$ and $d = \omega_0/2$.

image. The system is expressed in Fig. 2.8, where the device is practically a Mach-Zehnder interferometer with an image inverter in one arm. In Fig. 2.8, the electric field for two-point emitters is labeled red and blue, which are perpendicular. The electric field of either emitter in the detector can be calculated as

$$\boldsymbol{E}_\alpha = \boldsymbol{E}(\boldsymbol{r} + \boldsymbol{d}) - \boldsymbol{E}(\boldsymbol{r} - \boldsymbol{d}), \tag{2.57}$$

where $\boldsymbol{d}$ is the separation of the source from the centroid in vector form, and α denotes two perpendicular beams' field introduced in experiment [Tang et al., 2016].

To simplify, we will continue in one dimension. The output intensity can be calculated by using Eq. (2.57)

$$\begin{aligned} I &= |E_0|^2 \left[exp\left(-\frac{(x+d)^2}{2\omega_0^2} \right) - exp\left(-\frac{(x-d)^2}{2\omega_0^2} \right) \right]^2 \\ &= I_1 + I_2 - 2\sqrt{I_1 I_2} \end{aligned} \tag{2.58}$$

The dimensionless output field is displayed in the Fig. 2.9 for $d = 0.5\ \omega_0$ which mention in Fig. 2.8 (e.g. red beam). Accordingly, the output intensity is shown in Fig. 2.10 (solid red curve), where the pick to pick (pp) is indicated by the distance between two pick points that are demonstrated by vertical black lines. The evolution of the pp based on d/ω_0 is shown in Fig. 2.11, which can be used as a measurement parameter of the trap's width, where calculating FWHM by pp. Our numerical results show that the minimum value of the pp tends to $2\omega_0$ for $d < 0.15\ \omega_0$. In the next section (Sec. 6.3), we study the introduced hollow beam in the focal area of a

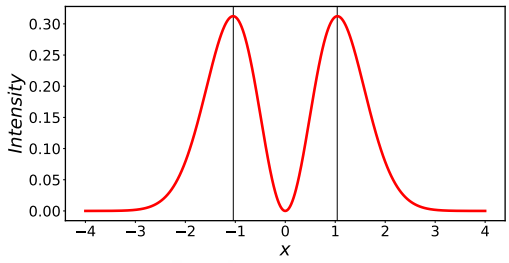

Figure 2.10: Dimensionless output intensity where x scaled by $\omega_0 = 1$ and $d = \omega_0/2$. Blue-dashed curves show the intensity of each beam separately, and the solid red curve indicates the interference output beam's intensity. The distance between two vertical black lines displays the FWHM.

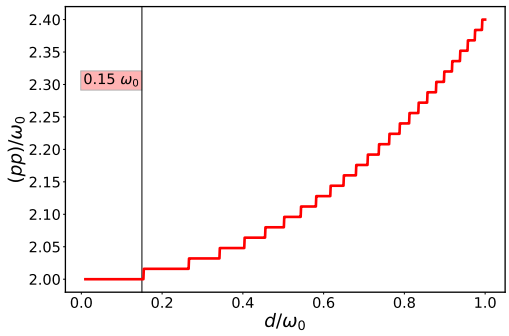

Figure 2.11: The scaled pp vs d/ω_0.

lens to impeliment it for a single-atom system in free space and see how the beam can trap the atom even under the diffraction limit. Now, we calculate the frequency of the trap for the presented hollow beam.

2.4.6 Blue-detuned Trap Equation of the Motion

According to Eq. (2.52) by using the hollow shape beam in Eq. (2.57), the trap frequency became

$$\begin{aligned} U_b(x,z) &= -U_0(z)|E_0|^2\left[\exp\left(-\frac{|x+d|^2}{2\omega^2}\right)-\exp\left(-\frac{|x-d|^2}{2\omega^2}\right)\right]^2, \\ &= -U_0(z)I_T, \end{aligned} \tag{2.59}$$

Using the Harmonic approximation, we expand it to a second order Taylor polynomial at $x = 0$

$$U_b(x,z) \approx 4|E_0|^2 U_0(z)(\frac{d}{\omega^2})^2 x^2. \tag{2.60}$$

The general solution of the equations of motion

$$m\ddot{x} = -\frac{d}{dx}[4U_0(z)(\frac{d}{\omega^2})^2 x^2] = 8U_0(z)(\frac{d}{\omega^2})^2 x, \tag{2.61}$$

where the frequency of the trap is

$$\omega_{blue}(x) = \sqrt{\frac{8U_0(z)d^2}{m\omega^4}} \tag{2.62}$$

Fig. 2.12 show we can approximate the potential based on Eq. (2.61) for small values of x.

2.5 Strongly Focused Light Beam

This section follows the method introduced in Ref. [van Enk and Kimble, 2001] to calculate the focusing field on a monochromatic Gaussian (paraxial) beam by an ideal strong lens. The optical field with a converging wavefront directly behind the lens must be propagated into the focal region to arrive at a field strength of the light interacting with the microscopic system. The field after the lens is expanded in a

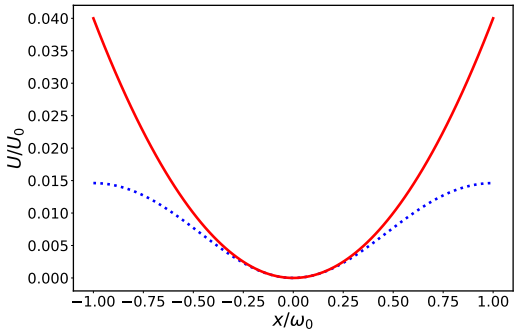

Figure 2.12: The original (blue dotted curve) and approximated (red solid curve) potential energies in an optical dipole trap are illustrated along x direction. They scale in terms of the maximal trap depth U_0 and the position in the beam waist w_0 where $E_0 = 1$, showing that Taylor expansion is a good approximation for small values of x.

complete set of modes which can be described as the exact solutions of Maxwell's equations [van Enk and Kimble, 2001].

$$\boldsymbol{E} = 2Re[\sum_{\nu} \alpha_\nu \boldsymbol{F}_\nu \exp\{(-i\omega t)\}], \tag{2.63}$$

with arbitrary complex amplitudes α_ν. The summation over ν is a notation for

$$\sum_{\nu} \equiv \int dk \int dk_z \sum_{s} \sum_{m}, \tag{2.64}$$

Here the field expanded based on a set of four eigenmodes, where k and k_z mention energy and momentum eigenmodes ($\hbar kc$ and $\hbar k_z$, respectively) in $\boldsymbol{z}$ direction. Angular momentum in $\boldsymbol{z}$ direction shown by $m\hbar$ and the helicity ($s\hbar k_z/k$) mentioned by s. We will consider monochromatic beams propagating in the positive z direction ($k_z > 0$) with a fixed value of $k = 2\pi/\lambda$. So, it projects the focusing field E_F on an orthogonal set of modes F_μ, $\mu = (k_t, s, m)$ with cylindrical symmetry where $k_t = \sqrt{k^2 - k_z^2}$ is the transverse part of the wave vector. Take k_t as a mode number instead of k_z, and we denote the set of mode numbers by $\mu \equiv (k_t, m, s)$, the notation can be written as

$$\sum_{\nu} \equiv \int dk_t \sum_{s} \sum_{m}. \tag{2.65}$$

The dimensionless mode functions $\boldsymbol{F}_\nu$ in cylindrical coordinates (ρ, z, ϕ) are defined by

$$\boldsymbol{F}_\nu = \frac{1}{4\pi}\frac{sk + k_z}{k}G(k, k_z, m-1)\boldsymbol{\epsilon}_+ + \frac{1}{4\pi}\frac{sk - k_z}{k}G(k, k_z, m+1)\boldsymbol{\epsilon}_- - i\frac{\sqrt{2}}{4\pi}\frac{k_t}{k}G(k, k_z, m)\boldsymbol{z}. \tag{2.66}$$

Here $\boldsymbol{\epsilon}_\pm = (\boldsymbol{x} \pm i\boldsymbol{y})/\sqrt{2}$ are two circular polarization vectors and $G(k, k_z, m)$ is defined by

$$G(k, k_z, m) = J_m(k_t\rho)\exp\{(ik_z z)\}\exp\{(im\phi)\} \tag{2.67}$$

where J_m is the mth order Bessel function.

2.5.1 Focusing with an ideal lens

An ideal lens transforms a beam with a plane wavefront with a radially dependent phase factor $\varphi(\rho)$ into one with a spherical wavefront that converges toward the focal point f (Fig. 2.13). The conversion of a plane into a spherical wavefront corresponds to a phase factor of $\varphi(\rho) = \exp\left[ik\sqrt{\rho^2 + f^2}\right]$ which in paraxial optics ($f \ll \rho$) can be approximated by equation [van Enk and Kimble, 2001]

$$\varphi = \exp\left(-ik\rho^2/2f\right) \tag{2.68}$$

In the plane of the lens ($z = 0$), the dimensionless incoming beam is given by

$$\boldsymbol{F}_{in} = \boldsymbol{F}_0(\rho, \phi), \tag{2.69}$$

and the output beam ($z > 0$) can be calculated by [van Enk and Kimble, 2001]

$$\boldsymbol{F}_{out}(\boldsymbol{r}) = \sum_\mu \kappa_\mu \boldsymbol{F}_\mu(\boldsymbol{r}) \tag{2.70}$$

where

$$\kappa_\mu = 2\pi k_t \int_0^{2\pi} d\phi \int_0^\infty d\rho\rho \exp\left(-i\frac{k\rho^2}{2f}\right)\boldsymbol{F}_0.\boldsymbol{F}_\mu^* \tag{2.71}$$

We suppose in the plane of the lens ($z = 0$), the incoming beam is given by

$$\boldsymbol{F}_0(\rho, \phi) = \exp\left(-\frac{\rho^2}{\omega_0}\right)\boldsymbol{\epsilon}_+, \tag{2.72}$$

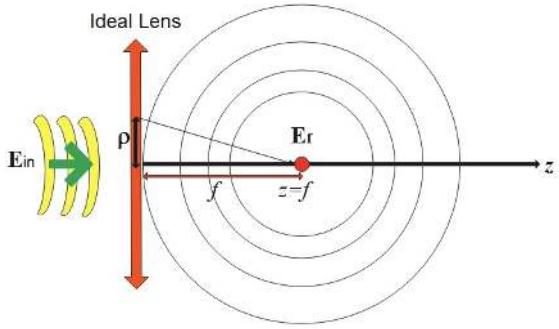

Figure 2.13: The electrical field $\boldsymbol{E}_{in}$ of a collimated beam with a Gaussian profile is converted into a focusing field $\boldsymbol{E}_f$ with a spherical wavefront by an ideal thin lens with a focal length f.

Using Eqs. (2.71) and (2.70)then κ_μ can be calculated by

$$\kappa_\mu = 2\pi k_t \int_0^{2\pi} d\phi \int_0^{\infty} d\rho\rho \left[\exp\left(-i\frac{k\rho^2}{2f}\right)\exp\left(-\frac{\rho^2}{\omega_0}\right)\right] \times \delta_{m1}\frac{1}{4\pi}\frac{sk+k_z}{k}J_{m-1}(k_t\rho)\exp(-ik_z z)\exp(-i(m-1)\phi), \tag{2.73}$$

where delta function δ_{m1} explains that the lens cannot absorb a cylindrically symmetric light's angular momentum, and since the incoming beam has one unit of "spin" angular momentum, index m should be 1 [van Enk and Kimble, 2001].

Using the integral

$$\int_0^{\infty} dr\alpha J_0(\beta r)\exp\left(-\alpha r^2\right) = \frac{1}{2\alpha}\exp\left(-\beta^2/4\alpha\right), \tag{2.74}$$

k_u can be simplified as

$$k_\mu = \pi\frac{k_t}{k}\frac{k_z+sk}{k}\zeta\exp\left(-\frac{k_t^2}{2k}\zeta\right) \tag{2.75}$$

where $\zeta \equiv \Omega_R - i\Omega_0$ by defining

$$\Omega_R = \frac{f^2 k\omega_0^2}{k\omega_0^2 + 2f^2},$$
$$\Omega_0 = \frac{f(k\omega_0^2)^2}{k\omega_0^2 + 2f^2}.$$

Now we can calculate the largest component of the output field (ϵ_+), which is given by

$$F_+ = \frac{\zeta}{2}\int_0^k dk_t \frac{k_t}{k}\frac{2k^2-k_t^2}{k^2}J_0(k_t r)\exp\left(-\frac{k_t^2}{2k}\zeta\right)\exp(ik_z z), \tag{2.76}$$

The dimensionless intensity $|F_0(\rho)|^2$, and $|F_+(\rho, z = 0)|^2$ as input and focal fields' intensity are shown in Fig. 2.15 where the system is scaled based on λ, and we consider $f = 100\ \lambda$, and $z_0 = 10^4$.

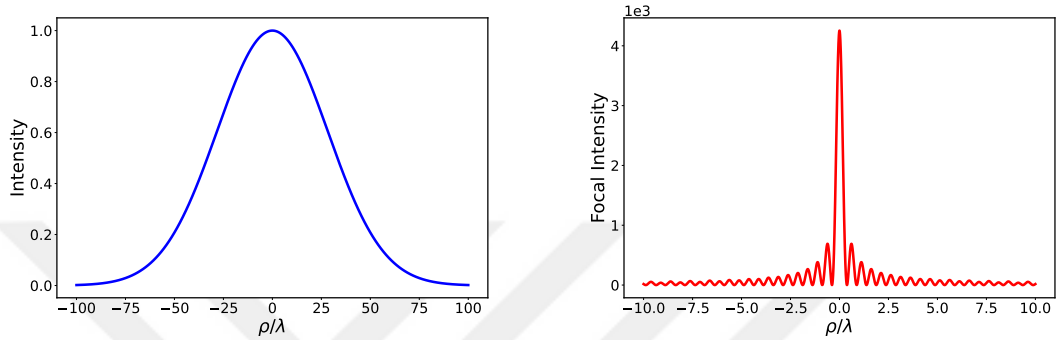

(a) (b)

Figure 2.14: (a) Input $|F_0|^2$ and (b) focal $|F_+|^2$ dimensionless intensity.

2.5.2 A Tight Blue-Detuned Trap

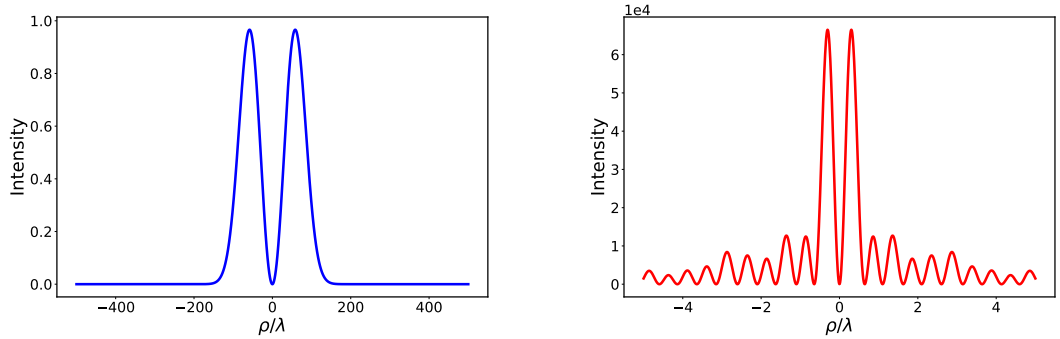

(a) (b)

Figure 2.15: (a) Input $|F_0|^2$ and (b) focal $|F_+|^2$ dimensionless intensity.

In this section, we consider tightly focused donut beams, i.e., beams of light produced by focusing an incoming higher-order LG beam. To make a tight blue detuned

trap, we implement the beam obtained from the method explained in Sec. 2.4.5. According to the presented method in Sec. 2.5.1, we can calculate the field in the focal point using Eq. (2.57).

The coefficient k_u can calculate by

$$\kappa_\mu = 2\pi k_t \int_0^{2\pi} d\phi \int_0^{\infty} d\rho\rho \exp\left(-i\frac{k\rho^2}{2f}\right)\left[\exp\left(-\frac{(\rho+d)^2}{\omega_0}\right) - \exp\left(-\frac{(\rho-d)^2}{\omega_0}\right)\right] \times \delta_{m2}\frac{1}{4\pi}\frac{sk+k_z}{k}J_{m-1}(k_t\rho)\exp(-ik_z z), \tag{2.77}$$

The δ function describes the conservation of the angular momentum. So, the field in the focal point can be obtained by

$$F_f = \sum_m \sum_{s=\pm 1} \int_{k_t} \frac{1}{4\pi}\frac{sk+k_z}{k}J_1(k_t\rho)\exp(ik_z z)\kappa_\mu \tag{2.78}$$

The dimensionless intensity for input field $|E_\alpha|^2$ (Eq. (2.57)) and output field $|E_f|^2$ calculated in Eq. (2.78) are shown in Fig. 2.15.

2.5.3 Generation of a sub-diffraction blue-detuned Trap

Cavities often achieve strong interaction between the light field and an atom. Recent experiments have operated a distinct configuration: a propagating light field is strongly focused using a system of lenses, and the atom is presumed to pose at the focal position. At any finite temperature, the atom position fluctuations affect the coupling. To acquire a more confined atom, which compels the stronger coupling, we propose a method to trap a single atom in a tight blue-detuned trap employing an intensely focused beam with a lens in free space. We show the atom is highly confined in the trap with a radius in the order of a nanometer.

We consider the same configuration introduced in Sec. 2.5.2 ([Tang et al., 2016]) while we replace the lens system with the detector to focus the output beam (Fig. 2.16). The complete setup of the system is shown in Fig. 2.16.

The outcoming beam from the interferometer is considered in the plane of the lens. It can be obtained by

$$E_T(r,z) = E_0(w_0/w(z))\left(\exp\left(-\frac{|r+d|^2}{w(z)^2}\right) - \exp\left(-\frac{|r-d|^2}{w(z)^2}\right)\right), \tag{2.79}$$

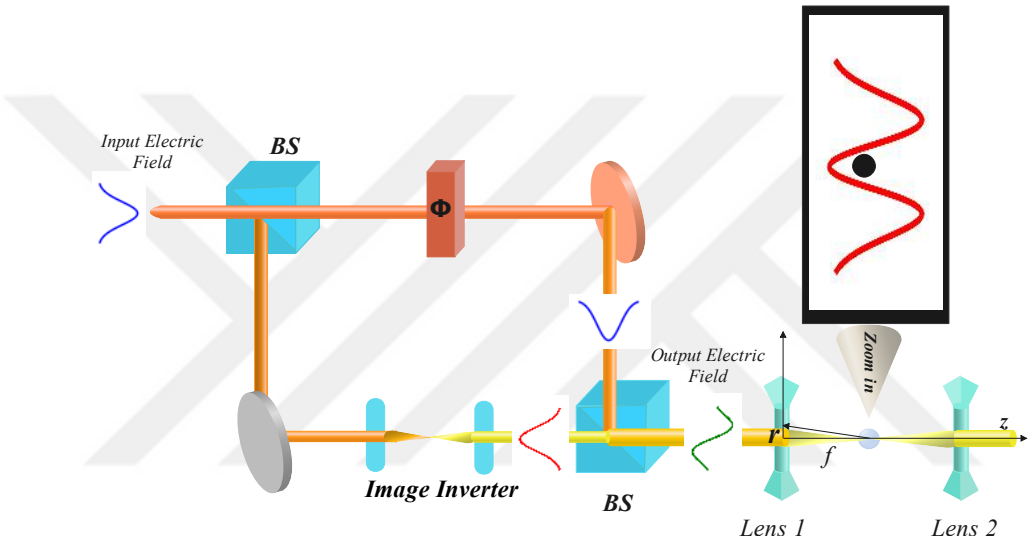

Figure 2.16: The schematic of an experimental setup to trap a single atom in a tight blue-detuned trap potential. The setup includes a balanced Mach-Zehnder interferometer and a lens system to focus the output beam in the focal point where a single atom is located. The interferometer contains an appropriate delay, Φ, in one arm and an image inverter in the other. We implement a self-interference technique to make a hollow shape beam before the first lens. After the first lens, the output beam propagates to the focal point. The inset figure shows the zoom-in of the trap potential in the focal point.

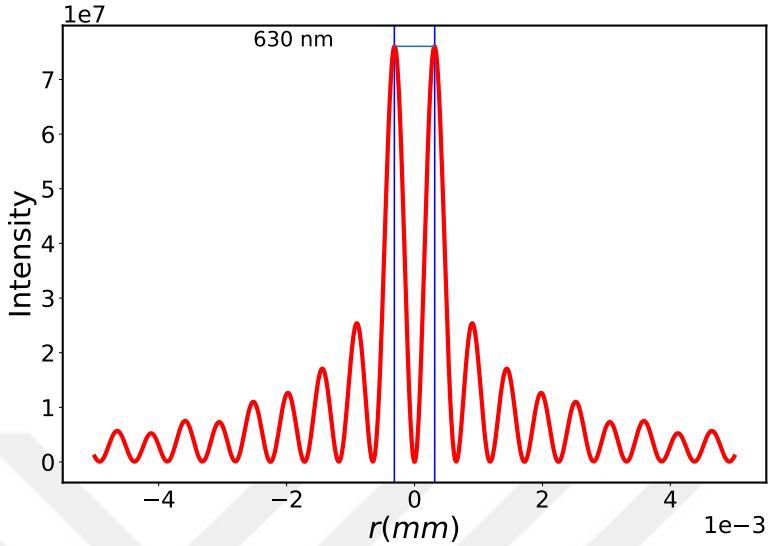

Figure 2.17: The dimensionless intensity distribution in focal point where $w_0 = d = 1.1$ mm, and $f = 4.5$ mm. The pick to pick in the focal point is calculated as $pp \approx 630$ nm.

where $w(z) = w_0\sqrt{1+(z/z_R)^2}$. The Rayleigh range is defined as $z_R = \pi w_0^2/\lambda$. The electric field on the focal plane at $z = f$ is calculated by

$$E_f(r, z = f) = \int_0^k dk_t \sum_{s=\pm} k_\mu \frac{1}{4\pi}\frac{sk + k_z}{k} j_1(k_t r)\exp(ik_z z), \tag{2.80}$$

where

$$k_\mu = 2\pi k_t \int_0^{2\pi} d\phi \int_0^\infty r dr E_T(r, z)\frac{1}{4\pi}\frac{sk + k_z}{k} j_1(k_t r)\exp(-ik_z z). \tag{2.81}$$

We consider a beam with width beam $\omega_0 = 1.1$ mm, and the intensity scaled based on $E_0 = 1$. The focal length is considered as $f = 4.5$ mm. The distribution of the beam in the focal point as a function of ρ scaled based on millimeter shown in Fig. 2.17. The diffraction limit for the ideal lens can be approximated by $d_{diff} = \lambda/2.8$ [Lipson et al., 1995]. For our proposed beam with $\lambda = 1064$ nm, so $d_{diff} \approx 380$ nm. On the other hand, the wavelength in the focal point can be approximated by $w_f \approx pp/2$, and $FWHM = \sqrt{2\ln 2}\, w_f \approx 371$ nm. So, $FWHM < d_{diff}$ presents the atom can be trapped in a trap with a sub-diffraction width.

We approximate the trap's radial frequency for presented tight blue-detuned trap in focal point using Eqs. (2.49), (2.4.3) and (2.62)

$$\omega_{blue}^{f} = \sqrt{\frac{8U_0(z)d_f^2}{mw_f^4}}, \tag{2.82}$$

Here, w_f, and d_f are obtained based on numerical simulation as

$$w_f \approx 315\ nm,$$
$$d_f \approx 265\ nm.$$

According Eqs. (2.51) and (2.50), $U(0)_z = U_0/(1+z/z_R)$ where $U_0 = (3\pi c^2\Gamma/2\omega_0^3\Delta)I_0 \equiv uI_0$.

For ^{52}Cr at the typical optical dipole trap wavelength $\lambda = 1064$ nm, we can calculate $u = 0.273 \times 10^{-36}\ Jm^2/W$. The intensity of the beam I_0 is

$$I_0 = \frac{2P}{\pi w_0} \tag{2.83}$$

Chapter 3

THE PRINCIPLES II (QUANTUM THERMODYNAMICS)

The combination of two independent theories, Thermodynamics and Quantum Mechanics, is named Quantum Thermodynamics, where new perspicuity appears whenever the two theories address the same phenomena. This section discusses thermodynamics laws in the quantum regime. We developed through the analysis of quantum thermodynamic cycles and quantum heat engines.

3.0.1 Thermodynamics laws

Zeroth law: If two thermodynamic systems, A and B, are each in thermal equilibrium with a third system, they are in thermal equilibrium. Accordingly, the temperature is defined as the intensive variable of a state equal to two systems if they are in thermal equilibrium.

A direct generalization of the classical zeroth law to the quantum realm is not available in quantum thermodynamics. Also, the temperature definition for a single quantum object, i.e., without an ensemble approach, is far from trivial [Aharonov and Vaidman, 1993, Aharonov et al., 1993, MM et al., 2020]. On the other hand, although the temperature is not observable, effective or virtual temperatures are found to be convenient to introduce [Skrzypczyk et al., 2015]. Even in quantum coherence, useful definitions of temperature, such as apparent temperature, can be proposed to interpret energy flows [Latune et al., 2019]. A single thermodynamical variable dual to energy cannot represent them unless they carry no quantum coherence in their energy basis. For example, one can use the excited and ground-level populations' ratio to assign a temperature to a two-level atom. However, if there is a quantum coherence between the two levels, it can also be used as an energy resource.

Accordingly, the atom requires at least two variables dual to energy to describe its thermodynamic value. In quantum thermodynamics, the temperature parameter per se is insufficient for tagging equivalence classes. Classical zeroth law can be violated in quantum coherence and correlations [Bera et al., 2017]. As canonical thermal Gibbs states, equilibrium states are allowed free states in resource theory [Chitambar and Gour, 2019, Lostaglio, 2019]. Accordingly, zeroth law defines the available free states for quantum thermodynamic operations. Temperature can be introduced as follows. Two thermal states involving their corresponding Hamiltonians are equivalent resources, provided that no work can be extracted from the joint state of their arbitrary number of copies [Brandão et al., 2015]. From the dynamical description of the thermalization of an open quantum system, subject to a heat bath at temperature T, zeroth law can be stated as the stationary state's presence with a unique canonical thermal (Gibbs) expression at T [Shishkov et al., 2018]. However, the existence of such a stationary Gibbs state is restrained as it relies on the system-bath interaction structure.

First law: In an isolated system, the internal energy is constant while it is changed by the balance of heat Q and work W contributions,

$$dU = đQ + đW, \tag{3.1}$$

where $đ$ is the inexact differential representing process-dependent infinitesimal changes. This law demonstrates Q and W as distinct but equivalent modes of energy transfer and signifies the conversion of one into the other. Q and W express a flow of energy that represent processes. The added heat is the amount of thermal energy that changes the system's temperature, and the work is the mechanical energy input that moves the system. Converting one into the other is the basis of all thermal machines. Furthermore, energy conservation points out that no possible engines generate more energy than they consume.

The contributions of coherent (work) and incoherent (heat) energy transfers are additive, and the first law can be taken as the definition of heat. On the other hand, a straightforward identification of work and heat definitions for a quantum system is unknown [Weimer et al., 2008]. The earliest proposal uses a mathematical

distribution of the exact differential in an infinitesimal change of the internal energy of a quantum system described by Hamiltonian H and in the state (density matrix) ρ.

$$dU = d(\mathrm{Tr}\{\rho H\}) = \mathrm{Tr}\{H d\rho\} + \mathrm{Tr}\{\rho dH\} \tag{3.2}$$

So, the first and second terms are taken as the definitions of heat and work, respectively,

$$\begin{aligned} đQ &:= \mathrm{Tr}(d\rho H), \\ đW &:= \mathrm{Tr}(\rho dH), \end{aligned} \tag{3.3}$$

The work and heat definitions, in terms of the energy eigenvalues E_j of H, and populations of the corresponding eigenstates p_j, become [74]

$$\begin{aligned} đQ &= \sum_j E_j dp_j, \\ đW &= \sum_j p_j dE_j. \end{aligned} \tag{3.4}$$

These definitions are intuitively appealing as they declare that processes associated with population modifications in energy levels transfer heat into the system. In contrast, those processes that change energy levels without varying their populations move energy into the system in the form of work. They construct the basis of directly generalizing classical thermodynamical processes and quantum heat engine cycles to their quantum counterparts [Quan et al., 2007a, Quan, 2009].

Second law: Without working on the system, the heat never transfers spontaneously from a cold to a hot reservoir, introducing irreversibility as a fundamental asymmetry in nature. A heat flow changes the state variable entropy S and is formally represented in the Clausius inequality,

$$\Delta S \leq \frac{\delta Q}{T}, \tag{3.5}$$

This positivity of entropy production limits the performance of heat engines, as it is impossible for any machine to convert heat into work entirely. The second law

of quantum thermodynamics imposes constraints on the quantum thermodynamical processes. One can conclude that classical thermodynamics can be envisioned as the limiting form of quantum thermodynamics [Tuncer and Mustecaplioglu, 2020].

Third law: Regarding the properties of closed systems, the entropy of a system approaches a constant value when its temperature approaches absolute zero. It defines an essential reference for the temperature scale and entropy since the absolute zero of temperature equals the zero point of entropy.

3.1 Thermodynamic Cycles

Heat engines are cyclic operating systems that convert a temperature difference between two thermal baths to some amount of mechanical work. A working medium in a thermodynamic cycle exchanges work and heat with the environment. The system performs as a heat engine if the work output overwhelms the work consumption, powered by net heat absorption. It acts as a heat pump if a net amount of work is consumed to generate a heat output more significant than the heat input. The internal energy of a system is expressed as a product of a conjugate pair of an intensive and an extensive state variable, like for classical macroscopic system pressure and volume (mechanical quantities) or temperature and entropy (thermal quantities) [Cal85, Atk10]. Using such pairs to represent a thermodynamic cycle directs to a straightforward formal definition, where the area of the cycle equals the net mechanical work produced. All thermodynamic properties can be derived from the relevant pairs of conjugate variables. Considering many combinations of thermodynamic processes, we can characterize various idealized cycles. For a clear description of the idealized processes, the cycles usually are represented such that one state variable is kept constant during this process. Real engines' thermodynamic cycles may deviate significantly from their idealized counterparts. In the following, we study the quantum versions of some thermodynamic processes.

3.1.1 Quantum isothermal process

In quantum isothermal processes, the working substance is kept in contact with a heat bath at a constant temperature. The system can perform positive work outside and absorb heat from the reservoir. In this process, considering a multi-level system as the working substance, the energy gaps and the occupation probabilities need to change simultaneously so that the system remains in an equilibrium state with the heat bath every instant. Specifically for a two-level system with the excited state $|e\rangle$, the ground state $|g\rangle$, and a single energy spacing ε. In the quasi-static quantum isothermal process, the ratio $r = P_e/P_g$ of the two occupation probabilities must meet the Boltzmann distribution $r = P_e/P_g = \exp[-\beta\varepsilon(t)]$ where $\beta = 1/k_B T$, and also the normalization condition $P_e + P_g = 1$ [Quan et al., 2007a].
According to ratio r, an effective temperature can be defined for a two-level system

$$T_{eff} = \frac{1}{k_B \beta_{eff}} = \frac{\varepsilon(t)}{k_B}(\ln[P_g/P_e])^{-1} \tag{3.6}$$

3.1.2 Quantum isochoric process

A quantum isochoric process has properties similar to that of classical isochoric processes. In a quantum isochoric process, the working substance is in contact with a heat bath, and no work is done in this process while heat is exchanged. In a quantum isochoric process, the occupation probabilities P_n and thus the entropy S change until the working substance finally reaches thermal equilibrium with the heat bath. For example, consider the working substance is chosen to be a particle confined in an infinite square well potential. In that case, no work is done during a quantum isochoric process when heat is absorbed or released. The occupation probabilities in every Eigen state satisfy the Boltzmann distribution at the end of the isochoric process.

3.1.3 Quantum adiabatic process

In a quantum adiabatic process the population distributions remain unchanged, $dP_n = 0$, while the process satisfies the generic quantum adiabatic condition. Ac-

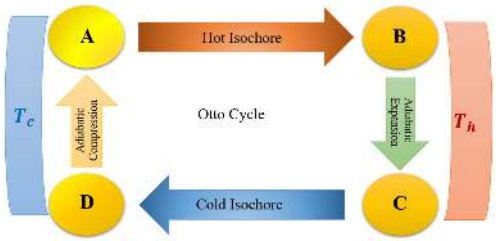

Figure 3.1: Schematic of an Otto Cycle.

cording to the first law, there is no heat exchange in a quantum adiabatic process. A classical adiabatic process, however, does not necessarily require the occupation probabilities to be kept invariant [Quan et al., 2007a].

3.2 Otto Engine

In this thesis, the Otto cycle will play a significant role. An Otto cycle consists of two isochoric and two isentropic processes (Fig. 3.1). The heating and cooling processes are much faster than the dynamics of the piston in an Otto cycle. In isochors, the heat is transferred between the system and the reservoirs at constant volume. The system's volume is changed at constant entropy while the system is isolated from the environment in the isentropic processes. The isoentropic processes are supposed to be adiabatic and reversible. During the expansion phase, the system moves a piston and thus performs work, while during the compression phase, works is consumed to compress the system by displacing the piston.

3.2.1 Otto Engine's Work and efficiency

In the quantum isochoric heating process from A to B (see Fig. 3.1), no work is done, but heat is absorbed as

$$Q_h = \sum_n E_n^h [P_n(\beta_h) - P_n(\beta_c)], \tag{3.7}$$

where E_n^h is the n-th eigen-energy of the system in the quantum isochoric heating process from A to B. Likewise, the heat released to the low-temperature entropy bath in the quantum isochoric cooling process from C to D

$$Q_c = \sum_n E_n^c [P_n(\beta_c) - P_n(\beta_h)], \tag{3.8}$$

Here E_n^c is the n-th eigen-energy of the system in the quantum isochoric cooling process. Therefore, using Eqs. (3.7) and (3.8), the net work w done during a QOE cycle can be calculated by

$$W = Q_h - Q_c = \sum_n \big(E_n^h - E_n^c\big)\big[\, P_n(\beta_h) - P_n(\beta_c)\big] \tag{3.9}$$

accordingly, the efficiency of the QOE is

$$\eta = \frac{W}{Q_h} = 1 - \frac{E_n^c}{E_n^h} \tag{3.10}$$

3.2.2 Two-Level system QOE

Let's consider a QOE based on a two-level system interacting with an external laser field. We assume the Hamiltonian of the two-level system based on Eq. (2.10). The eigenvalues of the Hamiltonian when the system scaled by $\Omega = 1$ and $\hbar = 1$ versus detuning Δ are plotted in Fig. 3.2. It shows that the difference between eigenvalues $|\delta E|$ is changing by modifying Δ. We show that $|\delta E|$ is increasing by changing Δ from 0 to 1 in Fig. 3.3.

We consider the system is in thermal equilibrium with a cold bath with reverse temperature β_c, where $\beta_c = 1/k_B T_c$, and Δ is zero initially. We put this two-level system in an Otto cycle, interacting with a laser, and calculate the work and efficiency. According to Fig. 3.3, we can execute the adiabatic processes by changing Δ. According to Sec. 3.2, the Otto engine cycle completes in four strokes based on the following steps:

Hot Isochore: The first stroke is the quantum isochoric heating process where heat exchanges between system and hot bath, but no work is done. During this

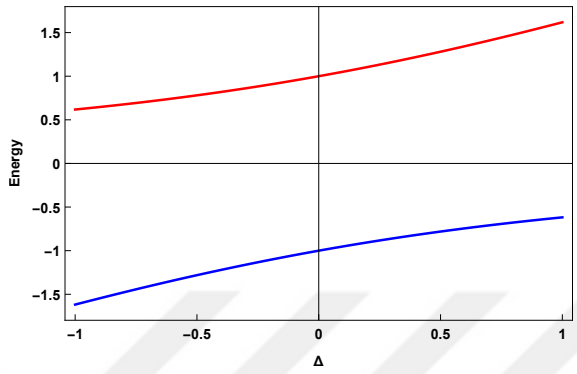

Figure 3.2: Evolution of the Two-level atom Eigen values vs detuning Δ.

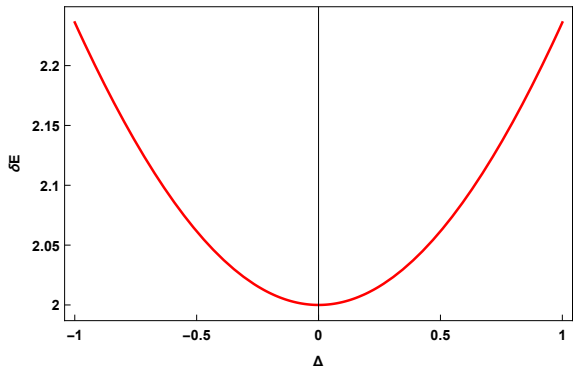

Figure 3.3: Evolution of δE vs detuning Δ.

process the system put into contact with the hot bath in inverse temperature β_h for a time τ_h. The exchanged heat Q_h is calculated by [Quan et al., 2007b]

$$Q_h = \sum_{n=1}^{2} E_n(\Delta = 0)(P_n(\beta_h) - P_n(\beta_c)) \tag{3.11}$$

Here, $E_n(A)$ is $n-th$ eigenenergy of system Hamiltonian H, and the population of $n-th$ eigenstate is changing from $P_n(\beta_c)$ to $P_n(\beta_h)$. Here $P_n(\beta) = \exp(-\beta E_n)/Z$, where $Z = \sum_n(\exp(-\beta E_n))$.

During this process, the Hamiltonian is kept constant. Here we can assume high temperatures and weak envelopes of a electromagnetic drive to claim approximate thermalization (See Eqs. (10) and (11) for the two-level case, e.g.in, the Ref. [Hildred1 et al., 1983]).

Adiabatic Expansion: The system Hamiltonian is changed from $H(\Delta = 0)$ to $H(\Delta)$ for a time τ_1 isolated from the environment. The adiabaticity can be acquired by modifying the system's energy over a time interval much shorter than the one needed to interact with a thermal bath [B. Leggio, 2016].

Cold Isochore: The system is put into contact with the cold bath at inverse temperature β_c for a time τ_c. The exchanged heat between system and cold bath is

$$Q_c = \sum_{n=1}^{2} E_n(\Delta)(P_n(\beta_c) - P_n(\beta_h)) \tag{3.12}$$

Adiabatic Compression: In the same methods that with the first adiabatic process, the cycle will close with the last adiabatic stroke while the system Hamiltonian shifts slowly from $H(\Delta)$ to $H(\Delta = 0)$ for a time $\tau_2 = \tau_1$.

Eventuallqy, the extracted work can be calculated by using Eqs. (3.11) and 3.12)

$$\begin{aligned} W &= Q_h + Q_c \\ &= \sum_{n=1}^{2} [E_n(\Delta = 0) - E_n(\Delta)](P_n(\beta_h) - P_n(\beta_c)). \end{aligned} \tag{3.13}$$

The efficiency of the engine can be calculated by $\eta = W/Q_h \times 100$, where the Otto cycle is working as a heat engine by satisfying the condition $Q_h > 0$, $Q_c < 0$

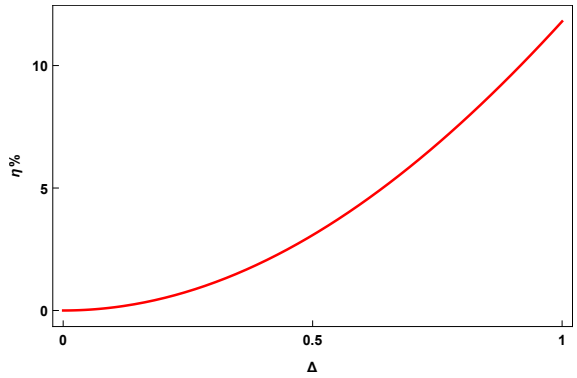

Figure 3.4: Evolution of efficiency $\eta(\%)$ vs detuning Δ.

and $W < 0$ from the system point of view. Fig. 3.4 shows the engine's efficiency corresponds to Δ, where the efficiency boosts by increasing Δ. We will repeat the same calculations for the three-level system with more details in Sec. 4.

Chapter 4

ENANTIOMER DETECTION VIA QUANTUM OTTO CYCLE

Enantiomers are chiral molecules that exist in right-handed and left-handed conformations. For the discrimination between left- and right-handed molecules, optical techniques of enantiomers detection are widely employed. However, identical spectra of enantiomers make enantiomer detection a very challenging task. Here, we investigate the possibility of exploiting thermodynamic processes for enantiomer detection. In particular, we employ a quantum Otto cycle, in which a chiral molecule described by a three-level system with cyclic optical transitions is considered a working medium. Each energy transition of the three-level system is coupled with an external laser drive. By changing the phase of these drives during the adiabatic stages of the Otto cycle, we find that left- and right-handed molecules work as a heat engine and heat pump, respectively. In addition, if the detuning of the laser drives is varied during adiabatic strokes of the cycle, both left- and right-handed molecules work as heat engines. However, the molecules can still be distinguished because the extracted work and efficiency are quantitatively very different in both cases. Accordingly, left and right-handed molecules can be distinguished by evaluating the work distribution in the Otto cycle.

4.1 Introduction

Quantum thermodynamics investigates the applicability of laws of thermodynamics and their possible generalizations in the realm of quantum mechanics [Gemmer et al., 2009, Kosloff, 2013, Vinjanampathy and Anders, 2016, Goold et al., 2016, Deffner and Campbell, 2019, Tuncer et al., 2020, Myers et al., 2022]. Quantum heat engines

(QHEs) serve as test beds for fundamental discussions and practical applications of quantum thermodynamics. In a broad context, QHE is a thermal machine whose operation cycle requires a quantum mechanical description. A typical example is the quantum Otto cycle, where the fast isentropic compression and expansion strokes of its classical counterpart are replaced by the slow quantum adiabatic parametric processes [Kosloff and Levy, 2014b, Kosloff and Rezek, 2017, Izadyari et al., 2022b, Altintas and Mustecaphoglu, 2015, Singh et al., 2021]. Different quantum working substances have been proposed to implement quantum Otto cycle [Scovil and Schulz-DuBois, 1959a, ScullyM et al., 2012, N. Brunner and Skrzypczyk, 2012, Hewgill et al., 2020, Naseem et al., 2020, Insinga et al., 2016], and experimental demonstrations have been reported for spin systems [Peterson et al., 2019, Bouton et al., 2021, Zhang et al., 2022]. These studies revealed that a quantum Otto cycle's work output and efficiency are determined by the energy spectrum of the quantum working system. Accordingly, we ask if a quantum Otto cycle can be used as a probe to discriminate systems with identical energy spectrums but with distinct spectral changes under the same parametric processes. A specific system with such a spectral character and for which this question is particularly significant is a chiral molecule.

Chiral molecules can have either left- or right-handed geometries that are not superimposable on their mirror images [Fox and Whitesell, 1974, Woolley, 1976]. They play significant role in fundamentals and applications in biology [Saito and Hyuga, 2013, Gal, 2012, Ariens, 1986], physics [Quack and Stohner, 2000], and pharmacy [Hutt and Tan, 1996]. The two mirror-image molecules are called enantiomers. Enantiomers exhibit identical physical and chemical properties in an achiral environment, while they can act remarkably differently when placed in a chiral environment [Ariens, 1986]. Chiral molecules may exist as a mixture of enantiomers in varying proportions. Therefore, enantioseparation is a critical and challenging task in chemistry and medicine [Chen et al., 2022, Ye et al., 2021, Kondru et al., 1998, Bielski and Tencer, 2005, Ye et al., 2019, McKendry et al., 1998, Bielski and Tencer, 2007].

Optical enantio-separation techniques are one of the most common methods for

enantiodetection based on the interference between the electric and the magnetic dipole transitions [Bielski and Tencer, 2007, Kondru et al., 1998]. Enantiomer-specific microwave spectroscopic methods, based on cyclic three-level systems, which can exist in chiral molecules [Král and Shapiro, 2001, Ye et al., 2018] and other artificial symmetry-broken systems [You and Nori, 2011], have been examined for the enantiodetection of chiral molecules [Shapiro and Brumer, 1991, Král et al., 1991, Král and Shapiro, 2001, Li and Shapiro, 2010, Jia and F.Wei, 2011, Patterson et al., 2013, Patterson and Doyle, 2013]. Three-level quantum systems with broken symmetry allows the coexistence of one- and two-photon transitions such that a cyclic population transfer can occur between different energy levels [Orlando et al., 1999, Hönigl-Decrinis et al., 2018, Guo et al., 2022, Král and Shapiro, 2001, Ye et al., 2018]. In this paper, we consider a chiral molecule, described by a three-level system with cyclic optical transitions, as our working substance subject to a quantum Otto cycle. By calculating the work and efficiency of the engine, we investigate if left- and right-handed enantiomers can have different energetics that can be probed by the engine behavior and the performance.

The rest of the paper is organized as follows. In Sec. 4.2, we describe and shortly review the Hamiltonian model to describe a cyclic three-level chiral molecule interacting with three linearly polarized optical fields, which was originally proposed in Ref. [Král and Shapiro, 2001]. In Sec. 4.3, we introduce the quantum Otto cycle operation where the detuning and the phases of the optical fields are used as the control parameters in the quantum adiabatic strokes. We calculate the quantum thermodynamic work and efficiency for different enantiomers and discuss how they can be distinguished in Sec. 4.4. We conclude in Sec. 5.5.

4.2 Model System

We consider a chiral molecule that is described by a three-level system with cyclic optical transitions driven by three classical optical fields [Král and Shapiro, 2001, Ye et al., 2018, Leibscher et al., 2019], and it is shown in Fig. 6.1. The Hamiltonian of this system in the rotating wave approximation is given by [Král and Shapiro,

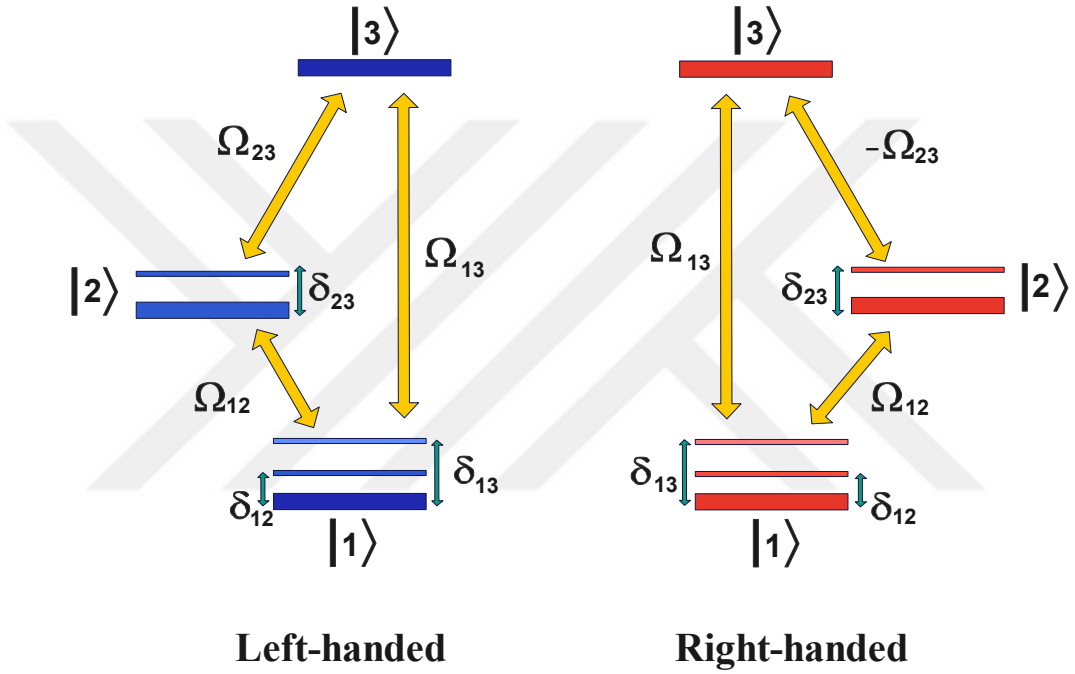

Figure 4.1: (Color online) A schematic illustration of a left-handed (a) and right-handed (b) chiral molecule which is described by a three-level system with cyclic optical transitions. The three-level system is coupled with three classical optical drives of Rabi frequencies Ω_{12}, Ω_{13}, and $\pm\Omega_{23}$, where $+\Omega_{23}$ $(-\Omega_{23})$ describes the left-handed (right-handed) molecule. The detunings of the external optical drives from energy transitions are indicated by δ_{ij}.

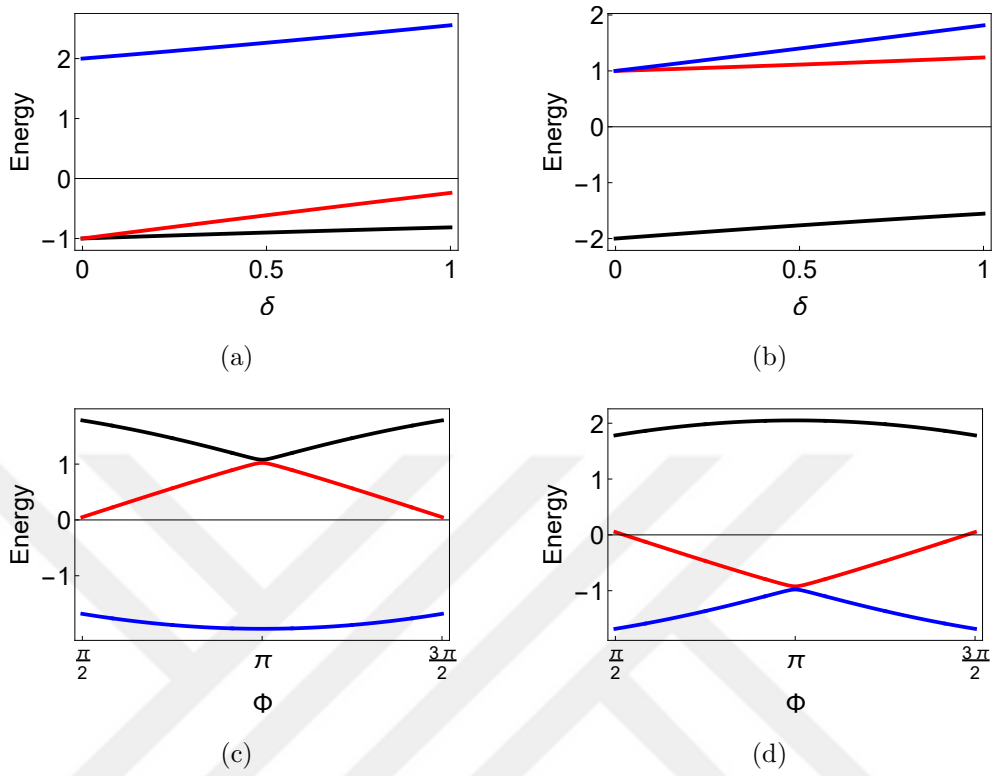

Figure 4.2: (Color online) Energy eigenvalues of the Hamiltonian $H_{\rm int}^{\pm}$ for constant overall phase $\Phi = 0$ (a, b), and constant detuning $\delta = 0.1/\tau_0$ (c, d). The panels (a, c) and (b, d) represent left- and right-handed enantiomers, respectively. The eigenenergies are scaled with the rotational energy $E_0 = \hbar^2 B$ with the rotational constant B, that is why eigenenergies are $\pm 1E_0$ and $\pm 2E_0$ for $\Phi = \delta = 0$. The eigenvalues are obtained for time-independent Hamiltonian ($\Delta = 0$) and considering the unit magnitude of the Rabi frequencies Ω_{ij}.

2001, Ye et al., 2018, Leibscher et al., 2019]

$$H = \sum_{j=1}^{3} \omega_j \left|j\right\rangle + \sum_{i>j=1}^{3} (\Omega_{ij}(t) e^{-i\omega_{ij}t} \left|i\right\rangle \left\langle j\right| + \text{H.c.}). \tag{4.1}$$

Here, the first term describes the energy of a three-level system with ω_j being the energy of the state $|j\rangle$. The second term describes the coupling of classical optical fields with the three-level atom; the frequency of the optical field is given by ω_{ij} which describes the coupling between $|i\rangle \leftrightarrow |j\rangle$ energy levels. $\Omega_{ij}(t) = \vec{\mu}_{ij}.\vec{E}_{ij}$ represents the Rabi frequency which depends on the field strength $\vec{E}_{ij}$ and associated transition dipole matrix element $\vec{\mu}_{ij}$ between the states $|i\rangle$ and $|j\rangle$. In the interaction picture,

the Hamiltonian of the chiral molecule is given by

$$H_{\text{int}}^{\pm} = \begin{pmatrix} \delta_{13} & \Omega_{12}e^{i(\Delta t+\Phi)} & \Omega_{13} \\ \Omega_{12}e^{-i(\Delta t+\Phi)} & \delta_{23} & \pm\Omega_{23} \\ \Omega_{13} & \pm\Omega_{23} & 0 \end{pmatrix} \tag{4.2}$$

Here, δ_{ij} is the detuning of the optical fields with energy levels $|i\rangle \leftrightarrow |j\rangle$, and $\Delta := \delta_{12} - \delta_{13} + \delta_{23}$. In addition, we define overall phase $\Phi := \Phi_{12} - \Phi_{13} + \Phi_{23}$, where $\Phi_{ij} = \phi_{ij} + \theta_{ij}$ contains the material phase θ_{ij} and the phases of the electric fields ϕ_{ij} [Leibscher et al., 2019]. We stress that the difference between the left- and right-handed molecules are expressed by the $\pm\Omega_{23}$, where the left-handed and right-handed molecules are given by positive and negative Rabi frequency Ω_{23}, respectively (see Fig. 6.1).

According to Eq. (4.2), the interaction Hamiltonian becomes time-independent for $\Delta = 0$ [Leibscher et al., 2019]. In the rest of the paper, we assume $\delta_{12} = \delta_{23} = \delta_{13}/2 \equiv \delta$ for which Δ becomes zero and the Hamiltonian becomes time-independent. This can be achieved by making a judicious choice on the selection of frequencies ω_{ij}. All system parameters can be scaled for convenience with arbitrary energy E_0. Henceforth, we assume that the system parameters are scaled with rotational energy $E_0 = \hbar^2 B$, defined by the angular momentum operators concerning the principle molecular axes [Leibscher et al., 2019], with the rotational constant B. Accordingly, time and frequencies are given in the units of $\tau_0 = \hbar/E_0$ and $1/\tau_0$.

Fig. 6.2 displays the eigenvalues of the Hamiltonian $H^{\pm}$ given in Eq. (4.2) as a function of the overall phase Φ and detuning δ. We implement the adiabatic strokes in the quantum Otto cycle by either varying the overall phase Φ or detuning δ; the adiabaticity condition requires no level crossing of the energy levels of the working medium. This is why we consider the system parameters in Fig. 6.2 and the rest of the paper such that there is no level crossing in the field-dressed eigenstates, which can occur for $\Phi = 0, \pi, 2\pi$, and $\delta = 0$ [Leibscher et al., 2019]. According to Fig. 6.2(c-d), the left- and right-handed enantiomer have identical energy spectrum for phases $\Phi = \pi/2$ and $\Phi = 3\pi/2$. We consider these two phase values as the starting and ending points of the adiabatic strokes in the cycle in Sec. 4.4.1. Although

the energy spectrum is identical at the start and end of the adiabatic strokes, we will show that the Otto cycle discriminates the left- and right-handed enantiomer in the output work. Furthermore, we investigate the Otto cycle by keeping the overall phase constant and adjusting the detuning in adiabatic processes as a more practical assumption in Sec. 4.4.2. The next section illustrates that the different energy characteristics of enantiomers lead to different thermodynamic properties when subjected to an Otto cycle.

4.3 Chiral Molecule Otto cycle

A quantum Otto cycle (QOC) consists of two quantum isochoric and two adiabatic processes [Quan et al., 2006]. We consider a chiral three-level system with cyclic optical transitions as a working medium of our quantum Otto cycle. A schematic illustration of the QOC is shown in Fig. 6.3 where the system is in contact with a hot and cold bath in two isochoric processes indicated by $A \to B$ and $C \to D$, respectively. During the adiabatic strokes of the cycle, the Hamiltonian changes slowly, and the system is not allowed to exchange heat with the environment. At the start of the cycle, we assume that the working medium is in thermal equilibrium with the cold thermal bath of inverse temperature β_c. The four strokes of the quantum Otto cycle are described as follows:

Hot Isochore ($A \to B$): The first stroke is the quantum isochoric heating process in which the working medium is coupled to a hot bath of inverse temperature β_h. During this stroke, Q_h heat is injected into the system, but no work is done. At the end of this stroke, we assume that the working medium comes to equilibrium with the hot thermal bath, and each energy level has an occupation probability of $P_j(\beta_h)$. The exchanged heat Q_h with the hot thermal bath is calculated by [Quan et al., 2007b]

$$Q_h = \sum_{n=1}^{3} E_n(A)(P_n(\beta_h) - P_n(\beta_c)) \tag{4.3}$$

Here, $E_n(A)$ is n-th eigenenergy of system Hamiltonian H_{int} for overall phase Φ_1, and the population of the associated eigenstate is changed from $P_n(\beta_c)$ to $P_n(\beta_h)$.

During this stage, the Hamiltonian $H_{\rm int}^{\pm}$ is kept constant; accordingly, no work is done.

In general, the system may not reach a thermal state in the presence of external laser drives. Here, we assume the cyclic three-level system approximately thermalizes with the bath at the end of the isochoric stages. This approximation is reasonable for weak envelopes of the three electromagnetic drives and high temperatures of the thermal baths. Thermalization of a two-level atom in the presence of a laser drive has been discussed previously, e.g., see Eqs. (10) and (11) of Ref. [Hildred1 et al., 1983].

To check the validity of the thermalization assumption, we numerically simulate the system's dynamics for the isochoric stages of the cycle. In particular, the dynamics of the reduced state ρ of the three-level system during the isochoric stages is given by the master equation [Breuer and Petruccione, 2007, Scully and Zubairy, 1997, Fink et al., 2010]

$$\frac{d\rho}{dt} = -i[\hat{H}, \rho] + \sum_{i \neq j} \kappa_\alpha (\bar{n}_\alpha + 1) D[\hat{\sigma}_{ij}] + \kappa_\alpha \bar{n}_\alpha D[\hat{\sigma}_{ij}^\dagger]. \tag{4.4}$$

Here, $D[\hat{u}] = (1/2)(2\hat{u}\rho\hat{u}^\dagger - \hat{u}^\dagger\rho\hat{u} - \rho\hat{u}^\dagger\hat{u})$ refers to the Lindblad dissipator superoperators with $\hat{u} = \hat{\sigma}_{ij}$ $(i = 1, 2, 3)$. $\alpha = h, c$ denotes the hot or cold bath, respectively. In addition, κ_α is the system-bath coupling strength and $\bar{n}_\alpha$ is the average excitation of the bath. We obtained the reduced state of the three-level system ρ by numerically solving the master equation using Python programming language and an open source quantum optics package QuTiP [Johansson et al., 2013].

We note that a system coupled to a thermal bath at inverse temperature β_h takes $t \to \infty$ time to reach the corresponding exact Gibbs (thermal) state [Breuer and Petruccione, 2007] with density matrix

$$\rho_{\rm th} = \frac{e^{-\beta_j H_{\rm s}}}{{\rm Tr}[e^{-\beta_j H_{\rm s}}]} \tag{4.5}$$

In order to realize a practical heat engine, we assume the system reaches the target thermal state as long as its state is at a small distance from the target state. We quantify this error by

$$\varepsilon = 1 - \mathcal{F}(\rho(t), \rho_{\rm th}), \tag{4.6}$$

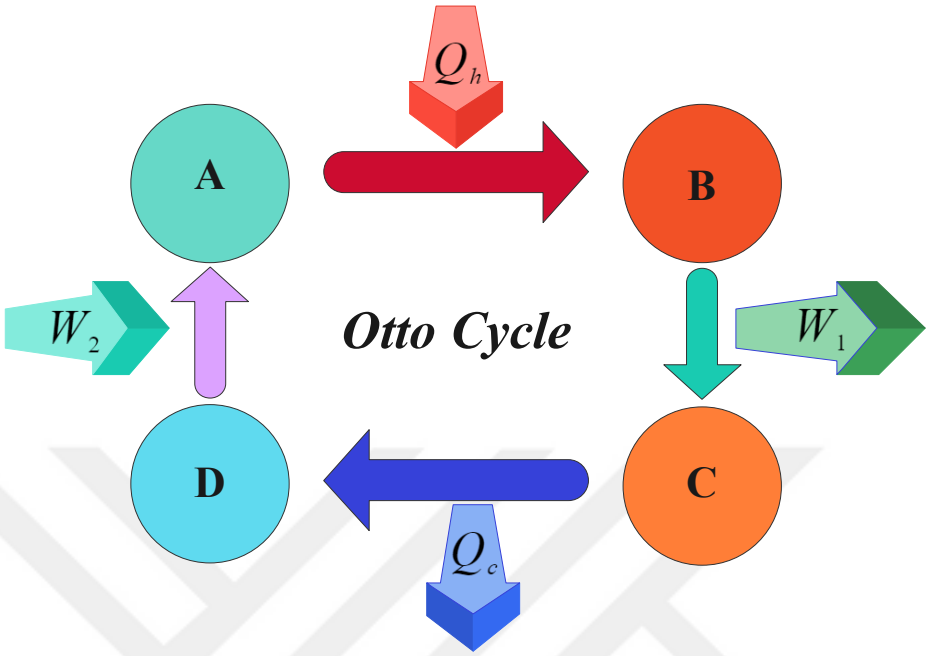

Figure 4.3: (Color online) A schematic description of a quantum Otto cycle consisting of two isochore strokes ($A \to B$ and $C \to D$), and two adiabatic strokes ($B \to C$ and $D \to A$). During the hot isochore $A \to B$, Q_h heat is injected into the working medium from the hot bath of temperature T_h, and in the cold isochore $C \to D$, the working medium rejects Q_c into the cold bath of temperature T_c. During the adiabatic expansion $B \to C$ and compression $D \to A$, work is extracted and invested on the working medium, respectively.

here $\mathcal{F} = \mathrm{Tr}[\sqrt{\sqrt{\rho}\rho_{\mathrm{th}}\sqrt{\rho}}]$ is the fidelity between the state of the three-level system and its corresponding thermal state at β_j during the thermalization strokes. In our numerical results, the calculated tolerance is obtained as $\varepsilon < 10^{-4}$. Fig. 4.4 shows the tolerance ε as a function of scaled time; it is immediately evident that our assumption of thermalization is reasonable in the considered system parameters regime. It indicates that the system in each thermalization process reaches its thermal state with high fidelity ($\mathcal{F} \approx 1$).

Adiabatic Expansion ($B \to C$): During this stage, the system is decoupled from the hot bath, and the system Hamiltonian is changed from $H(A)$ to $H(B)$. We discuss two strategies to implement the adiabatic strokes: First, varying Φ

from Φ_1 to Φ_2 by keeping detuning constant such that $\delta > 0$. In second case, changing the detuning δ from δ_1 to δ_2 for constant phase Φ. Work is extracted from the system during this stage of the cycle. We assume this process is slow enough that the occupation probabilities of the energy levels are unchanged to satisfy the adiabaticity condition. The adiabaticity can be ensured by modifying the system's energy over a time interval much shorter than the one needed to interact with a thermal bath [B. Leggio, 2016].

Cold Isochore ($C \rightarrow D$): During this stage, the system is subject to either constant phase Φ and it is put into contact with the cold bath of inverse temperature β_c for a time τ_c. The exchanged heat between the system and the cold bath is given by

$$Q_c = \sum_{n=1}^{3} E_n(B)(P_n(\beta_c) - P_n(\beta_h)). \tag{4.7}$$

At point D, the system reaches to a thermal state defined by inverse temperature β_c, and no work is done during this stage.

Adiabatic Compression ($D \rightarrow A$): Similar to adiabatic expansion, the system is isolated from the environment during this stage. The eigenenergies are changed by varying either phase Φ or detuning δ; the occupation probabilities remain the same during this stroke. The cycle closes with the adiabatic compression while the system Hamiltonian shifts slowly from $H(B)$ to $H(A)$ for a time τ_4. The net produced work during a cycle can be calculated by using Eqs. (4.3 and 4.7)

$$\begin{aligned} W_0 &= Q_h + Q_c \\ &= \sum_{n=1}^{3} [E_n(A) - E_n(B)](P_n(\beta_h) - P_n(\beta_c)). \end{aligned} \tag{4.8}$$

The efficiency of a heat engine is defined as $\eta = W_0/Q_h$. Here we adopt the convention that the work done on (by) the system is positive, and heat flow out of (into) the system is negative.

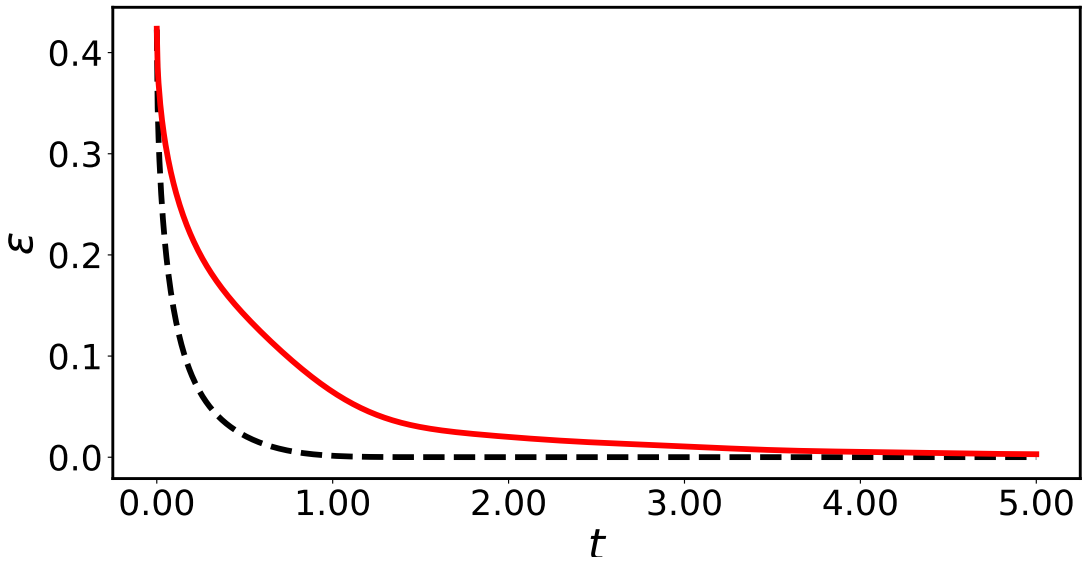

Figure 4.4: (Color online) The error ε (Eq. (4.6)) in the assumption of thermalization calculated during the isochoric stages of the cycle as a function of the time (scaled by τ_0). Solid and dashed lines represent the thermalization of the system during the cold and hot isochore stages of the cycle. In the long time limit, the state of the three-level system $\rho(t)$ reaches the target thermal state ρ_{th} during the isochoric stages.

4.4 Results

We look for the signatures in the work output of the Otto cycle to distinguish left- and right-handed enantiomers. The system's Hamiltonian (Eq.(4.2)) is a function of the overall phase Φ and detuning δ. As a result, the adiabatic stages of the cycle can be implemented either by varying the phase or detuning and keeping the other constant during the stroke. In this section, we examine both strategies for implementing the Otto cycle; and evaluate the output work to distinguish enantiomers. First, we investigate the Otto cycle in constant detuning δ regime while the overall phase employs as the control parameter in Sec. 4.4.1, and then in Sec. 4.4.2 examine the Otto cycle when δ is the control parameter, and overall phase kept constant.

4.4.1 Control parameter Φ

We adhere to the sign conventions of absorbed (rejected) heat is positive (negative), and work extracted (consumed) is negative. Accordingly, the thermal machine's operations can be categorized into four distinct regimes [Solfanelli et al., 2020]

$$
\begin{aligned}
&Engine: && W \leq 0, Q_h \geq 0, Q_c \leq 0,\\
&Refrigerator: && W \geq 0, Q_h \leq 0, Q_c \geq 0,\\
&Heater: && W \geq 0, Q_h \leq 0, Q_c \leq 0,\\
&HeatPump: && W \geq 0, Q_h \geq 0, Q_c \leq 0.
\end{aligned}
$$

We consider the set of system parameters for which there is no level crossing between the energy levels during the Otto cycle (see Fig. 6.2). Accordingly, we consider the phase $\Phi_1 = \pi/2$ at the start of the adiabatic expansion and change it to $\Phi_2 = 3\pi/2$ at the end of this stage. Similarly, the phase is changed from Φ_2 to Φ_1 in the adiabatic compression stage. During the adiabatic stages detuning $\delta = 0.1/\tau_0$ is kept constant. The heat exchanged with the thermal baths and extracted work for left- and right-handed systems are shown in Fig. 4.5. For both left- and right-handed enantiomers, the heat injected Q_h from the hot bath into the system is positive, and heat rejected Q_c into the cold bath is negative. However, the work distribution reveals that work is extracted from the left-handed system ($W < 0$) but in the right-handed system,

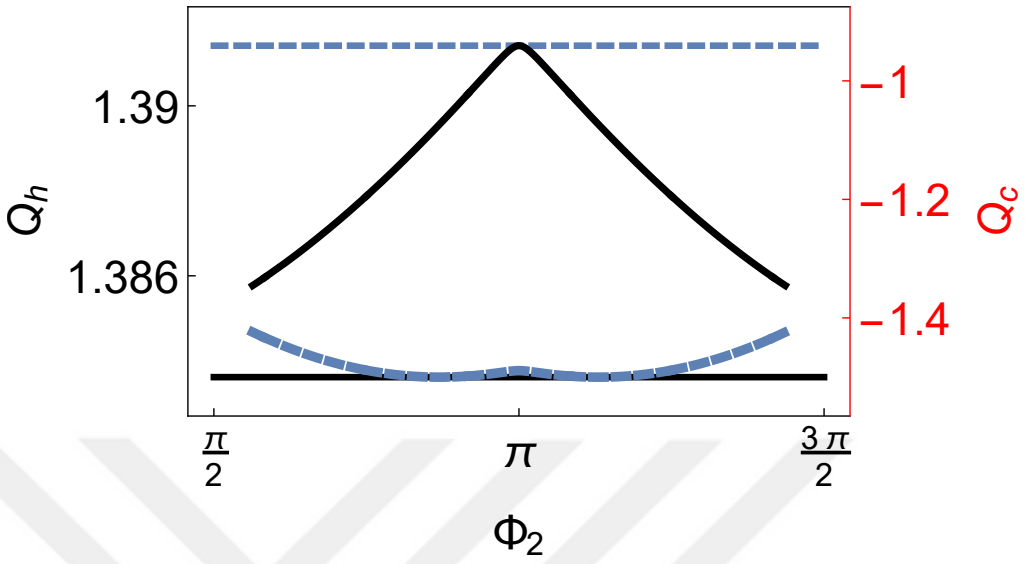

(a)

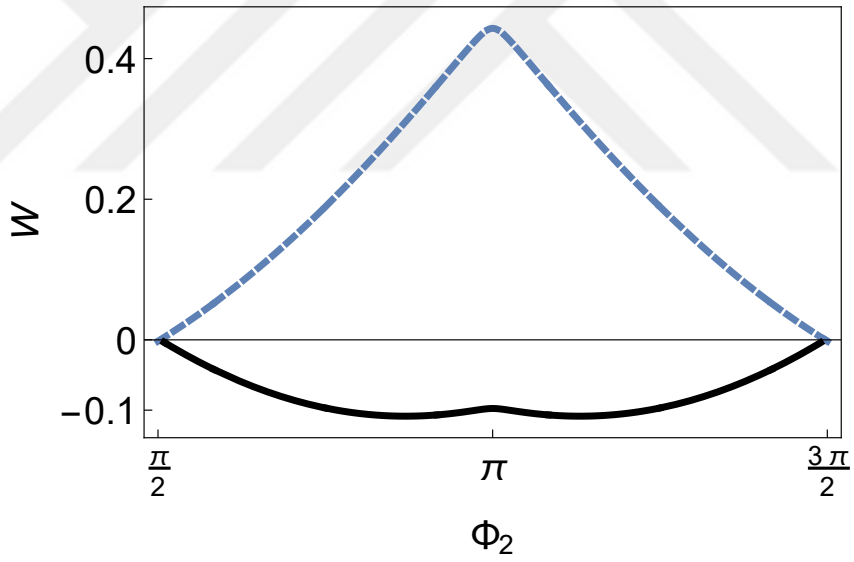

(b)

Figure 4.5: (Color online) (a) Heat exchange Q_h with the hot bath and Q_c (scaled by E_0) with the cold bath as a function of the overall phase Φ of the optical drives with contant $\delta = 0.1/\tau_0$. The solid and dashed lines are for the right- and left-handed enantiomers. In addition, upper and lower horizontal lines represent heat Q_h injected into the system, and heat rejected Q_c into the cold bath is denoted by curved lines. (b) Work output W as a function of the phase Φ of the optical drives in the quantum Otto cycle operating between the hot and cold baths of inverse temperatures $\beta_h = 0.01$, and $\beta_c = 1$, respectively. The solid and dashed lines are for the left- and right-handed enantiomers, respectively.

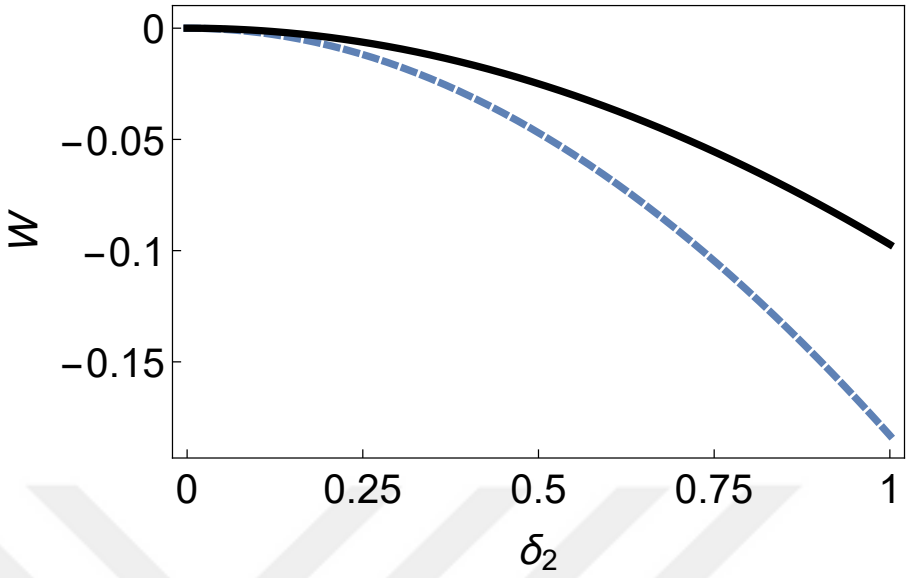

Figure 4.6: (Color online) Work output W as a function of the detuning δ_2 (scaled by τ_0) supposing the optical drive fixed initially at resonance, $\delta_1 = 0$ and overall phase kept constant at $\Phi = 0$. The quantum Otto cycle operates between the hot and cold baths of inverse temperatures $\beta_h = 0.01$, and $\beta_c = 1$, respectively. The solid and dashed lines are for the left- and right-handed enantiomers.

the work is done on the system ($W > 0$). Accordingly, the left- and right-handed enantiomers operate as a heat engine and heat pump, respectively. Therefore, the thermodynamics response of the enantiomers are not the same, which can be used as a probe to distinguish these enantiomers.

4.4.2 Control parameter δ

It can be of practical importance to check the thermal behaviors of chiral three-level systems in the Otto cycle using δ as the control parameter with a constant phase Φ. The work output, in this case, is shown in Fig. 4.6, which shows that both the left- and right-handed enantiomers operate as heat engines. However, the extracted work in both cases can be significantly different. The extracted work differs between left- and right-handed systems based on the constant Φ selection. For instance, if we keep overall phase $\Phi = \pi/2$ during the Otto cycle, the obtained extracted work is the same for both enantiomers, but it is significantly different for

$\Phi = \pi$ ($W_{left} = -0.18\ E_0$ and $W_{right} = -0.097\ E_0$).

The efficiency of the Otto engine is given by

$$\eta(\%) = \frac{W}{Q_h} \times 100. \tag{4.9}$$

To study the efficiency, we consider the control parameter δ modifying from $\delta_1 = 0$ to $\delta_2 = 1/\tau_0$. We define the efficiency as a function of the overall phase Φ, which is constant during the cycle. The engine's efficiency corresponds to Φ is plotted in Fig. 4.7 where the solid black and dashed blue curves denote the left- and right-handed system's efficiency, respectively. According to Fig. 4.7, the magnitude of maximum efficiency for both cases is the same, $\eta \approx 20\%$. So, in a particular condition, both of them are equally efficient. However, their efficiency is distinguishable because of their dependency on the overall phase. For example, the left-handed Otto engine's maximum efficiency is obtained at $\Phi \approx \pi/5$, and $6\pi/5$ while it is maximum at $\Phi \approx \pi \pm 0.7$ for the right-handed engine. Also, $\eta_{left} = \eta_{right}$ at $\Phi = \pi/2$, and $3\pi/2$ which comes from their identical energy spectrum of the enantiomers in these points (Fig. 6.2). Therefore, regarding an appropriate constant phase, efficiency can be a powerful measurement to discriminate between the left- and right-handed enantiomers. Also, it can be considered as a hint as to why nature prefers one of the enantiomers.

4.5 Conclusion

We have investigated the possibility of exploiting thermodynamic processes for enantiomers detection. In particular, we considered a chiral molecule described by a cyclic three-level system coupled to three external classical optical fields. We found that depending on the phase and detuning of the optical fields, the left- and right-handed cyclic three-level system exhibited different thermal functions when subjected to an Otto cycle. Specifically, suppose the adiabatic strokes in the cycle are implemented by changing the overall phase of three optical drives. In that case, the left- and right-handed enantiomer operate as a quantum heat engine and heat pump. The

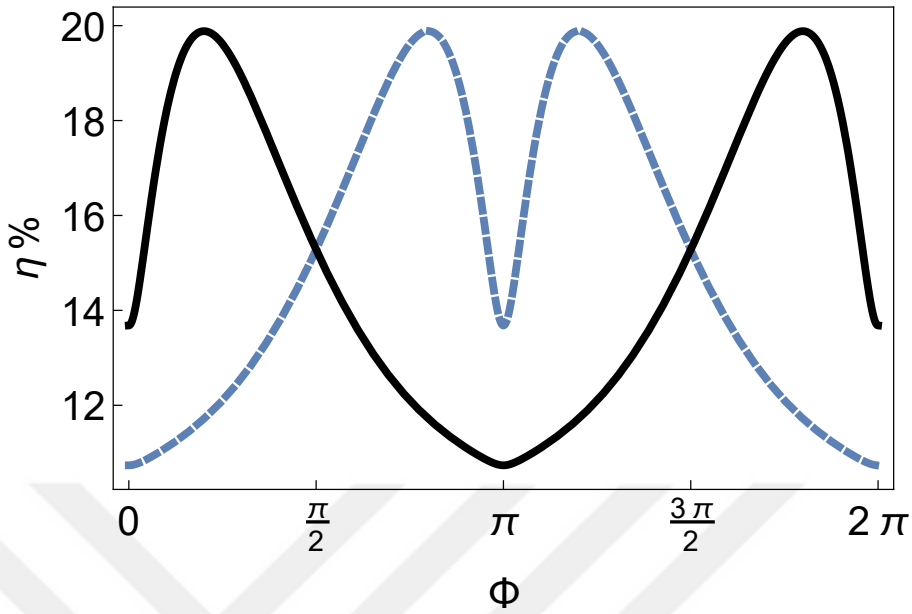

Figure 4.7: (Color online) The engine's efficiency $\eta(\%)$ as a function of Φ, while detuning as a control parameter modifies from $\delta = 0$ to $\delta = 1/\tau_0$, in the quantum Otto cycle operating between the hot and cold baths of inverse temperatures $\beta_h = 0.01/\tau_0$, and $\beta_c = 1/\tau_0$, respectively. The solid and dashed lines are for the left- and right-handed Otto engines.

extracted work is maximum for the case of the upper two nearly degenerate energy levels. Suppose the adiabatic strokes in the cycle are implemented by changing the detuning δ and keeping phase Φ constant during the cycle, which is more practical from the experimental point of view. In that case, both the left- and right-handed enantiomers operate as heat engines. However, the enantiomers still can be distinguished by the output work distribution and their efficiency, as quantitatively. In addition to the practical distinction of enantiomers, our results fundamentally suggest that different enantiomers may be associated with different thermodynamic (energetic) functions in chemical or biological processes, such as work harvesting or heat pumping. Besides, even if they are capable of performing the same energetic function, their efficiencies may differ so that one enantiomer may be more favorable than the other. One of the crucial steps in implementing the Otto cycle with a three-level system with cyclic optical transitions is the thermalization of the system. In general, in the presence of external laser drives, a system coupled to a thermal

bath may not reach a thermal state. However, by numerically solving the master equation for the isochoric stages of the cycle, we showed that a thermal state could approximately give the system's state.

Enantiomer detection is a formidable task, even for the case of two enantiomers, because of their identical energy spectra [Quack, 1986, Fabri et al., 2015, Leibscher et al., 2019]. Our analysis revealed that thermodynamic processes could be exploited for enantiomer detection. Our method of enantiomer detection via work distribution can be an alternative to more widely employed schemes for discrimination between the enantiomers [Kondru et al., 1998, Bielski and Tencer, 2007].

Chapter 5

SINGLE ATOM HEAT ENGINE IN A TAPERED TRAP

5.1 Introduction

Quantum heat engines (QHEs) are machines harnessing thermal energy using quantum working substances [Geusic et al., 1967, Kosloff and Levy, 2014a]. While the three-level maser, a quantum device that amplifies microwave radiation, was recognized as a QHE several decades ago [Scovil and Schulz-DuBois, 1959b], systematic studies of QHE have attracted much attention quite recently [Dawkins et al., 2019, Kieu, 2004, Quan et al., 2005, Quan et al., 2007c, Scully et al., 2011, Altintas et al., 2014, Abah et al., 2012, Bergenfeldt et al., 2014, Roßnagel et al., 2014, Altintas et al., 2015, Zhang and Zhang, 2017, Naseem and Mustecaphoglu, 2019, Barontini and Paternostro, 2019, Wang et al., 2012, Steeneken et al., 2011, Kaur et al., 2021, Ghosh et al., 2019, Brantut et al., 2013, Blickle and Bechinger, 2012, Hugel et al., 2002, Martinez et al., 2016, Zhang, 2020, Naseri-Karimvand et al., 2022, Metcalf and van der Straten, 1999, Levy et al., 2020, Levy et al., 2016, Lindenfels et al., 2019, Sheng et al., 2021, Xu et al., 2021, Gelbwaser-Klimovsky and Kurizki, 2015, Huang et al., 2018, He et al., 2012]. A pioneering experiment was the demonstration of a piston-type (Otto) engine using a single trapped ion [Roßnagel et al., 2016]. Due to the relatively small energy gaps of the trapped ion at the involved temperatures, genuine, profound quantum effects in the single-atom piston were assumed to be non-existent. Here, we ask if it is sufficient to lower the temperature to bring the experimental setup to the quantum regime or if it is necessary to make more modifications. To answer this question, we use a higher-order, so-called quadratic, optomechanical model of the interaction between the motional degrees of freedom of the atom arising due to the tapered trap geometry of the experiment.

It was intuitively expected that an optomechanical-type mutual interaction effectively emerges when an atom is confined in a funnel-shaped trap [Roßnagel et al., 2016]. Here, we explicitly verify this intuition, but surprisingly, we find an additional degenerate three-wave mixing type coupling. It is a well-known interaction for generating squeezed states [Milburn and Walls, 1981, A.Lugiato and Strini, 1982, Yurke, 1984]. After that, we explore the signatures of the quantum squeezing in the system by differentiating classical and quantum correlations via solving master and classical stochastic Langevin equations separately. In a single atom system trapped in a tapered trap, we find that quantum correlations arise by increasing coupling strength between axial and radial modes. These quantum correlations can significantly enhance the dissipated power relative to the classical correlations. According to our model, the coupling strength depends on the trap's geometry and frequencies asymmetry. So, we indicate that the dissipated power can be enhanced by increasing the trap asymmetry and reducing the trap radius. The results show that lowering the temperature of the experiment [Roßnagel et al., 2016] per se is not sufficient to bring the single-ion engine to the quantum regime. As a result, making the trap geometry more asymmetric and the atom more confined at low temperatures make quantum squeezing type correlations more significant for a remarkable performance increase than the classical stochastic engine. Accordingly, we conclude that, in addition to lowering the temperature, the original single-atom heat engine setup in Ref. [Roßnagel et al., 2016] can be converted into a genuine quantum-enhanced heat engine in a more asymmetric and confined configuration.

This paper is organized as follows. In Sec. 5.2, we describe our Hamiltonian model to describe the experimental ion in a tapered trap system in Ref. [Roßnagel et al., 2016]. In Sec. 5.2.1, we investigate the dynamics of the system using the master equation approach. We identify an effective Otto cycle for the radial mode in Sec. 5.3. Sec. 5.4 compares the stochastic and quantum dissipated power outputs through the axial mode. We conclude in Sec. 5.5.

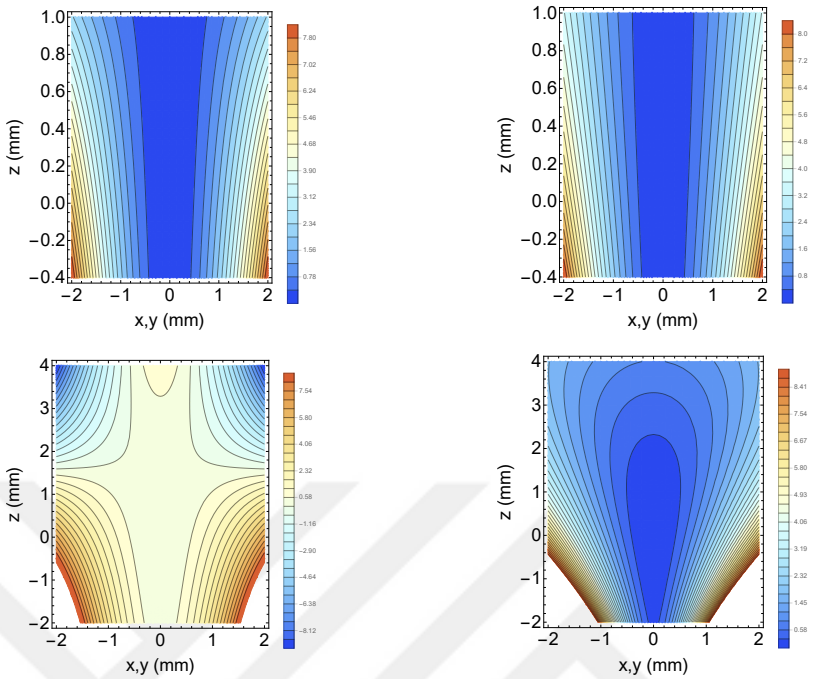

Figure 5.1: Cross sections of the approximate (Left panels) and exact (Right panels) funnel-shaped potential (in units of eV) of the tapered trap geometry. The approximation requires $z \tan\theta \ll r_0$ where $\theta = 30^o$ is the tapered trap angle and $r_0 = 1.1$ mm is the trap radius at $z = 0$. The calculations are done for the Calcium ion of mass $m = 40$u in atomic unit $u = 1.66 \times 10^{-27}$ kg.

5.2 Model System

Single ion-heat engine realized in Ref. [Roßnagel et al., 2016] consists of a Calcium ion of mass m in a tapered trap geometry. In the axial (z) direction the trap frequency is ω_z. In the directions, x, y, the trap frequencies are given by

$$\omega_\alpha = \frac{\omega_{0\alpha}}{(1+\epsilon z)^2}, \tag{5.1}$$

where $\epsilon := (\tan\theta)/r_0$. Here, $r_0 = 1.1$ mm is the radius of the trap at $z = 0$ and $\theta = 30^o$ is the trap angle. Trap frequencies along x and y axes are given as ω_{0x} and ω_{0y}, respectively. It is found that during the heat engine operation, the ion makes axial coherent oscillations with amplitude in the order of micrometers [Roßnagel et al., 2016]. Accordingly, we can consider $\epsilon z \ll 1$ for the description of heat engine

dynamics. In this limit, the trap potential,

$$U(x,y,z) = \frac{m}{2}(\omega_x^2 x^2 + \omega_y^2 y^2 + \omega_z^2 z^2), \tag{5.2}$$

can be approximated by

$$V(r,y) = \frac{m}{2}\omega_r^2 r^2(1-gz) + \frac{m}{2}\omega_z^2 z^2, \tag{5.3}$$

where $r^2 = x^2 + y^2$, and $g = 4\epsilon \approx 2.1$ (1/mm). We neglected the small difference between ω_x and ω_y and replace them with the mean radial trap frequency, $\omega_r := (\omega_{0x} + \omega_{0y})/2$ [Roßnagel et al., 2016]. The trap potential $U(x,y,z)$ (using Eq. (5.1) to define ω_x and ω_y) and its approximation by $V(r,z)$ are compared in Fig. 5.1 (right and left panels respectively). According to Fig. 5.1 (upper panels), the exact potential can be superseded by approximated potential for small values of z.

The trapped ion is always subject to a cooling laser yielding the effect of a cold thermal bath. An electrical white noise is applied to the radial degree of freedom for periodical heating as illustrated in Fig. 5.2. The heat engine system with two radial (a) and axial (b) vibrational modes (coupled by β) is shown in Fig. 5.2. Accordingly, two thermal baths at temperatures T_h and T_a couple to radial mode, and the axial mode is coupled to a bath at temperature T_b. The coupling between system and thermal bath at temperature T_h is periodically turned on and off. The engine cycle is examined classically in Ref. [Roßnagel et al., 2016], which is justified for $k_B T \gg \hbar\omega_r$, where T is considered as the working temperatures of the engine. Indeed, for all temperatures of interest, including the high-temperature condition $T_c \gg \hbar\omega_r$ is satisfied. On the other hand, the particular coupling of the axial and radial degrees of freedom in Eq. (5.3) contains a quadratic nonlinearity in r. From the quantum mechanical point of view, such a nonlinearity could yield a quantum noise squeezing effect.

Let us express the quantum model of the center-of-mass (CM) motion, in the form

$$H_0 = \frac{P_r^2 + P_z^2}{2M} + V(r,z). \tag{5.4}$$

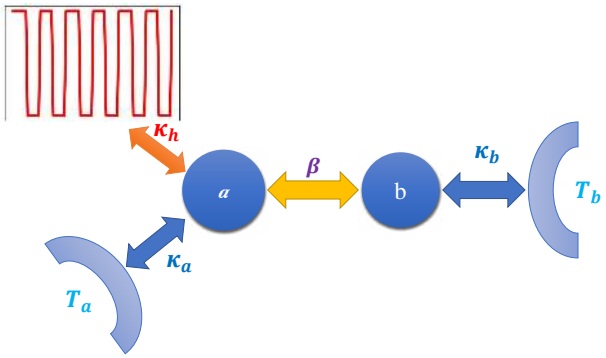

Figure 5.2: Diagram of the heat engine system based on the radial (a) and axial (b) vibrational modes whose coupling is characterized by the parameter β. Radial mode is coupled to two thermal baths at temperatures T_h and T_a, where the coupling to the bath at temperature T_h is periodically turned on and off, and the axial mode is coupled to a bath at temperature T_b. The background environment common to both modes is not shown.

Here, P_r and P_z stand for the components of the CM momentum operator, with $P_r^2 = P_x^2 + P_y^2$. We apply the harmonic-oscillator quantization $r = (\hbar/m\omega_r)^{1/2}\hat{q}_r$, $z = (\hbar/m\omega_z)^{1/2}\hat{q}_z$, $P_r = (\hbar m\omega_r)^{1/2}\hat{p}_r$, and $P_z = (\hbar m\omega_z)^{1/2}\hat{p}_z$ with $\hat{p}_r = i(\hat{a}^\dagger - \hat{a})/\sqrt{2}$, $\hat{p}_z = i(\hat{b}^\dagger - \hat{b})/\sqrt{2}$, $\hat{q}_r = (\hat{a}^\dagger + \hat{a})/\sqrt{2}$, and $\hat{q}_z = (\hat{b}^\dagger + \hat{b})/\sqrt{2}$ to write the Hamiltonian (5.4) in terms of the vibrational phonon operators, (we take $\hbar = 1$)

$$\hat{H}_{\rm cm} = \omega_r\hat{n}_r + \omega_z\hat{n}_z - \frac{\beta}{4}(\hat{a}^2 + \hat{a}^{\dagger 2} + 2\hat{a}^\dagger\hat{a} + 1)(\hat{b} + \hat{b}^\dagger), \tag{5.5}$$

where we have dropped the constants $\omega_r/2$ and $\omega_z/2$. $\beta \equiv g\omega_r\sqrt{\hbar/2m\omega_z}$ is the coupling coefficient of r and z degrees of freedom; $\hat{n}_r = \hat{a}^\dagger\hat{a}$, and $\hat{n}_z = \hat{b}^\dagger\hat{b}$ are the phonon number operators in r and z directions, respectively. We remark that the coupling coefficient β depends on trap geometry through the coupling constant g.

The Hamiltonian (5.5) can be compared to an optomechanical-like Hamiltonian, but in addition to the occupation of mode a, quantum squeezing-type correlations can induce additional pressure on mode-b to produce coherent displacement or useful work. To isolate the effects of different coupling mechanisms in Eq. (5.5), we simulate

each of them using the separate models,

$$H_{\text{om}} = \omega_r \hat{n}_r + \omega_z \hat{n}_z - \frac{\beta}{2}\hat{a}^\dagger \hat{a}(\hat{b} + \hat{b}^\dagger), \tag{5.6}$$

$$H_{\text{class}} = \omega_r \hat{n}_r + \omega_z \hat{n}_z - \frac{\beta}{4}(\hat{b} + \hat{b}^\dagger), \tag{5.7}$$

$$H_{\text{sq}} = \omega_r \hat{n}_r + \omega_z \hat{n}_z - \frac{\beta}{4}(\hat{a}^2 + \hat{a}^{\dagger 2})(\hat{b} + \hat{b}^\dagger). \tag{5.8}$$

Eq. (5.6) describes a pure optomechanical coupling where only the occupation of mode-a produces pressure on mode-b. Modes are uncoupled in Hamiltonian (5.7), but there is still an effective classical drive on mode-b. Eq. (5.8) injects coherence in mode-b depending on the squeezing of mode a.

In the next section, we will simulate the system based on total Hamiltonian Eq. (5.5) as system A_0, and each of the models in Eqs. (5.6-5.8) as systems A_1, A_2 and A_3, respectively. Let's emphasize that optomechanical coupling can not emerge per se but is always accompanied by the other classical and squeezed drive terms, and each coupling contributes with comparable or the same strengths. Our separation is artificial and only for the purpose of shedding light on the individual effects of each term on the coherent dynamics of mode-b, in particular on the work output of the single ion heat engine. We note that Ref. [Hugel et al., 2002] assumes Gaussian thermal distribution to model the spatial distribution of mode-a. This description would be closer to the classical treatment of our optomechanical model of A_1 given by Eq. (5.6).

5.2.1 Results

In this section, we introduce the parameters we used in our simulations and describe the open quantum system dynamics of the system in terms of a master equation.

5.2.2 Parameters

The experiment [Roßnagel et al., 2016] has been performed at high temperature (in the order of mK). As the usual route to the quantum regime is to reduce the temperature, we consider the temperature in the order of the μK. However, we find

that lowering the temperature is insufficient to see the system's quantum effects. It is required to demonstrate the system can harness more power than its stochastic counterpart to be classified as a genuine quantum (enhanced) heat engine [Uzdin et al., 2015]. In addition to reducing the temperature, increasing β plays a crucial role in achieving clear signatures of quantum enhancement in the heat engine operation with a single ion in a tapered trap. It is necessary to exploit quantum squeezing type correlations to enhance power output relative to the case where there are only classical correlations.

In the following, we take $T_h = 166$ μK and $T_a = T_b = 4$ μK while we suppose the atom's initial temperature is $T_0 = 10$ μK. Also, the radial and axial frequencies are taken $\omega_r/2\pi = 1$ MHz and $\omega_z/2\pi = 50$ kHz, respectively. According to the definition of the coupling coefficient ($\beta \propto \tan\theta/r_0$), we consider high trap asymmetry by taking $\theta = \pi/4$ and considering more confined traps with $r_0 \lesssim 20$ μm [Decker et al., 2019, et al, 2009] to make the coupling stronger. For example, for $r_0 \approx 2$ μm and using the aforementioned parameters, we find $\beta/2\pi = 100$ kHz. We emphasize that these parameters are not arbitrary but taken as an example from a range of values for which the temperatures are sufficiently low and squeezing type coupling is sufficiently large to get into the quantum enhanced regime of engine operation.

The dissipation rates of mode a to the cold and hot baths are considered to be $\kappa_a/2\pi = \kappa_h/2\pi = 200$ kHz, where κ_h is taken as a time-dependent square wave $\kappa_h(t) := \kappa_h u(t)$. The time-dependent part is $u(t) = 1$ for the heating and otherwise $u(t) = 0$. Also, the dissipation rate of mode b to the cold bath is $\kappa_b/2\pi = 50$ kHz.

5.2.3 The dynamics of the system

According to Eq. (5.5), the model effectively describes two nonlinearly coupled single-mode resonators. We assume a microwave white noise and a cooling laser are applied to the mode a, as shown in the experiment of Ref. [Roßnagel et al., 2016]. This continuous electrical noise and cooling laser plays the roles of two cold and heat baths at temperatures T_a and T_h such that $T_h > T_a$. An extra cooling laser beam is introduced to mode b to keep the axial mode's oscillations in control

by tuning its parameters on purpose to get a limit cycle at temperature T_b. The background environment with temperature T_0 has been ignored during the dynamics by assuming the coupling coefficient of background environment with mode b and a less than κ_j where $j \in \{h, a, b\}$ [Hardal et al., 2017]. The dynamics of the density matrix ρ of the two-resonator system is determined by the master equation [Breuer and Petruccione, 2007, Scully and Zubairy, 1997, Fink et al., 2010]

$$\begin{aligned}\frac{d\rho}{dt} &= -i[\hat{H}_\lambda, \rho] \\ &+ \kappa_a(\bar{n}_a + 1)D[\hat{a}] + \kappa_a\bar{n}_a D[\hat{a}^\dagger] \\ &+ \kappa_h(t)(\bar{n}_h + 1)D[\hat{a}] + \kappa_h(t)\bar{n}_h D[\hat{a}^\dagger] \\ &+ \kappa_b(\bar{n}_b + 1)D[\hat{b}] + \kappa_b\bar{n}_b D[\hat{b}^\dagger],\end{aligned} \tag{5.9}$$

where $\lambda =$ cm, om, class, sq represents different models and $D[\hat{\alpha}] = (1/2)(2\hat{\alpha}\rho\hat{\alpha}^\dagger - \hat{\alpha}^\dagger\rho\hat{\alpha} - \rho\hat{\alpha}^\dagger\hat{\alpha})$ refers to the Lindblad dissipator superoperators with $\hat{\alpha} = \hat{a}, \hat{b}$. Mean number of phonons in mode a and b at the bath temperature T_u and T_b is denoted by $\bar{n}_u$ with $u \in \{a, h\}$ and $\bar{n}_b$, given by the Planck distribution (we take $k_B = 1$)

$$\begin{aligned}\bar{n}_u &= \frac{1}{\exp(\omega_r/T_u) - 1}, \\ \bar{n}_b &= \frac{1}{\exp(\omega_z/T_b) - 1}.\end{aligned} \tag{5.10}$$

We assume that before the cooling and heating lasers are applied, the ion and its vibrational modes are in thermal equilibrium with the background thermal environment at temperature T_0. Initial state then can be expressed as a canonical thermal (Gibbs) state such that

$$\rho(0) \quad = \frac{1}{\mathrm{Tr}[e^{-\hat{H}_\lambda/T_0}]} e^{-\hat{H}_\lambda/T_0}, \tag{5.11}$$

and the initial states of the vibrational modes are determined by the reduced density matrices $\rho_b(0) = Tr_b(\rho(0))$ and $\rho_a(0) = Tr_a(\rho(0))$. We solve the master equation to determine $\rho(t)$ for the given $\rho(0)$ using Python programming language and an open source quantum optics package QuTiP [Johansson et al., 2013]. Taking the partial trace of $\rho(t)$ over the degrees of freedom of mode-a, we find the reduced state of the

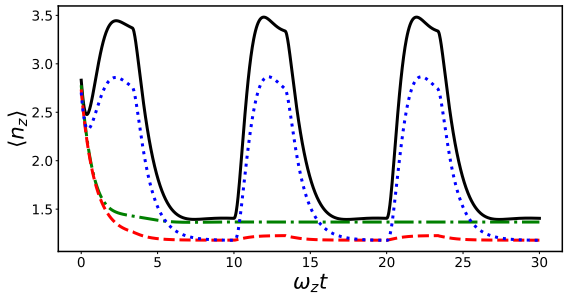

Figure 5.3: Dynamics of the mean number of vibrational phonons $\langle n_z \rangle$ in modes b where time is scaled with ω_z. The parameters used in the plots are taken to be $\omega_r/2\pi = 1$ MHz, $\omega_z/2\pi = 50$ kHz, $\bar{n}_h = 3$, and $\beta/2\pi = 100$ kHz. The solid black, dotted blue, dash-dotted green, and dashed red lines show the evolution of $\langle n_z \rangle$ under the models A_0, A_1, A_2, and A_3, respectively.

mode-b such that $\rho_b(t) = Tr_a[\rho(t)]$. Time dependence of the mean number of vibrational phonons in mode-b is evaluated by $\langle \hat{n}_z \rangle = Tr(\rho_b(t)\hat{b}^\dagger \hat{b})$. Similar calculations give dynamics of $\langle \hat{n}_r \rangle$, too.

The evolutions of $\langle \hat{n}_z \rangle$ for the four models A_0 to A_3 are shown in Fig. 5.3. Since all the models A_0 to A_3 have different Hamiltonians, the initial conditions differ. Nevertheless, the differences in the initial value of $\langle \hat{n}_z \rangle$ are too small to be visible in Fig. 5.3. Among all the terms in the overall interaction A_0, optomechanical type coupling A_1 is the only mechanism to increase the axial mode population. However, despite the qualitative agreement, A_1 per se cannot quantitatively explain the $\langle \hat{n}_z \rangle$ behavior. While the squeezing term A_3 cannot directly populate $\langle \hat{n}_z \rangle$; it plays a subtle role to increase $\langle \hat{n}_z \rangle$ beyond what is possible solely by A_1.

Intuitively, the effect of squeezing-type terms A_3 in A_0 can be interpreted as an enhancement of vibrational radial pressure on the axial mode. When A_3 terms are present, the number of radial vibrational phonons during the heating stage is expected to increase so that the optomechanical-like coupling A_1 in A_0 can yield higher $\langle \hat{n}_z \rangle$. The more radial phonons cause stronger pressure on the axial mode to transfer more energy or power. To appreciate how the quantum character of the modes enters into this picture, let us look at the dynamics of $\langle \hat{n}_z \rangle$ according to the

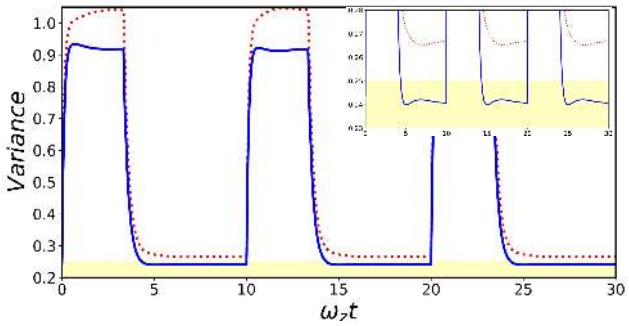

Figure 5.4: The time evolutions of the variances of the quadratures $(\langle\Delta\hat{q}_r\rangle)^2$ (red dotted line) and$(\langle\Delta\hat{p}_r\rangle)^2$ (blue solid line) of the radial mode. The inset magnifies the squeezing region where Variance $< 1/4$.

master equationn (5.9)

$$\frac{d}{dt}\langle\hat{n}_z\rangle = \frac{\beta}{\sqrt{2}}(\langle\hat{q}_r^2,\hat{p}_z\rangle + \langle\hat{q}_r^2\rangle\langle\hat{p}_z\rangle) - \kappa_b(\langle\hat{n}_z\rangle - \bar{n}_b), \tag{5.12}$$

where $\langle\hat{q}_r^2,\hat{p}_z\rangle := \langle\hat{q}_r^2,\hat{p}_z\rangle - \langle\hat{q}_r^2\rangle\langle\hat{p}_z\rangle$ is a quantum correlation function between the radial and axial modes. The dissipated power output of the engine is determined by $P_{\rm dis} = \omega_z\kappa_b(\langle\hat{n}_z\rangle - \bar{n}_b)$, which measures the net flux of energy dissipated into the environment [Mari1 et al., 2015]. In order to produce more power than a stochastic engine that can only have classical correlations, it is necessary for us to ensure that the system has strong quantum correlations associated with the second moment of the displacement of the radial mode. Quantum character of the $\langle\hat{q}_r^2\rangle$ can be examined in terms of the quadrature variances of the radial mode

$$(\langle\Delta\hat{q}_r\rangle)^2 = Tr[\rho_a\hat{q}_r^2] - (Tr[\rho_a\hat{q}_r])^2, \tag{5.13}$$

$$(\langle\Delta\hat{p}_r\rangle)^2 = Tr[\rho_a\hat{p}_r^2] - (Tr[\rho_a\hat{p}_r])^2, \tag{5.14}$$

where $\rho_a(t) = Tr_b[\rho(t)]$ is the reduced density matrix of the radial mode. When a quadrature variance is less than its vacuum value of 1/4, the state is said to be quadrature squeezed.

The time evolutions of $(\langle\Delta\hat{q}_r\rangle)^2$ (red dotted line) and $(\langle\Delta\hat{p}_r\rangle)^2$ (blue solid line) are shown in Fig. 5.4. The yellow shaded area, where Variance $< 1/4$, in Fig. 5.4 indicates that the radial mode starts each cycle in a squeezed thermal state. Fig. 5.5

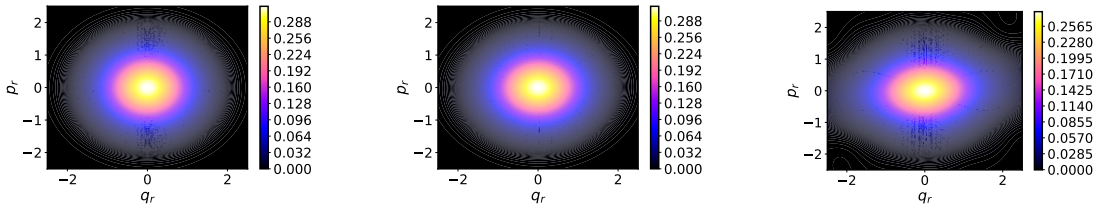

(a) (b) (c)

Figure 5.5: Colour online)(a)-(c) The Wigner functions in the p_r, q_r field quadrature phase space of the radial mode plotted for (a) $\beta/2\pi = 10$ kHz, (b) $\beta/2\pi = 100$ kHz, (c) $\beta/2\pi = 200$ kHz. The other system parameters are $\omega_r/2\pi = 1$ MHz, $\omega_z/2\pi = 50$ kHz.

plots the Wigner functions of the radial mode for different β, at the same scaled time after thermalization of the system, when the system dynamics is governed by the full model A_0. Wigner function of a thermal state in the quadrature phase space has circular contours, which are changed to ellipses due to quadrature squeezing. In the Fig. 5.5, we show that although the quadrature phase space of radial mode has circular contours for small β (Fig. 5.5 (a)), it becomes to ellipses contours by enhancing β (figs. 5.5 (b,c)). So, for small β, the eccentricity is almost zero, and the squeezing is negligible even at low temperatures. Accordingly, the dissipated power of the engine will be dominated and determined by the classical correlations only. On the other hand, for large values of β, second order moments of the displacement operator should be treated quantum mechanically in Eq. 5.12 and hence to the calculation of the dissipated power. We present explicit calculation of P_{dis} for both quantum and classical stochastic treatments in Sec. 5.4.

5.3 Effective Otto Cycle For the Radial Mode

For a single ion in an asymmetrical Paul trap [Roßnagel et al., 2016], the hot bath is simulated by the external white electric-field noise. The cold bath interaction is realized by exposing the ion to the laser cooling beam. According to [Roßnagel et al., 2016, Levy et al., 2020], the cooling laser is kept on during the process. Despite the continuous coupling to the heat baths, we can identify an Otto engine

cycle in our model. We consider the mode a as the working substance and treat the mode b as the engine's flywheel where the work is stored. We replace the flywheel displacement $q_z = \langle \hat{b} + \hat{b}^\dagger \rangle$ as a number in model A_0. The reduced semi-quantum model describes a squeezed oscillator Hamiltonian for mode a, whose diagonalization by the Bogoluibov transformation (see .1.) yields an effective frequency of ω_{eff}, and the effective mean energy can be defined as $U = \langle H'_{\text{cm}} \rangle$.

The Otto engine is identified in Fig. 5.6 with four steps [Levy et al., 2020].

(A→B) Hot isochore: the effective trapping frequency (ω_{eff}) is kept constant at ω_h while contacting with hot bath at temperature T_h. The thermalization will be done after a time of τ_h.

(B→C) Adiabatic expansion: The atom evolves in the trapping potential while isolated from the hot bath. After a time τ_z, the effective frequency will be changed from ω_h to ω_c, and work will be done by considering the displacement in the axial direction.

(C→D) Cold isochore: the effective frequency remains in ω_c, and the cold bath with temperature T_c is contacted with the system for a time τ_c.

(D→A) Adiabatic compression: the effective frequency returns to the initial frequency another time τ_z in the last step.

The time scales can be considered by $\tau_h \approx \tau_c < \tau_z$. An effective, finite-time (non-ideal) Otto cycle (ABCD) is defined in the diagram (Fig. 5.6) where we plot dependence of U on ω_{eff} in the steady state at $\bar{n} = 3$.

5.3.1 Performance of the engine

We have seen that the engine operates by converting the thermal energy harvested by the radial mode into coherent oscillations of the axial vibrational mode. We can envision the vibrational mode as the work reservoir storing coherent energy and examine the engine cycle for the radial mode. For that aim, let's consider a semi-classical model of the vibrational interaction by replacing the coherent axial mode operators, in particular q_z operator in the vibrational coupling with a c-number, which is its expectation value. After that, we can apply the Bogoluibov transforma-

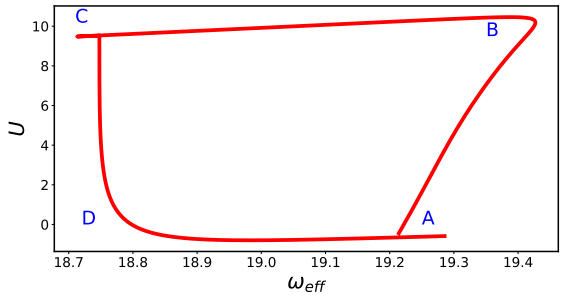

Figure 5.6: Effective energy-frequency diagram of the radial mode a by considering the dependence of the mean effective energy U to the effective frequency ω_{eff} (in units of $\hbar\omega_z$).

tion (as described in .1) to the effective semi-classical model, which yields a simple uncoupled quantum oscillator model. Accordingly, we conclude that the vibrational modes, particularly the radial mode, are Gaussian states under the semi-classical model. More specifically, the radial mode is a Gibbsian (thermal equilibrium) Gaussian state for which a simple Von-Neumann entropy expression can be derived in the form [Hardal et al., 2017]

$$S = (1 + \langle \hat{n}_c \rangle) \ln(1 + \langle \hat{n}_c \rangle) - \langle \hat{n}_c \rangle \ln(\langle \hat{n}_c \rangle). \tag{5.15}$$

The effective temperature of the radial mode Gibbsian state is given by

$$T_{\text{eff}} = \omega_{\text{eff}} / \ln(1 + 1/\langle \hat{n}_c \rangle). \tag{5.16}$$

Here, the $\langle \hat{n}_c \rangle$ comes from the diagonalized form of radial mode in Hamiltonian employing Bogoliubov transformation (.1).

The temperature-entropy $T - S$ diagram is plotted in Fig. 5.3.1 which closely resembles an Otto engine. The potential work output can be obtained by calculating the area of the T-S diagram. We approximate the work from the T-S diagram, and the net work is estimated by $W \approx 0.22\ \hbar\omega_z \simeq 7.3 \times 10^{-30}$ joules. The Power can be calculated by dividing work by the cycle time $T = 20 \times 2\pi/\omega_z$ as $P \simeq 2.9 \times 10^{-27}$ Watts. The determined heat intake of mode a is $Q_{\text{in}} \simeq 3 \times 10^{-28}$ joules, and therefore the efficiency is $\eta \simeq 2.4\%$.

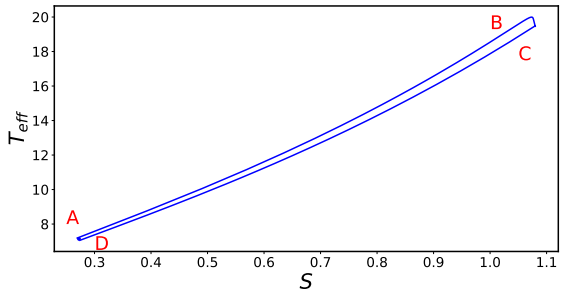

Figure 5.7: T-S diagram of the mode a which closely resembles that of an Otto engine (in units of $\hbar\omega_z$)

.

The coupling coefficient β in Hamiltonian (5.5) plays an essential role in producing work and achieving higher efficiency, which can be done by revising the trap's geometry in the experiment [Roßnagel et al., 2016]. Engine performance improves by applying the quantum correlations, which are significant only for much higher coupling regimes and at low temperatures. According to the definition of $\beta \propto 1/r_0$, we can increase β by lowering the trap's radius r_0. As we argued in Sec. 5.2.2, sufficiently large β can be achieved by reducing the trap's radius to the micrometer scale. Fig. 5.8 shows the dependence of the extracted work, determined by the area of the $T-S$ diagram, on r_0. Here, θ, radial, and axial frequencies are kept constant so that β increases with r_0. It can be pointed out that the work output increases strongly in tightly confined tapered traps. We remark, however, that increasing the coupling coefficient β is limited in our treatment where we use a local optomechanical master equation, which requires β to be smaller than the radial frequency [Naseem et al., 2018].

5.4 Classical vs Quantum Heat Engine Regimes

The previous section identifies an effective Otto cycle by treating the radial mode as a working fluid and assuming the coherent displacements of axial mode are classical. This treatment allows us to use conventional thermodynamic cycle diagrams

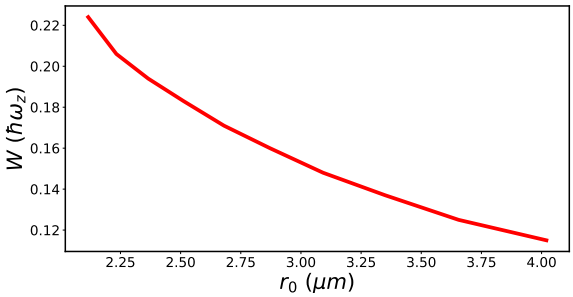

Figure 5.8: Extracted work W (in unit of $\hbar\omega_z$) versus trap's radius r_0 (μm) where radial and axial frequencies are constant ($\omega_r/2\pi = 1$ MHz, and $\omega_z/2\pi = 50$ kHz) and $\theta = \pi/4$.

in terms of mean effective energy, effective temperature, effective frequency (spatial-like parameter), and entropy for our reduced quantum oscillator model for the radial mode. In this case, the potential work output of the effective Otto cycle is computed from the $T - S$ diagram. The missing piece of this engine picture is the flywheel, which is the axial mode. The work is translated to the piston (axial) mode, and it is determined in terms of the dissipated power through the axial mode, which we will calculate in the present section. Dissipated power is essentially determined with the population of the axial mode (mean number of axial phonons). As we have seen in Sec. 5.2.1, the dynamical equation of the mean number of axial phonons includes a quantum correlator term, which can be significant on top of classical correlations when quantum squeezing is present and can enhance the dissipated power. When there are only classical correlations, we solve the Langevin equations to determine the mean number of axial phonons. In addition, we determine the mean number of axial phonons from the quantum master equation as well. Using these two methods, we will determine the mean number of phonons to be substituted to the same dissipated power formula to compare the classical and quantum dissipated power outputs with each other.

To compare the quantum engine with its classical counterpart, we follow the standard method of neglecting the non-commutative character of the quantum operators (for example, position and momentum operators). In the optomechanical

engine models, they are replaced with c-numbers, $\langle\hat{a}\rangle \rightarrow \upsilon_r$ and $\langle\hat{b}\rangle \rightarrow \upsilon_z$ [Hardal et al., 2017, Mari1 et al., 2015]. The Heisenberg equations of motion are then changed to classical Langevin equations, which further include the stochastic noise terms describing the classical models of the heat baths in the form

$$\begin{aligned}
\dot{\upsilon}_r &= -i\left(\omega_r\upsilon_r - \frac{\beta}{2}(\upsilon_r^* + \upsilon_r)(\upsilon_z + \upsilon_z^*)\right) \\
&\quad - \frac{\kappa_r + \kappa_h}{2}\upsilon_r + \xi_h(t) + \xi_r(t), \\
\dot{\upsilon}_z &= -i\left(\omega_z\upsilon_z - \frac{\beta\upsilon_z}{4}(\upsilon_r^2 + \upsilon_r^{*2} + 2\upsilon_r\upsilon_r^* + 1)\right) \\
&\quad - \frac{\kappa_b}{2}\upsilon_z + \xi_z(t).
\end{aligned} \tag{5.17}$$

Here $\xi_k(t)$ presents time dependent delta-correlated and temperature dependent stochastic noise terms where $k = r, z, h$ [Hardal et al., 2017, Mari1 et al., 2015].

Defining the field quadratures X_i, Y_i as $\upsilon_i = 1/\sqrt{2}(X_i + iY_i)$, and writing the noise parameters as $\xi_i = 1/\sqrt{2}(\xi_x^i + i\xi_y^i)$ where $i = r, z$ we can simulate the equations as:

$$\begin{aligned}
dX_r &= \left(\omega_r Y_r - \frac{\kappa_a + \kappa_h}{2}X_r\right)dt + dW_x^h + dW_x^a, \\
dY_r &= \left(-\omega_r X_r + \sqrt{2}\beta X_r X_z - \frac{\kappa_a + \kappa_h}{2}Y_r\right)dt + dW_y^h + dW_y^a, \\
dX_z &= \left(\omega_z Y_z - \frac{\kappa_b}{2}X_z\right)dt + dW_x^b, \\
dY_z &= \left(-\omega_z X_z + \frac{\sqrt{2}\beta}{4}(4X_r^2 + 1) - \frac{1}{2}\kappa_b Y_z\right)dt + dW_y^b.
\end{aligned} \tag{5.18}$$

Here, $dW^i = 1/\sqrt{2}(dW_x^i + idW_y^i)$ where $\xi_k^i dt = dW_k^i$, with $k = x, y$, is the Wiener process with width $\sqrt{\kappa_i\bar{n}_i dt}$.

We solve these equations to determine the mean number of phonons,

$$\langle\hat{n}_z\rangle = \frac{1}{2}(X_z^2 + Y_z^2), \tag{5.19}$$

which is then used to determine the dissipated power. The calculation is then repeated using the quantum master equation instead of the Langevin equations. Fig. 5.9 shows the maximum dissipated power output of classical and quantum calculations versus β. It reveals that the quantum model enables power outputs

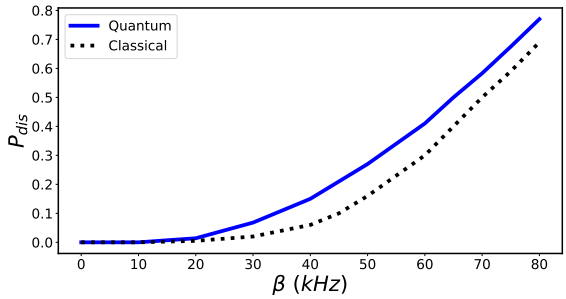

Figure 5.9: The maximum dissipated power (in units of $\hbar\omega_z$) concerning coupling constant β (in units of kHz). The black dashed and solid blue curves show the results of classical and quantum simulations, respectively.

that greatly exceed the power of stochastic engines for large β, which identifies the regime in which the system can be classified as a genuine quantum heat engine (according to the criteria in Ref. [Uzdin et al., 2015]).

The quantum correlation contributions to the engine performance are negligibly small in the single-ion heat engine experiment [Roßnagel et al., 2016], and it should be classified as a classical heat engine even at low temperatures according to the criteria of Ref. [Uzdin et al., 2015]. It is necessary to modify the setup by increasing the asymmetry of the tapered trap and decreasing the trap's radius (to increase β) to bring the single-ion engine of Ref. [Roßnagel et al., 2016] to the domain of quantum heat engines. According to our calculations, the dissipated power output of the engine overcomes the stochastic classical power output with the help of quantum correlations when $\beta \geq 20$ kHz. As an example, to reach this condition by using the parameters defined in Sec. 5.2.1 we can use $\theta = 45^o$ and $r_0 \leq 10$ μm.

5.5 Conclusion

In summary, we examined the single-atom heat engine using the asymmetric trap configuration of experiment Ref. [Roßnagel et al., 2016] employing a quadratic optomechanical model. In our model, the working fluid mode (radial mode) was simultaneously driven by the contribution of optomechanical, classical, and squeezed terms. We clarified the effects of the coherent and squeezing couplings on the en-

gine's operation beyond the standard optomechanical coupling. Furthermore, it was found that the coupling coefficient β plays a critical role in increasing quantum correlations contribution and enables power outputs that greatly exceed the power of stochastic engines. We showed that the engine should perform in a high coupling and low-temperature regime to benefit from the quantum correlations. According to our calculations, the quantum character of the second order moments of the displacement operator emerges by increasing β. In the strong coupling regime, the radial mode is in a thermal squeezed state, and as a result, the system treats quantum mechanically. The coupling coefficient depends on the trap's geometry and the frequencies asymmetry, so adjusting the trap's geometry asymmetry and reducing the trap's radius can increase the efficiency and work of the engine. We concluded that a single atom heat engine in a more confined and asymmetric trap operates in the quantum regime where the dissipated power is more significant than its classical counterpart with only classical stochastic correlation.

Chapter 6

ATOM-FIELD INTERACTION IN A SUB-DIFFRACTION HOLLOW SHAPE TRAP

6.1 Introduction

Atom–light interaction at the single quantum level plays a vital role in many quantum communication and computation protocols. The strong interaction of light with an atom is needed to transfer a photonic qubit into internal atomic degrees of freedom as a stationary qubit. This process is critical to implement quantum light-matter interfaces. In this section, we extend the original theoretical model of atom-light interaction in the free space to apply in the strong focusing regime. We investigate the interaction strength between light and an atom in realistic focusing geometries by considering thermal fluctuations of the trapped atom, which depends on temperature and trap frequency[Teo and Scarani, 2011].

Thermal fluctuations are essential in free space atom-field interaction [Teo and Scarani, 2011]. We show how the trap's width can affect the atom field coupling averaging over the atomic spatial profile. We consider a single atom trapped in a tight blue-detuned potential interacting with a field focused by a lens system, as shown in Fig. 6.1. We investigate the scattering rate and the effects of the trap frequency on the scattering rate as a measurement for the atom-field interaction strength in the presence of thermal fluctuations. Finally, we present a method to design a sub-diffraction blue-detuned trap using a self-interference technique introduced in [Tang et al., 2016].

6.2 Generating a Sub-diffraction Blue-detuned Trap

We present a setup including a balanced Mach-Zehnder interferometer introduced in Ref. [Tang et al., 2016] and a lens system to trap an atom located at the focal point in a sub-diffraction regime, as shown in Fig. 6.1. According to Fig. 6.1, the interferometer consists of a proper delay Φ in one arm and an image inverter in the other. The output field in the arm associated with destructive interference for on-axis light is monitored where the output arm is sensitive to separating the point sources. The presented method is based on a self-interference technique for determining the separation between two incoherent point sources [Tang et al., 2016]. The output field propagates into a lens to focus on the focal point.

We consider the input electric field after passing a single-mode fiber propagate into the interferometer, which can be approximated with a Gaussian beam in cylindrical coordinate (ρ, z),

$$\boldsymbol{E}_{in}(\rho, z) = E_0 \exp\big(-\rho^2/w(z)^2\big)\boldsymbol{\epsilon}_+. \tag{6.1}$$

Here $\boldsymbol{\epsilon}_\pm = (\boldsymbol{x} \pm i\boldsymbol{y})/\sqrt{2}$ is the circular polarization of the beam, E_0 is the amplitude and $w(z) = w_0[1 + (z/z_R)^2]$ represents the beam's width at z where $z_R = \pi w_0^2/\lambda$ is the Rayleigh range.

The output electric field before lens 1 (Fig. 6.1), generated from self-interference of the propagating beams in two arms of the interferometer, is calculated by [Tang et al., 2016]

$$\boldsymbol{E}_{out}(\rho, z = z_0) = \boldsymbol{E}(\rho + d, z) - \boldsymbol{E}(\rho - d, z), \tag{6.2}$$

where d is the source's separation from the centroid vector form.

We use experimental parameters presented in Ref. [Chen et al.,] as the input field's wavelength $\lambda = 632.8$ nm, $w_0 = 331$ μm where we consider the source's separation $d = w_0$. The normalized intensity ($I_{out} = 2\epsilon_0 c|E_{out}/E_0|^2$), obtained from Eq. (6.2), is shown in Fig. 6.2 where output light's peak-to-peak diameter is about 1118 λ. The first lens transforms the output beam into a spherical wavefront toward the focal point $z = z_0 + f$.

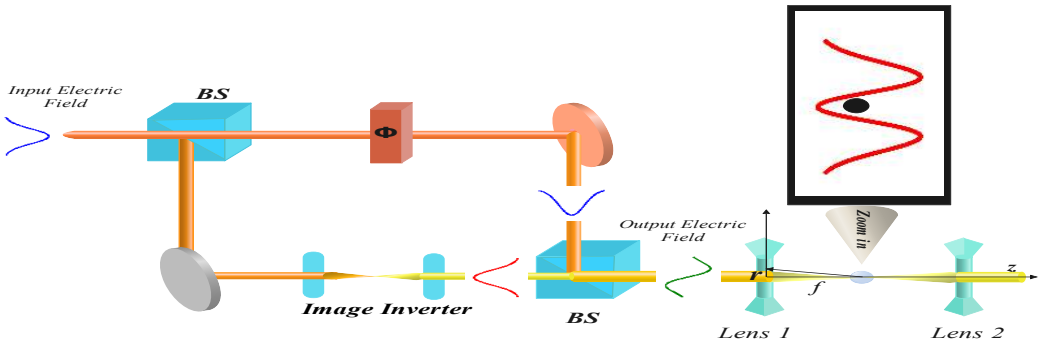

Figure 6.1: The schematic of an experimental setup to trap a single atom in a tight blue-detuned trap potential. The setup includes a balanced Mach-Zehnder interferometer and a lens system to focus the output beam in the focal point where a single atom is located. The interferometer contains an appropriate delay, Φ, in one arm and an image inverter in the other. We implement a self-interference technique to make a hollow shape beam before the first lens. After the first lens, the output beam propagates to the focal point. The inset figure shows the zoom-in of the trap potential in the focal point.

The electric field at the focal point can be calculated by [van Enk and Kimble, 2001] when we consider the first lens located at $z = z_0$,

$$E(\rho, z = z_0 + f) = \int_0^k dk_t \sum_{s=\pm} k_\mu \frac{1}{4\pi} \frac{sk + k_z}{k} j_1(k_t\rho) \exp(ik_z z), \tag{6.3}$$

where

$$k_\mu = 2\pi k_t \int_0^{2\pi} d\phi \int_0^{\infty} \rho d\rho \times E_{out}(\rho, z = z_0) \frac{1}{4\pi} \frac{sk + k_z}{k} j_1(k_t\rho) \exp(-ik_z z). \tag{6.4}$$

Here we suppose $z_0 = 276$ mm based on the experimental data in Ref. [Chen et al.,].

Considering lens' radius $R = 500\ \lambda$ and $f = 600\ \lambda$, the numerical aperture (NA) of the lens will be $NA = \sin[\arctan(f/R)] = 0.64$ [Chen et al.,]. Therefore, we can calculate the diffraction limit by $d_{diff} = 0.5\lambda/NA = 0.78\lambda$.

Implementing Eq. (6.3), the electric field distribution at the focal plane is depicted in

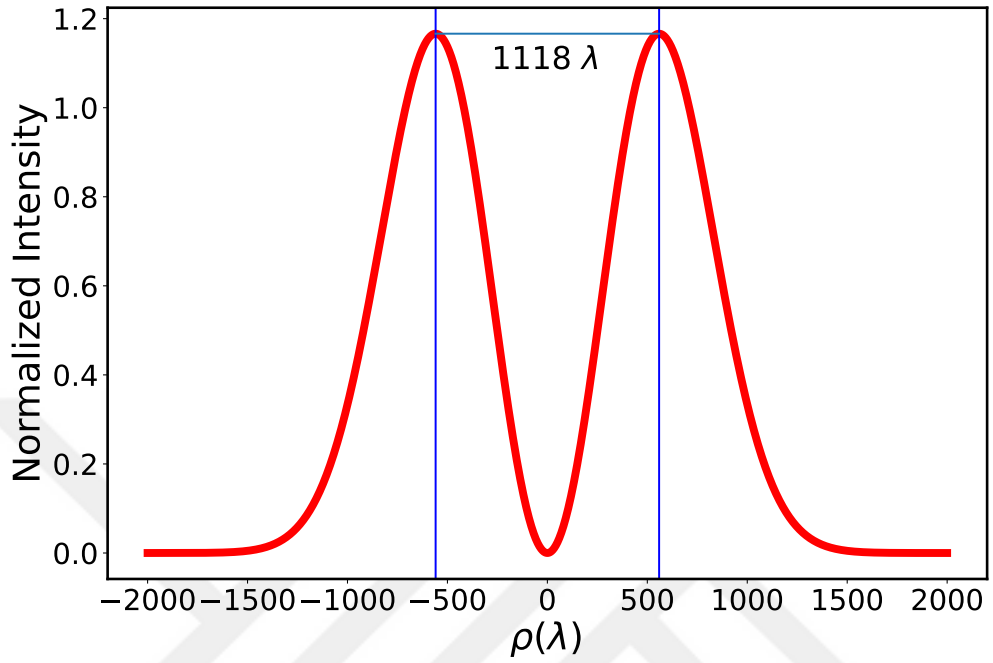

Figure 6.2: The normalized intensity distribution of the incident light where $w_0 = 331\ \mu$m, $z = z_0 = 276$ mm, and $\lambda = 632.8$ nm. The plot is scaled by $\lambda = 1$, and we consider $d = w_0$ where the peak-to-peak diameter of the beam is obtained as $pp = 1118\ \lambda$.

Fig. 6.3. We find that the peak-to-peak diameter at the focal point is $pp_f = 0.59\ \lambda$, which is less than the diffraction limit $pp_f < d_{diff}$.

We can use the presented configuration to trap an atom at the focal point when the frequency of the input light is larger than the atom's frequency. Therefore, a blue-detuned dipole trap with an under-diffraction radius can be applied to keep the atom more confined.

6.2.1 Dipole Trap

In interacting atoms with far-detuned light, the optical excitation is very low, and the radiation force due to photon scattering is negligible compared to the dipole force. The optical dipole force arises from the dispersive interaction of the induced atomic dipole moment with the intensity gradient of the light field [Cook, 1979,

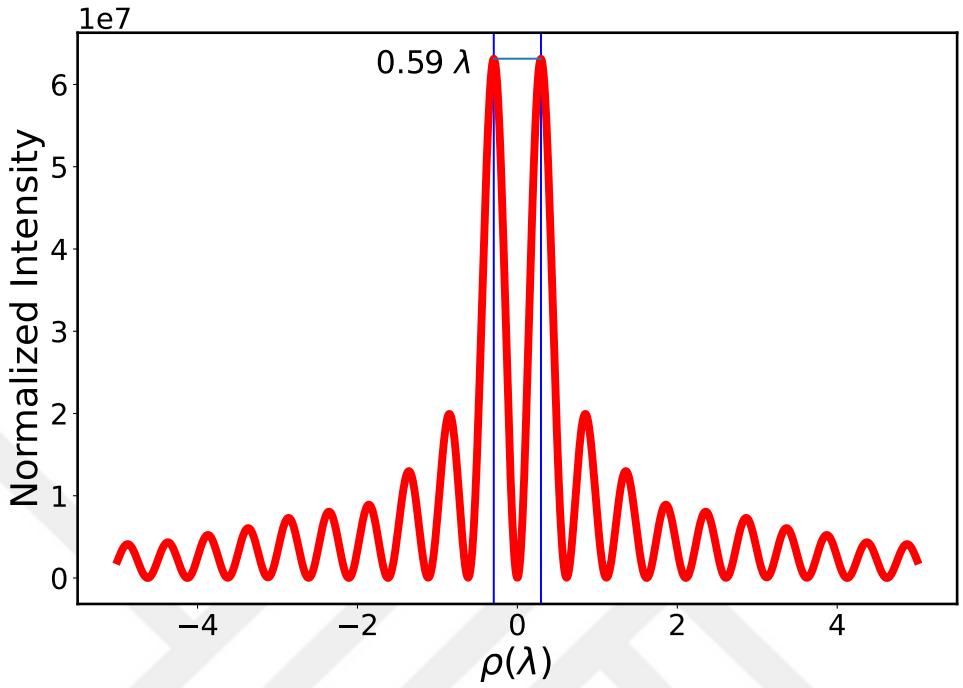

Figure 6.3: The designed intensity on the focal plane at $z = z_0 + f$, where the plot is scaled by $\lambda = 1$ and focal length is $f = 600\ \lambda$, and the focal beam's peak-to-peak diameter is $pp_f \approx 0.59\ \lambda$.

Gordon and Ashkin, 1980]. Because of its conservative character, the force can be derived from potential, the minima of which can be used for atom trapping. The interaction potential of the induced dipole moment in the driving field in rotating wave approximation is given [R.Grimm et al., 2000]

$$U_{dip}(\rho, z) = \frac{3\pi c^2}{2\omega_0^3} \frac{\Gamma}{\Delta} I(\rho, z), \tag{6.5}$$

where ω_0, and ω are the atomic and incident field frequency, and $\Delta = \omega - \omega_0$ is the detuning. $I(\rho, z) = 2\epsilon_0 c|E(\rho, z)|^2$ is the incident light intensity. Here,

$$\Gamma = \frac{\omega_0^3}{3\pi\epsilon_0\hbar c^2} |\langle e|\, \mu\, |g\rangle|^2, \tag{6.6}$$

where the atom is considered a two-level quantum system interacting with the classical radiation field (semi-classical approach), and the saturation effects can be neglected. $\mu = \boldsymbol{\mu}.\boldsymbol{\epsilon}$ is the projection of the electric dipole operator on the polarization

direction $\boldsymbol{\epsilon}$ of the electric field. The dipole interaction repels atoms out of the field when ($\Delta > 0$), which is called blue detuning, and potential minima correspond to the intensity minima [R.Grimm et al., 2000].
The trap's frequency is proportional to the inverse of the beam's radius $\omega_{trap} \propto 1/w$. Therefore, trap frequency increases by reducing the trap width.

The following section illustrates how the trap's frequency affects the atom-field interaction. We employ the results of Ref. [Teo and Scarani, 2011] to show that a more confined atom makes the atom-field interaction stronger by evaluating the atom's thermal fluctuation in the trap.

6.3 Atom-Field Interaction

Consider a two-level atom at the focal point of a lens illuminated by a focused weak monochromatic light as a prob field with an incident power P_{in}. The prob's interaction strength with the atom corresponds to the fraction of power scattered by the atom. Consequently, the atom-field coupling strength can be measured by calculating the scattering ratio.

6.3.1 Scattering Ratio

Consider a focused weak monochromatic light field interacting with a single two-level atom localized at focus. The interaction strength is directly related to the fraction of power scattered by the atom.

$$R_{sc} = \frac{P_{sc}}{P_{in}}, \tag{6.7}$$

where P_{in}, and P_{sc} denote incident and scattered power, respectively.

After passing through the single-mode fiber, the incident electric field can be approximated by a the Gaussian field,

$$E_{in} = E_0 \exp\left(-\rho^2/w_{in}^2\right)\boldsymbol{\epsilon}_+. \tag{6.8}$$

Here $\boldsymbol{\epsilon}_+ = (\boldsymbol{x} + i\boldsymbol{y})/\sqrt{2}$ is the polarization of the field, E_0 is the amplitude, and w_{in} represents the width of the incident beam. The incident beam carries a power of

$$P_{in} = \frac{1}{4}\epsilon_0 \pi c E_0^2 w_{in}^2, \tag{6.9}$$

where ϵ_0 and c are the vacuum's electric permittivity and the light's speed. The optical power scattered by the atom can be defined by the product of energy splitting, decay rate, and population of the excited state [Cohen-Tannoudji et al., 1998, Tey et al., 2009],

$$P_{sc} = \frac{3\epsilon_0 c \lambda^2 E_A^2}{4\pi}, \tag{6.10}$$

where E_A indicates the field's amplitude at the focus.

Using Eqs. (6.9) and (6.10), the scattering ratio is

$$R_{sc} = \frac{P_{sc}}{P_{in}} = \frac{3\lambda^2}{\pi^2 w_{in}^2}\left(\frac{E_A}{E_0}\right)^2, \tag{6.11}$$

which is obtained under weak and on-resonant excitation. $|E_A|$ can be calculated by [Tey et al., 2009]

$$|E_A| = \sqrt{\frac{k^2 P_{in}}{4\epsilon_0 c}}\ \frac{e^{1/u^2}}{u}\left(\frac{1}{u}\Gamma\left(-\frac{1}{4}, \frac{1}{u^2}\right) + \sqrt{u}\Gamma\left(\frac{1}{4}, \frac{1}{u^2}\right)\right). \tag{6.12}$$

The fraction R_{sc} of the optical power scattered away by a two-level atom is approximated by calculating the amplitude E_A of the electrical field at the focus. So, the scattering ratio is [Tey et al., 2009]

$$R_{sc} = \frac{3\ e^{2/u^2}}{4u^3}\left(\Gamma\left(-\frac{1}{4}, \frac{1}{u^2}\right) + u\Gamma\left(\frac{1}{4}, \frac{1}{u^2}\right)\right)^2, \tag{6.13}$$

where, $u := w_{in}/f$ defined as the focusing strength, and *Gamma* denotes the incomplete gamma function $\Gamma(a, b) = \int_0^\infty s^{a-1}e^{-s}ds$.

6.3.2 Effects of the Thermal fluctuations on Scattering Ratio

In the previous section, we supposed the atom is fixed at the focus. However, in experiments, the atom is held in a dipole trap at a particular temperature, inducing the incoming beam's Doppler shift and spatial effects [Teo and Scarani, 2011]. Here

we investigate the spatial effects by averaging the scattering ratio over the atomic spatial profile. For any function $f(\boldsymbol{\rho})$, which relies on the position of the atom, the average value will be given by [Teo and Scarani, 2011]

$$\langle f(\boldsymbol{\rho})\rangle \approx \frac{1}{Z}\int e^{-V(\boldsymbol{\rho})/k_BT} f(\boldsymbol{\rho}) d^3\boldsymbol{\rho}, \tag{6.14}$$

where the dipole potential is approximated by a harmonic oscillator $V(\boldsymbol{\rho}) = m\omega_\rho^2\rho^2/2$, and Z is the partition function in a classic canonical ensemble, and ω_ρ shows the trap's frequency. Here, we use a cylindrical coordinate while ignoring the fluctuations in axial z direction to simplify.

The measured scattering is the averaged scattering, weighted in the canonical ensemble as in shown Eq. (6.14),

$$\langle R_{sc}(\boldsymbol{\rho})\rangle \approx \frac{1}{Z}\int_0^{2\pi} d\phi \int_0^{\infty} \rho d\rho \exp\left(-\frac{m\omega_\rho^2\rho^2}{2k_BT}\right) R_{sc}(\rho). \tag{6.15}$$

$|E_A|$ can be obtained by finding the dimensionless field $\boldsymbol{F}$ at focus [van Enk and Kimble, 2001],

$$|E_A| = \frac{1}{w_{in}}\sqrt{\frac{4P_{in}}{\pi\epsilon_0 c}}|\boldsymbol{F}|, \tag{6.16}$$

where, the dimensionless field $\boldsymbol{F}$ is given by

$$\boldsymbol{F} = \frac{-ik\sqrt{f}}{2}\frac{\left(f+\sqrt{f^2+\rho^2}\right)}{\left(f^2+\rho^2\right)^{5/4}}\exp\left(\rho^2/w_{in}^2\right)\boldsymbol{\epsilon}_+. \tag{6.17}$$

Here, $k = 2\pi/\lambda$ is the incident beam's wave number, and f is focal length. Therefore, the scattering rate by averaging over spatial profile, considering atomic thermal fluctuations, will be

$$\langle R_{sc}\rangle = \frac{3\lambda^2}{\pi^2 w_{in}^2}\langle|\boldsymbol{F}|^2\rangle, \tag{6.18}$$

The scattering ratio R_{sc} corresponds to focusing strength u is shown in Fig. 6.4, where the dotted-black curve denotes R_{sc} at focus and solid curves indicate the average scattering $\langle R_{sc}\rangle$ for different trap frequencies at constant temperature $T =$ 10 μK. It demonstrates that R_{sc} as a measurement of the atom-field interaction declines by averaging over atomic spatial profile. Moreover, $\langle R_{sc}\rangle$ decreases by

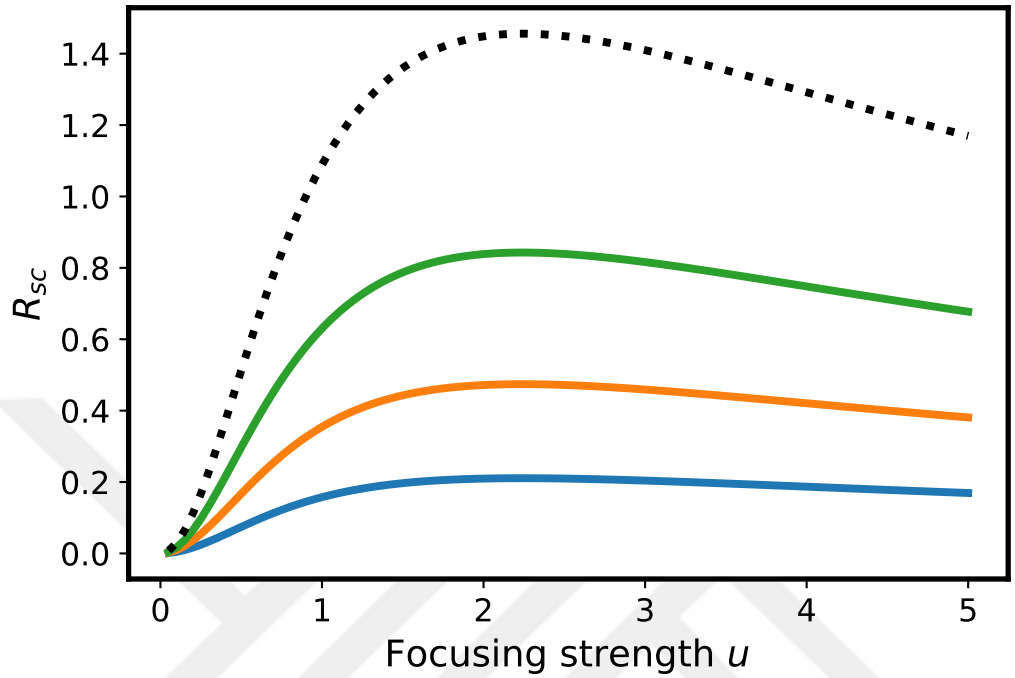

Figure 6.4: The scattering ratio R_{sc} vs. focusing strength u for different trap frequencies in constant temperature $T = 10$ μK. The dashed black curve displays the scattering ratio in focus, while the solid curves demonstrate R_{sc} for frequencies 0.5, 0.75, and 1 MHz down to up, respectively.

reducing trap frequency, as shown in Fig. 6.4 where the solid curves from up to down represent $\langle R_{sc} \rangle$ for $\omega_\rho = 1$, 0.75, and 0.5 MHz, respectively. We show that trap's frequency increases by reducing the trap's width in the previous section (Sec. 6.2). Therefore, it can be concluded that the coupling strength between the atom and the incident field is stronger for a more confined atom.

Chapter 7

CONCLUSION

In this thesis, we have investigated the atom-field interaction and demonstrated its applications in quantum thermal machines. We have examined the possibility of manipulating thermodynamic processes for enantiomers detection. We found that relying on the phase and detuning of the optical fields, the left- and right-handed cyclic three-level system displayed distinct thermal functions when subjected to an Otto cycle.

We studied the atom trap system and examined the single-atom heat engine employing the asymmetric trap configuration of experiment Ref. [Roßnagel et al., 2016] using a quadratic optomechanical model. We indicated that the engine should act in a high coupling and low-temperature regime to profit from the quantum correlations. We concluded that a single-atom heat engine in a more confined and asymmetric trap works in the quantum regime where the dissipated power is more important than its classical counterpart with only a classical stochastic correlation.

To make the atom more confined, we continued analyzing diploe trap geometry. We presented a method to create a tight blue-detuned trap with a radius of under-diffraction limit. Also, we demonstrate that a more confined trap improves the atom-field coupling strength in realistic focusing geometries by considering the thermal fluctuations of the atom.

BIBLIOGRAPHY

[Abah et al., 2012] Abah, O., Roßnagel, J., Jacob, G., Deffner, S., Schmidt-Kaler, F., Singer, K., and Lutz, E. (2012). Single-ion heat engine at maximum power. *Phys. Rev. Lett.*, 109:203006.

[Aharonov et al., 1993] Aharonov, Y., Anandan, J., and Vaidman, L. (1993). Meaning of the wave function. *Phys. Rev. A*, 47:4616.

[Aharonov and Vaidman, 1993] Aharonov, Y. and Vaidman, L. (1993). Measurement of the schrödinger wave of a single particle. *Phys. Lett. A*, 178:38–42.

[Altintas et al., 2014] Altintas, F., Hardal, A. U. C., and Mustecaplıoglu, O. E. (2014). Quantum correlated heat engine with spin squeezing. *Phys. Rev. E*, 90:032102.

[Altintas et al., 2015] Altintas, F., Hardal, A. U. C., and Mustecaplıoglu, O. E. (2015). Rabi model as a quantum coherent heat engine: From quantum biology to superconducting circuits. *Phys. Rev. A*, 91:023816.

[Altintas and Mustecaplıoglu, 2015] Altintas, F. and Mustecaplıoglu, O. E. (2015). General formalism of local thermodynamics with an example: Quantum otto engine with a spin-1/2 coupled to an arbitrary spin. *Phys. Rev. E*, 92:022142.

[A.Lugiato and Strini, 1982] A.Lugiato, L. and Strini, G. (1982). Production of squeezed states in a degenerate parametric amplifier. *Opt. Commun.*, 41:67.

[Ariens, 1986] Ariens, E. J. (1986). Stereochemistry: A source of problems in medicinal chemistry. *Med. Res. Rev.*, 6:451–466.

[B. Leggio, 2016] B. Leggio, M. A. (2016). Otto engine beyond its standard quantum limit. *Phys. Rev. E*, 93:022122.

[Barontini and Paternostro, 2019] Barontini, G. and Paternostro, M. (2019). Ultracold single-atom quantum heat engines. *New J. Phys.*, 21:063019.

[Bera et al., 2017] Bera, A., Riera, A., Lewenstein, M., and Winter, A. (2017). Generalized laws of thermodynamics in the presence of correlations. *Nature Communications*, 8:2180.

[Bergenfeldt et al., 2014] Bergenfeldt, C., Samuelsson, P., Sothmann, B., Flindt, C., and Buttiker, M. (2014). Hybrid microwave-cavity heat engine. *Phys. Rev. Lett.*, 112:076803.

[Bielski and Tencer, 2005] Bielski, R. and Tencer, M. (2005). Absolute enantioselective separation: Optical activity ex machina. *J. Sep. Sci.*, 28:2325.

[Bielski and Tencer, 2007] Bielski, R. and Tencer, M. (2007). A possible path to the rna world: Enantioselective and diastereoselective purification of ribose. *Orig Life Evol. Biosph*, 37:167–175.

[Blickle and Bechinger, 2012] Blickle, V. and Bechinger, C. (2012). Realization of a micrometre-sized stochastic heat engine. *Nature Physics*, 8:143.

[Bouton et al., 2021] Bouton, Q., Nettersheim, J., Burgardt, S., Adam, D., Lutz, E., and Widera, A. (2021). A quantum heat engine driven by atomic collisions. *Nat. Commun.*, 12(1):2063.

[Brandão et al., 2015] Brandão, F., Horodecki, M., Ng, N., Oppenheim, J., and Wehner, S. (2015). The second laws of quantum thermodynamics. *Proceedings of the National Academy of Sciences*, 112:3275.

[Brantut et al., 2013] Brantut, J., Grenier, C., Meineke, J., Stadler, D., Krinner, S., Kollath, C., Esslinger, T., and Georges, A. (2013). A thermoelectric heat engine with ultracold atoms. *Science*, 342:713.

[Breuer and Petruccione, 2007] Breuer, H. and Petruccione, F. (2007). *The Theory of Open Quantum Systems*. Oxford.

[Chen et al.,] Chen, G., Wu, Z., Yu, A., Zhang, Z., Wen, Z., Zhang, K., Dai, L., Jiang, S., Li, Y., Chen, L., Wang, C., and Luo, X. Generation of a sub-diffraction hollow ring by shaping an azimuthally polarized wave. *Sci. Rep.*, 6:37776.

[Chen et al., 2022] Chen, Y., Cheng, J., Ye, C., and Li, Y. (2022). Enantiodetection of cyclic three-level chiral molecules in a driven cavity. *Phys. Rev. Research*, 4:013100.

[Chitambar and Gour, 2019] Chitambar, E. and Gour, G. (2019). Quantum resource theories. *Reviews of Modern Physics*, 91:025001.

[Cirac et al., 1996] Cirac, J., A.S.Parkins, R.Blatt, and P.Zoller (1996). Nonclassical states of motion in ion traps. *Adv. At. Mol. Opt. Phys.*, 37:237–296.

[Cohen-Tannoudji et al., 1998] Cohen-Tannoudji, C., Dupont-Roc, J., and Grynberg, G. (1998). *Atom-Photon Interactions: Basic Processes and Applications*. Wiley.

[Cook, 1979] Cook, R. J. (1979). Atomic motion in resonant radiation: An application of ehrenfest's theorem. *Phys. Rev. A*, 20:224.

[Dawkins et al., 2019] Dawkins, S. T., Abah, O., Singer, K., and Deffner, S. (2019). *Single Atom Heat Engine in a Tapered Ion Trap*. Springer.

[Decker et al., 2019] Decker, T., Zheng, Y., and et al., A. R. (2019). A microscale planar linear ion trap mass spectrometer. *Spectrometer. J. Am. Soc. Mass Spectrom*, 30:482–488.

[Deffner and Campbell, 2019] Deffner, S. and Campbell, S. (2019). *Quantum Thermodynamics*. 2053-2571. Morgan Claypool Publishers.

[et al, 2009] et al, P. F. H. (2009). Positioning of the rf potential minimum line of a linear paul trap with micrometer precision. *J. Phys. B: At. Mol. Opt. Phys.*, 42:154008.

[Fabri et al., 2015] Fabri, C., Horny, L., and Quack, M. (2015). Tunneling and parity violation in trisulfane (hsssh): An almost ideal molecule for detecting parity violation in chiral molecules. *ChemPhysChem*, 16(17):3584–3589.

[Feynman, 1960] Feynman, R. (1960). There's plenty of room at the bottom. *Engineering and Science*, 23:22–36.

[Fink et al., 2010] Fink, J. M., Steffen, L., Studer, P., Bishop, L. S., Baur, M., Bianchetti, R., Bozyigit, D., Lang, C., Filipp, S., Leek, P. J., and Wallraff1, A. (2010). Quantum-to-classical transition in cavity quantum electrodynamics. *Phys. Rev. Lett.*, 105:163601.

[Fleischhauer et al., 2005] Fleischhauer, M., Imamoglu, A., and Marangos, J. P. (2005). Electromagnetically induced transparency: Optics in coherent media. *Rev. Mod. Phys.*, 77:633.

[Foot, 2005] Foot, C. J. C. (2005). *Atomic Physics*. Oxford University Press.

[Fox and Whitesell, 1974] Fox, M. A. and Whitesell, J. K. (1974). *Organic Chemistry*. Jones and Bartlett Publishers.

[Gal, 2012] Gal, J. (2012). The discovery of stereoselectivity at biological receptors: Arnaldo piutti and the taste of the asparagine enantiomersm— history and analysis on the 125th anniversary. *Chirality*, 24:959.

[Gelbwaser-Klimovsky and Kurizki, 2015] Gelbwaser-Klimovsky, D. and Kurizki, G. (2015). Work extraction from heat-powered quantized optomechanical setups. *Sci. Rep.*, 5:7809.

[Gemmer et al., 2009] Gemmer, J., Michel, M., and Mahler, G. (2009). *Quantum Thermodynamics*. Springer-Verlag, Berlin.

[Geusic et al., 1967] Geusic, J. E., Schulz-DuBios, E. O., and Scovil, H. E. D. (1967). Quantum equivalent of the *Carnot* cycle. *Phys. Rev*, 156:343.

[Ghosh et al., 2019] Ghosh, A., Mukherjee, V., Niedenzu, W., and Kurizki, G. (2019). Are quantum thermodynamic machines better than their classical counterparts? *Eur. Phys. J. Spec. Top.*, 227:2043–2051.

[Goold et al., 2016] Goold, J., Huber, M., Riera, A., del Rio, L., and Skrzypczyk, P. (2016). The role of quantum information in thermodynamics—a topical review. *J. Phys. A: Math. Theor.*, 49(14):143001.

[Gordon and Ashkin, 1980] Gordon, J. P. and Ashkin, A. (1980). Motion of atoms in a radiation trap. *Phys. Rev. A*, 21:1606.

[Guo et al., 2022] Guo, Y., Gong, X., Ma, S., and Shu, C. (2022). Cyclic three-level-pulse-area theorem for enantioselective state transfer of chiral molecules. *Phys. Rev. A*, 105:013102.

[Hardal et al., 2017] Hardal, A. U. C., Aslan, N., Wilson, C. M., and Mustecaplioglu, O. E. (2017). Quantum heat engine with coupled superconducting resonators. *Phys. Rev. E*, 96:062120.

[He et al., 2012] He, X., He, J., and Zheng, J. (2012). Thermal entangled quantum heat engine. *Physica A*, 391:6594–6600.

[Herfurth and Blaum, 2008] Herfurth, F. and Blaum, H. K. (2008). *Trapped Charged Particles and Fundamental Interactions*. Springer.

[Hewgill et al., 2020] Hewgill, A., González, J. O., Palao, J. P., Alonso, D., Ferraro, A., and Chiara, G. D. (2020). Three-qubit refrigerator with two-body interactions. *Phys. Rev. E*, 101:012109.

[Hildred1 et al., 1983] Hildred1, G. P., Hassan, S. S., Puri, R. R., and Bullough, R. K. (1983). Thermal reservoir effects in resonance fluorescence. *J. Phys. B: Atom. Mol. Phys.*, 16:1703.

[Huang et al., 2018] Huang, X., Sun, Q., Guo, D., and Yu, Q. (2018). Quantum otto heat engine with three-qubit xxz model as working substance. *Physica A*, 491:604–612.

[Hugel et al., 2002] Hugel, T., Holland, N. B., Cattani, A., Moroder, L., Seitz, M., and Gaub, H. E. (2002). Single-molecule optomechanical cycle. *Science*, 296:1103.

[Hutt and Tan, 1996] Hutt, A. J. and Tan, S. C. (1996). Drug chirality and its clinical significance. *Drugs*, 52:1–12.

[Hönigl-Decrinis et al., 2018] Hönigl-Decrinis, T., Antonov, I. V., Shaikhaidarov, R., Antonov, V. N., Dmitriev, A. Y., and Astafiev, O. V. (2018). Mixing of coherent waves in a single three-level artificial atom. *Phys. Rev. A*, 98:041801.

[Insinga et al., 2016] Insinga, A., Andresen, B., and Salamon, P. (2016). Thermodynamical analysis of a quantum heat engine based on harmonic oscillators. *Phys. Rev. E*, 94:012119.

[Izadyari et al., 2022a] Izadyari, M., Naseem, M. T., and Özgür E. Müstecaplıouglu (2022a). Enantiomer detection via quantum otto cycle. *arXiv*, 2211.06888.

[Izadyari et al., 2022b] Izadyari, M., Öncü, M., Durak, K., and Mustecaplıoglu, O. E. (2022b). Quantum signatures in quadratic optomechanical heat engine with an atom in a tapered trap. *JOSA B*, 39:11.

[Jia and F.Wei, 2011] Jia, W. Z. and F.Wei, L. (2011). Probing molecular chirality by coherent optical absorption spectra. *Phys. Rev. A*, 84:053849.

[Johansson et al., 2013] Johansson, J., Nation, P., and Nori, F. (2013). Qutip 2: A python framework for the dynamics of open quantum systems. *Comput. Phys. Commun.*, 184:1234–1240.

[Jährling and Saghafi, 2011] Jährling, N. and Saghafi, S. (2011). a novel light sheet based imaging technique created by various research disciplines. *Elektrotech. Inftech*, 128:352.

[Kaur et al., 2021] Kaur, K., Singh, V., Ghai, J., Jena, S., and Özgür E. Müstecaplıoğlu (2021). Unified trade-off optimization of a three-level quantum refrigerator. *Physica A*, 576:125892.

[Kieu, 2004] Kieu, T. D. (2004). The second law, maxwell's demon, and work derivable from quantum heat engines. *Phys. Rev. Lett.*, 93:140403.

[Kondru et al., 1998] Kondru, R. K., P.Wipf, and Beratan, D. N. (1998). Atomic contributions to the optical rotation angle as a quantitative probe of molecular chirality. *Science*, 282:2247.

[Kosloff, 2013] Kosloff, R. (2013). Quantum thermodynamics: A dynamical viewpoint. *Entropy*, 15(6):2100–2128.

[Kosloff and Levy, 2014a] Kosloff, R. and Levy, A. (2014a). Quantum heat engines and refrigerators: Continuous devices. *Annual Review of Physical Chemistry*, 65:365–393.

[Kosloff and Levy, 2014b] Kosloff, R. and Levy, A. (2014b). Quantum heat engines and refrigerators: Continuous devices. *Annu. Rev. Phys. Chem.*, 65:365.

[Kosloff and Rezek, 2017] Kosloff, R. and Rezek, Y. (2017). The quantum harmonic otto cycle. *Entropy*, 19:136.

[Král and Shapiro, 2001] Král, P. and Shapiro, M. (2001). Cyclic population transfer in quantum systems with broken symmetry. *Phys. Rev. Lett.*, 87:183002.

[Král et al., 1991] Král, P., Thanopulos, I., Shapiro, M., and Cohen, D. (1991). Coherently controlled asymmetric synthesis with achiral light. *Phys. Rev. Lett.*, 90:033001.

[Lambropoulos and Petrosyan, 2007] Lambropoulos, P. and Petrosyan, D. (2007). *Fundamentals of Quantum Optics and Quantum Information*. Springer.

[Latune et al., 2019] Latune, C., Sinayskiy, I., and Petruccione, F. (2019). Apparent temperature: demystifying the relation between quantum coherence, correlations, and heat flows. *Quantum Science and Technology*, 4:025005.

[Leibscher et al., 2019] Leibscher, M., Giesen, T. F., and Koch, C. P. (2019). Principles of enantio-selective excitation in three-wave mixing spectroscopy of chiral molecules. *J. Chem. Phys.*, 151:014302.

[Letokhov et al., 1995] Letokhov, V. S., Ol'shanii, M. A., and Ovchinnikov, Y. B. (1995). Laser cooling of atoms: a review. *Quantum Semiclass. Opt.*, 7:5.

[Levy et al., 2016] Levy, A., Diósi, L., and Kosloff, R. (2016). Quantum flywheel. *Phys. Rev. A*, 93:052119.

[Levy et al., 2020] Levy, A., Göb, M., Deng, B., Singer, K., Torrontegui, E., and Wang, D. (2020). Single-atom heat engine as a sensitive thermal probe. *New J. Phys.*, 22:093020.

[Li and Shapiro, 2010] Li, X. and Shapiro, M. (2010). Theory of the optical spatial separation of racemic mixtures of chiral molecules. *J. Chem. Phys.*, 132:194315.

[Lindenfels et al., 2019] Lindenfels, D. V., Gräb, O., Schmiegelow, C. T., Kaushal, V., Schulz, J., Mitchison, M. T., Goold, J., Schmidt-Kaler, F., and Poschinger,

U. G. (2019). Spin heat engine coupled to a harmonic-oscillator flywheel. *Phys. Rev. Lett.*, 123:080602.

[Lipson et al., 1995] Lipson, S. G., Lipson, H., and Tannhauser, D. S. (1995). *Optical Physics*. Cambridge University Press.

[Lostaglio, 2019] Lostaglio, M. (2019). An introductory review of the resource theory approach to thermodynamics. *Reports on Progress in Physics*, 82:114001.

[Mari1 et al., 2015] Mari1, A., Farace1, A., and Giovannetti, V. (2015). Quantum optomechanical piston engines powered by heat. *J. Phys. B: At. Mol. Opt. Phys.*, 48:175501.

[Martinez et al., 2016] Martinez, I. A., Roldan, E., Dinis, L., Petrov, D., Parrondo, J. M. R., and Rica, R. A. (2016). Brownian *Carnot* engine. *Nature Physics*, 12:67.

[McKendry et al., 1998] McKendry, R., Theoclitou, M., Rayment, T., and Abell, C. (1998). Chiral discrimination by chemical force microscopy. *Nature*, 391:566–568.

[Metcalf, 1989] Metcalf, H. (1989). Magneto-optical trapping and its application to helium metastables. *J. Opt. Soc. Am. B*, 6:2206–2210.

[Metcalf and van der Straten, 1999] Metcalf, H. J. and van der Straten, P. (1999). *Laser Cooling and Trapping*. Springer.

[Milburn and Walls, 1981] Milburn, G. and Walls, D. F. (1981). Production of squeezed states in a degenerate parametric amplifier. *Opt. Commun.*, 39:401.

[MM et al., 2020] MM, M. A., WM, W. H., and Zhang, W. (2020). Quantum thermodynamics of single particle systems. *Scientific Reports*, 10:13500.

[Myers et al., 2022] Myers, N. M., Abah, O., and Deffner, S. (2022). Quantum thermodynamic devices: From theoretical proposals to experimental reality. *AVS Quantum Science*, 4(2):027101.

[N. Brunner and Skrzypczyk, 2012] N. Brunner, N. Linden, S. P. and Skrzypczyk, P. (2012). Virtual qubits, virtual temperatures, and the foundations of thermodynamics. *Phys. Rev. E*, 85:051117.

[Naseem et al., 2020] Naseem, M. T., Misra, A., and Mustecaplıoglu, O. E. (2020). Two-body quantum absorption refrigerators with optomechanical-like interactions. *Quantum Sci. Technol.*, 5:035006.

[Naseem and Mustecaplıoglu, 2019] Naseem, M. T. and Mustecaplıoglu, O. E. (2019). Quantum heat engine with a quadratically coupled optomechanical system. *J. Opt. Soc. Am. B*, 36:3000.

[Naseem et al., 2018] Naseem, M. T., Xuereb, A., and Özgür E. Müstecaplıoğlu (2018). Thermodynamic consistency of the optomechanical master equation. *Phys. Rev. A*, 98:052123.

[Naseri-Karimvand et al., 2022] Naseri-Karimvand, H., Lari, B., and Hassanabadi, H. (2022). Non-markovianity and efficiency of a q-deformed quantum heat engine. *Physica A*, 598:127408.

[Orlando et al., 1999] Orlando, T. P., Mooij, J. E., Tian, L., van der Wal, C. H., Levitov, L. S., Lloyd, S., and Mazo, J. J. (1999). Superconducting persistent-current qubit. *Phys. Rev. B*, 60:15398.

[Patterson and Doyle, 2013] Patterson, D. and Doyle, J. M. (2013). Sensitive chiral analysis via microwave three-wave mixing. *Phys. Rev. Lett.*, 111:023008.

[Patterson et al., 2013] Patterson, D., Schnell, M., and Doyle, J. M. (2013). Enantiomer-specific detection of chiral molecules via microwave spectroscopy. *Nature*, 497:475.

[Paul, 1990] Paul, W. (1990). Electromagnetic traps for charged and neutral particles. *Rev. Mod. Phys.*, 62:531–540.

[Peterson et al., 2019] Peterson, J. P. S., Batalhão, T. B., Herrera, M., Souza, A. M., Sarthour, R. S., Oliveira, I. S., and Serra, R. M. (2019). Experimental characterization of a spin quantum heat engine. *Phys. Rev. Lett.*, 123:240601.

[Quack, 1986] Quack, M. (1986). On the measurement of the parity violating energy difference between enantiomers. *Chem. Phys. Lett.*, 132(2):147–153.

[Quack and Stohner, 2000] Quack, M. and Stohner, J. (2000). Influence of parity violating weak nuclear potentials on vibrational and rotational frequencies in chiral molecules. *Phys. Rev. Lett*, 84:3807.

[Quan, 2009] Quan, H. (2009). Quantum thermodynamic cycles and quantum heat engines ii. *Phys. Rev. E*, 76:041129.

[Quan et al., 2007a] Quan, H., Liu, Y., Sun, C., and Nori, F. (2007a). Quantum thermodynamic cycles and quantum heat engines. *Phys. Rev. E*, 76:031105.

[Quan et al., 2006] Quan, H. T., Wang, Y. D., xi Liu, Y., Sun, C. P., and Nori, F. (2006). Maxwell's demon assisted thermodynamic cycle in superconducting quantum circuits. *Phys. Rev. Lett.*, 97:180402.

[Quan et al., 2007b] Quan, H. T., Wang, Y. D., xi Liu, Y., Sun, C. P., and Nori, F. (2007b). Quantum thermodynamic cycles and quantum heat engines. *Phys. Rev. E*, 76:031105.

[Quan et al., 2007c] Quan, H. T., xi Liu, Y., Sun, C. P., and Nori, F. (2007c). Quantum thermodynamic cycles and quantum heat engines. *Phys. Rev. E*, 76:031105.

[Quan et al., 2005] Quan, H. T., Zhang, P., and Sun, C. P. (2005). Quantum heat engine with multilevel quantum systems. *Phys. Rev. E*, 72:056110.

[Raab et al., 1987] Raab, E., Prentiss, M., Cable, A., Chu, S., and Pritchard, D. (1987). Trapping of neutral-sodium atoms with radiation pressure. *Phys. Rev. Lett.*, 59:2631.

[R.Grimm et al., 2000] R.Grimm, Weidemüller, M., and B.Ovchinnikov, Y. (2000). Optical dipole traps for neutral atoms. *Adv. At. Mol. Opt. Phys.*, 42:95–170.

[Roßnagel et al., 2014] Roßnagel, J., Abah, O., Schmidt-Kaler, F., Singer, K., and Lutz, E. (2014). Nanoscale heat engine beyond the *Carnot* limit. *Phys. Rev. Lett.*, 112:030602.

[Roßnagel et al., 2016] Roßnagel, J., Dawkins, S. T., Tolazzi, K. N., Abah, O., Lutz, E., Schmidt-Kaler, F., and Singer, K. (2016). A single-atom heat engine. *Science*, 352:325–329.

[Saito and Hyuga, 2013] Saito, Y. and Hyuga, H. (2013). Colloquium: Homochirality: Symmetry breaking in systems driven far from equilibrium. *REVIEWS OF MODERN PHYSICS*, 85:603.

[Scovil and Schulz-DuBois, 1959a] Scovil, H. E. D. and Schulz-DuBois, E. O. (1959a). Three-level masers as heat engines. *Phys. Rev. Lett.*, 2:262.

[Scovil and Schulz-DuBois, 1959b] Scovil, H. E. D. and Schulz-DuBois, E. O. (1959b). Three-level masers as heat engines. *Phys. Rev. Lett.*, 2:262.

[Scully et al., 2011] Scully, M. O., Chapin, K. R., Dorfman, K. E., Kim, M. B., and Svidzinsky, A. (2011). Quantum heat engine power can be increased by noise-induced coherence. *Proc. Natl. Acad. Sci.*, 108:15097.

[Scully and Zubairy, 1997] Scully, M. O. and Zubairy, M. S. (1997). *Quantum Optics*. Cambridge University Press.

[ScullyM et al., 2012] ScullyM, O., Chapin, K. R., Dorfman, K. E., Kim, M. B., and Svidzinsky, A. (2012). Quantum heat engine power can be increased by noise-induced coherence. *Proc. Natl Acad. Sci.*, 108(37):15097–100.

[Shapiro and Brumer, 1991] Shapiro, M. and Brumer, P. (1991). Controlled photon induced symmetry breaking: Chiral molecular products from achiral precursors. *J. Chem. Phys.*, 95:8658.

[Sheng et al., 2021] Sheng, J., Yang, C., and Wu, H. (2021). Realization of a coupled-mode heat engine with cavity-mediated nanoresonators. *arXiv*, 2110.13022.

[Shishkov et al., 2018] Shishkov, V., Andrianov, E., Pukhov, A., Vinogradov, A., and Lisyansky, A. (2018). Zeroth law of thermodynamics for thermalized open quantum systems having constants of motion. *Phys. Rev. E*, 98:022132.

[Singh et al., 2021] Singh, V., Singh, S., Abah, O., and Mustecaplıoglu, O. E. (2021). Unified trade-off optimization of quantum harmonic otto engine and refrigerator. *arXiv:2112.10669*.

[Skrzypczyk et al., 2015] Skrzypczyk, P., Silva, R., and Brunner, N. (2015). Passivity, complete passivity, and virtual temperatures. *Phys. Rev. E*, 91:052133.

[Solfanelli et al., 2020] Solfanelli, A., Falsetti, M., and Campisi, M. (2020). Nonadiabatic single-qubit quantum otto engine. *Phys. Rev. B*, 101:054513.

[Steeneken et al., 2011] Steeneken, P. G., Phan, K. L., Goossens, M. J., Koops, G. E. J., Brom, G. J. A. M., van der Avoort, C., and van Beek, J. T. M. (2011). Piezoresistive heat engine and refrigerator. *Nat. Phys.*, 7:354.

[Tang et al., 2016] Tang, Z. S., Durak, K., and Ling, A. (2016). Fault-tolerant and finite-error localization for point emitters within the diffraction limit. *Opt. Express*, 24:22004.

[Teo and Scarani, 2011] Teo, C. and Scarani, V. (2011). Lenses as an atom–photon interface: A semiclassical model. *Opt. Com.*, 284:4485–4490.

[Tey et al., 2009] Tey, M. K., Maslennikov, G., Liew, T. C. H., Aljunid, S. A., Huber, F., Chng, B., Chen, Z., Scarani, V., and Kurtsiefer, C. (2009). Interfacing light and single atoms with a lens. *New J. Phys.*, 11:043011.

[Tuncer et al., 2020] Tuncer, A., , and Müstecaplıoğlu, O. E. (2020). Quantum thermodynamics and quantum coherence engines. *Turk. J. Phys.*, 44:404.

[Tuncer et al., 2019] Tuncer, A., Izadyari, M., Dag, C. B., Ozaydin, F., and Mustecaplıoglu, O. E. (2019). Work and heat value of bound entanglement. *Quantum Inf Process*, 18:373.

[Tuncer and Mustecaplioglu, 2020] Tuncer, A. and Mustecaplioglu, O. E. (2020). Quantum thermodynamics and quantum coherence engines. *Turk J Phys*, 44:404.

[Uzdin et al., 2015] Uzdin, R., Levy, A., and Kosloff, R. (2015). Equivalence of quantum heat machines, and quantum-thermodynamic signatures. *Phys. Rev. X*, 5:031044.

[van Enk and Kimble, 2001] van Enk, S. J. and Kimble, H. J. (2001). Strongly focused light beams interacting with single atoms in free space. *Phys. Rev. A*, 63:023809.

[Vinjanampathy and Anders, 2016] Vinjanampathy, S. and Anders, J. (2016). Quantum thermodynamics. *Contemp. Phys.*, 57(4):545–579.

[Vitanov et al., 2017] Vitanov, N. V., Rangelov, A. A., Shore, B. W., and Bergmann, K. (2017). Stimulated raman adiabatic passage in physics, chemistry, and beyond. *Rev. Mod. Phys. 89*, 89:015006.

[Walther, 1993] Walther, H. (1993). Nphase transitions of stored laser-cooled ions. *Adv. At. Mol. Opt. Phys.*, 31:137.

[Wang et al., 2012] Wang, J., Wu, Z., and He, J. (2012). Quantum otto engine of a two-level atom with single-mode fields. *Phys. Rev. E*, 85:041148.

[Weimer et al., 2008] Weimer, H., Henrich, M., Rempp, F., Schröder, H., and Mahler, G. (2008). Local effective dynamics of quantum systems: a generalized approach to work and heat. *EPL (Europhysics Letters)*.

[Wineland et al., 2003] Wineland, D. J., Barrett, M., Britton, J., Chiaverini, J., DeMarco, B., Itano, W. M., Jelenković, B., Langer, C., Leibfried, D., Meyer, V., Rosenband, T., and Schätz, T. (2003). Quantum information processing with trapped ions. *Philosophical Transactions: Mathematical, Physical and Engineering Sciences*, 361:1808.

[Woolley, 1976] Woolley, R. G. (1976). Quantum theory and molecular structure. *Adv. Phys.*, 25:27.

[Xu et al., 2021] Xu, M., Stockburger, J. T., Kurizki, G., and Ankerhold, J. (2021). Mimimal model of a quantum heat engine in a bandgap environment. *arXiv*, 2109.12224.

[Ye et al., 2021] Ye, C., Sun, Y., and Zhang, X. (2021). Entanglement-assisted quantum chiral spectroscopy. *Phys. Chem. Lett.*, 12:8591.

[Ye et al., 2018] Ye, C., Zhang, Q., , and Li, Y. (2018). Real single-loop cyclic three-level configuration of chiral molecules. *Phys. Rev. A*, 98:063401.

[Ye et al., 2019] Ye, C., Zhang, Q., Chen, Y., and Li, Y. (2019). Determination of enantiomeric excess with chirality-dependent ac stark effects in cyclic three-level models. *Phys. Rev. A*, 100:033411.

[You and Nori, 2011] You, J. and Nori, F. (2011). Atomic physics and quantum optics using superconducting circuits. *Nature*, 474:589–597.

[Yurke, 1984] Yurke, B. (1984). Use of cavities in squeezed-state generation. *Phys. Rev. A*, 29:408.

[Zhang et al., 2022] Zhang, J.-W., Zhang, J.-Q., Ding, G.-Y., Li, J.-C., Bu, J.-T., Wang, B., Yan, L.-L., Su, S.-L., Chen, L., Nori, F., Özdemir, Ş. K., Zhou, F., Jing, H., and Feng, M. (2022). Dynamical control of quantum heat engines using exceptional points. *Nat. Commun.*, 13(1):6225.

[Zhang and Zhang, 2017] Zhang, K. and Zhang, W. (2017). Quantum optomechanical straight-twin engine. *Phys. Rev. A*, 95:053870.

[Zhang, 2020] Zhang, Y. (2020). Optimization performance of quantum otto heat engines and refrigerators with squeezed thermal reservoirs. *Physica A*, 559:125083.

List of publications

The following articles have been published in the course of this thesis, where most parts of the results have been presented:

- **Quantum signatures in a quadratic optomechanical heat engine with an atom in a tapered trap**

  Mohsen Izadyari,Mehmet Öncü,kadir durak,Ozgur Mustecaplioglu

  JOSA B **39**, 11 (2022).

  https://doi.org/10.1364/JOSAB.472901

  We investigate how quantum signatures can emerge in a single atom heat engine consisting of an atom confined in a tapered trap and subject to hot and cold thermal reservoirs. A similar system was realized experimentally in Ref. [1]. We model such a system using a quadratic optomechanical model and identify an effective Otto cycle in the system's dynamics. We compare the engine's performance in the quantum and classical regimes by evaluating the power dissipated. We find that lowering the temperature is insufficient to make the single atom engine of Ref. [Roßnagel et al., 2016] a genuine quantum-enhanced heat engine. We show that it is necessary to make the trap more asymmetric and confined to ensure that quantum correlations cause an enhancement in the power output [Izadyari et al., 2022b].

- **Enantiomer detection via Quantum Otto cycle**

  Mohsen Izadyari, M. Tahir Naseem, Özgür E. Müstecaplıouglu

  arXiv:2211.06888 [quant-ph] (2022).

  Enantiomers are chiral molecules that exist in right-handed and left-handed conformations. For the discrimination between left- and right-handed molecules, optical techniques of enantiomers detection are widely employed. However, identical spectra of enantiomers make enantiomer detection a very challenging task. Here, we investigate the possibility of exploiting thermodynamic processes for enantiomer detection. In particular, we employ a quantum Otto cycle, in which a chiral molecule described by a three-level system with cyclic optical transitions is considered a working medium. Each energy transition of the three-level system is coupled with an external laser drive. By changing the phase of these drives during the adiabatic stages of the Otto cycle, we find that left- and right-handed molecules work as a heat engine and heat pump, respectively. In addition, if the detuning of the laser drives is varied during adiabatic strokes of the cycle, both left- and right-handed molecules work as heat engines. However, the molecules can still be distinguished because the extracted work and efficiency are quantitatively very different in both cases. Accordingly, left and right-handed molecules can be distinguished by evaluating the work distribution in the Otto cycle [Izadyari et al., 2022a].

Publications not directly related to the selected main topic of this thesis:

- **Work and heat value of bound entanglement**

  Aslı Tuncer, Mohsen Izadyari, Ceren B Dağ, Fatih Ozaydin, Özgür E Müstecaplıoğlu

  Quan. Inf. Proc. **18**, 373 (2019).

  Entanglement has recently been recognized as an energy resource which can outperform classical resources if decoherence is relatively low. Multi-atom entangled states can mutate irreversibly to so-called bound entangled (BE) states under noise. Resource value of BE states in information applications has been under critical study, and a few cases where they can be useful have

been identified. We explore the energetic value of typical BE states. Maximal work extraction is determined in terms of ergotropy. Since the BE states are nonthermal, extracting heat from them is less obvious. We compare single and repeated interaction schemes to operationally define and harvest heat from BE states. BE and free entangled (FE) states are compared in terms of their ergotropy and maximal heat values. Distinct roles of distillability in work and heat values of FE and BE states are pointed out. Decoherence effects in dynamics of ergotropy and mutation of FE states into BE states are examined to clarify significance of the work value of BE states. Thermometry of distillability of entanglement using micromaser cavity is proposed [Tuncer et al., 2019].

Appendix A

.1 *Effective entropy and temperature of the working mode* a

To diagonalize the Hamiltonian (5.5), we first replace the q_z operator with its expectation value. The new effective semi-quantum model describes the radial mode as the working fluid of the engine. The effective reduced model is a quadratic form and it can be diagonalized using the Bogoliubov transformations

$$\hat{a} = \hat{c}\cosh x + \hat{c}^{\dagger}\sinh x, \tag{1}$$

$$\hat{a}^{\dagger} = \hat{c}\sinh x + \hat{c}^{\dagger}\cosh x. \tag{2}$$

Here, $\tanh 2x = \beta q_z/(2\omega_r - \beta q_z)$. The diagonalized Hamiltonian becomes

$$\hat{H}'_{cm} = \omega_{\text{eff}}\hat{n}_c + \omega_z\hat{n}_z + \omega_r \sinh^2 x - \frac{\beta q_z}{2}\big(\sinh 2x + \cosh 2x\big), \tag{3}$$

where an effective frequency ω_{eff} is defined to be

$$\omega_{\text{eff}} = (\omega_r - \frac{\beta q_z}{2})\cosh 2x - \frac{\beta q_z}{2}\sinh 2x. \tag{4}$$